Doctoral theses at NTNU, 2021:280

Tengjiao Jiang

Development and Application of a Vision-Based System for Structural Monitoring of Railway Catenary System

Doctoral thesis

NTNU
Norwegian University of
Science and Technology
Thesis for the degree of
Philosophiae Doctor
Faculty of Engineering
Department of Structural Engineering

NTNU
Norwegian University of
Science and Technology

Tengjiao Jiang

Doctoral theses at NTNU, 2021:280

NTNU

ISBN 978-82-326-6866-3 (printed ver.)
ISBN 978-82-326-5778-0 (electronic ver.)
ISSN 1503-8181 (printed ver.)
ISSN 2703-8084 (electronic ver.)

NTNU
Norwegian University of
Science and Technology

Tengjiao Jiang

Development and Application of a Vision-Based System for Structural Monitoring of Railway Catenary System

Thesis for the degree of Philosophiae Doctor

Trondheim, September 2021

Norwegian University of Science and Technology
Faculty of Engineering
Department of Structural Engineering

NTNU
Norwegian University of
Science and Technology

NTNU
Norwegian University of Science and Technology

Thesis for the degree of Philosophiae Doctor

Faculty of Engineering
Department of Structural Engineering

ISBN 978-82-326-6866-3 (printed ver.)
ISBN 978-82-326-5778-0 (electronic ver.)
ISSN 1503-8181 (printed ver.)
ISSN 2703-8084 (electronic ver.)

Doctoral theses at NTNU, 2021:280

PRINTED IN
NORWAY
NO - 1598

NORDIC SWAN ECOLABEL
Printed matter
2041 0731

Printed by Skipnes Kommunikasjon AS

Preface

This thesis is submitted in partial fulfilment of the requirements for the degree *Philosophiae Doctor* at the Norwegian University of Science and Technology (NTNU). The work has been carried out at the Department of Structural Engineering, Faculty of Engineering. Professors Anders Rönnquist, Professor Ole Øiseth and Associate Professor Gunnstein T. Frøseth have supervised the work. This thesis consists of a collection of three journal papers, one that is published in an international peer-reviewed journal and two that are submitted for publication.

Tengjiao Jiang

Trondheim, Norway
May 1st, 2021

Publications

Included publications

The following papers are included in this thesis:

I. T. Jiang, G. T. Frøseth, A. Rønnquist and E. Fagerholt. A robust line-tracking photogrammetry method for uplift measurements of railway catenary systems in noisy backgrounds. *Mechanical Systems and Signal Processing*, 144 (2020) 106888. doi: 10.1016/j.ymssp.2020.106888

II. T. Jiang, A. Rønnquist, Y. Song, G. T. Frøseth and P. Nåvik. A detailed investigation of uplift and damping of a railway catenary span in traffic using a vision-based line-tracking system. Submitted for journal publication, 2021.

III. T. Jiang, G. T. Frøseth, P. Nåvik and A. Rønnquist. Assessment of transition section contact point spatial variation via optical-based field measurements of railway catenaries. Submitted for journal publication, 2021.

Declaration of authorship

Tengjiao Jiang is the first author of all papers (I-III) included in this thesis. Other co-authors for the papers in this thesis are: Anders Rønnquist (papers I-III), Gunnstein T. Frøseth (papers I-III), Egil Fagerholt (paper I), Yang Song (papers II) and Petter Nåvik (papers II-III). Tengjiao Jiang came up with the ideas, algorithm programming, gathered the data, implemented the theory, obtained experimental results from both the field and the laboratory tests, analysed the results and wrote the manuscripts in all three papers. Anders Rønnquist, Gunnstein T. Frøseth, Egil Fagerholt, Yang Song and Petter Nåvik discussed the work for the papers they co-authored and provided constructive criticism, which increased the scientific quality of the papers.

Other scientific contributions

The following papers are related to the topic of this thesis and are published in journals and conference proceedings during the PhD study:

1) Y. Song, A. Rønnquist, T. Jiang and P. Nåvik. Identification of short-wavelength contact wire irregularities in electrified railway pantograph–catenary system. *Mechanism and Machine Theory*, 162 (2021) 104338. doi: 10.1016/j.mechmachtheory.2021.104338.
2) Y. Song, T. Jiang, A. Rønnquist, P. Nåvik and G. T. Frøseth. The effects of spatially distributed damping on the contact force in railway pantograph-catenary interactions. *IEEE Transactions on Instrumentation & Measurement*. Accepted for publication, 2021.
3) Y. Song, T. Jiang, P. Nåvik and A. Rønnquist. The geometry deviation effects of railway catenaries and the pantograph-catenary interaction: a case study in Norwegian railway system. Submitted for journal publication, 2021.

Abstract

With the continuous increase of train speed and the expansion of the railway network, health monitoring and predictive maintenance of railway infrastructure are becoming increasingly important. The increasing investments in inspection and infrastructure maintenance have initiated the need for intelligent and accurate measuring techniques. Railway catenary systems are critical to ensure a stable and continuous power supply for electrical railways. The current collection is achieved as the contact wire directly interacts with the pantograph, installed on the car-body roof to provide an electrical current to the engine. The dynamic behaviour of catenary systems is significant to determine the current collection quality.

This thesis proposes a vision-based line-tracking system (VIBLITE) to enable remote, non-contact and non-marker uplift measurements of catenary systems. This system avoids the defects of the traditional uplift measuring methods, e.g., track access, substantial time and work for sensor or marker installation on wires. An image-processing line-tracking algorithm for addressing the essential challenge of tracking slender wires without markers against noisy backgrounds is developed to achieve robust and accurate uplift measurements. The accuracy, robustness and applicability of VIBLITE are validated and demonstrated through numerical experiments, the field uplift measurement of the railway catenary system and the identification of the contact wire in a diverse city environment.

Damping plays an essential role in numerical simulations of pantograph-catenary interaction, especially for multiple pantographs. However, damping estimation of existing catenary sections is recognised as a challenge, and only a few studies have been published with single values of damping estimations. Thus, the spatially distributed damping of an existing catenary span was estimated by VIBLITE through uplift measurements. The damping ratios were identified using the covariance-driven stochastic subspace identification (Cov-SSI) method. The results were presented as Rayleigh damping coefficients, showing a notable spatial variation to be used in

numerical simulations. A small but clear train direction dependency of the damping distribution was observed over the entire span. Thus, it is recommended to consider the spatial damping distribution's influence when conducting future numerical simulations, especially when energy dissipation can be a vital component.

Finally, catenary section overlaps are designed to provide a transition between two consecutive catenary sections. The thesis studied the pantograph-catenary interaction and transition at the overlap span experimentally. VIBLITE with a new measuring method for the specific overlap span was developed and implemented under regular train operations to estimate the dynamic spatial vibration of the contact wires. The research explores the reasons for the high contact forces and the contact loss rendering arcing at overlap span. The important transition section distance, i.e., the length where the pantograph runs on both contact wires, was obtained and assessed at varying train speeds to study correlations.

Acknowledgements

I am very grateful to my father and mother, not only for gifting the world with happiness and health, but also to give continuous encouragement and endless support on my growth path. When I was a child, the unfairness of educational resources between modern cities and towns was serious. My parents are the ones who do their best to help me transfer school from the village to the city for better education. There were three primary schools that I had taken in six years, which greatly changed my later growth and education. The experience mentioned here is to appreciate my parents for all the emphasis they put on education, family and hobbies.

No matter how bitterly I failed, how hard I fell or how embarrassingly I was defeated, I always knew that when I come back home to both of you, I will be treated like a winner. Thanks for being amazing parents.

爱子心无尽，归家喜及辰。寒衣针线密，家信墨痕新。
见面怜清瘦，呼儿问苦辛。低徊愧人子，不敢叹风尘。
——致父母

My main supervisor, and good friend, Anders Rønnquist, should be acknowledged. Appreciate you having me fulfil my research dream and give me many opportunities to improve myself. I clearly remember the precious and happy time when we attended meetings in Houston or performed experiments at Gardermoen, Oslo. The experience that I have in the PhD study has really shaped me and help me understand my life purpose. I have learned a lot from you, both in research and in life. I also appreciate my co-supervisors, Ole Øiseth and Gunnstein T. Frøseth, for the valuable suggestions and discussions on research.

Appreciate to my current and former colleagues at the Structural Dynamics group, Yang Song, Mingjie Zhang, Petter Juell Nåvik, Knut Andreas Kvåle, Bjørn Thomas Svendsen, Aksel Fenerci, Niccolo Barni, Stefano Derosa, Øyvind Wiig Petersen, Dario Rafael Fernandez Castellon, Sebastian Reymert, Maria Zakharenko, Anno Christian

Dederichs, Oddbjørn Kildal, Marcin Luczkowski, Sverre Magnus Haakonsen, for creating a warm group environment in cold Norway.

I would also like to thank Egil Fagerholt for sharing his innovative methodology and code. Thanks to Engineer Trond Auestad and Per Øystein Nordtug for their great help in experiments.

To all my friends in Norway, thank you for giving me an unforgettable and wonderful life in the past three years. Even after decades, I will miss the beauty of life in Trondheim.

Finally, I must acknowledge my fiancée. It has been seven years since we fell in love. Living in a different country prevents me from making more memories and company with you. You always give me endless support and help me pass through difficulties, and you have become the strongest spiritual support in my heart. Thank you for always being there for me. You inspire me to be a better man, and I can not wait to grow old with you.

Contents

Chapter 1

Introduction

1.1 Background and motivation

With the development of the world economy, railways have played an essential role in passenger and freight transport [1]. According to energy sources, locomotives can broadly be classified into steam, internal combustion, and electric.

Richard Trevithick built the first full-scale working steam locomotive for the Coalbrookdale ironworks in the United Kingdom in 1802 [2]. The first commercially viable steam locomotive was named Salamanca and built by Matthew Murray for the Middleton Railway between Middleton and Leeds in 1812 [3].

A century later, the first successful diesel locomotives appeared in the United States in 1925, representing the new technology debut for the internal combustion locomotives. The internal combustion locomotives are classified by fuel types, mainly includes kerosene, petrol, diesel. Diesel locomotives were widely adopted in many countries during the economic recovery from World War II, due to their higher performance and flexibility and lower operating and maintenance costs than steam locomotives [4]. The diesel-electric locomotive is the most widely adopted diesel locomotive today. Its main feature is the diesel engine using electric transmission to power trains, and there is no mechanical connection between the diesel engine and the wheels.

The first example of an electric train powered by a fixed ground installation is the passenger train presented by Werner von Siemens in 1879, which was supplied by a third insulated rail. The first regular service in the world powered by an overhead line was the tram line between Mödling and Hinterbrühl near Vienna, Austria, in 1883 [5]. Electric locomotives can be powered by electricity mainly from three sources: an overhead line, a third rail or an on-board battery. Lower operation and maintenance costs, higher energy efficiency and environmentally friendly operations are the advantages of electric locomotives compared to diesel locomotives. However, the high infrastructure building cost for overhead lines or third rail, substations and control systems is the main drawback of electrification.

The overhead line is a primary form of power supply for electric locomotives and is the critical subsystem of the railway [1]. Electric locomotives collect the current from the contact wire while running. The pantograph-catenary interaction has become more frequent and severe with the increase in train speed [6]. The damage of overhead lines is accumulated under operation.

High demand for rail service and the new construction of railway lines impose higher requirements on the maintenance. For a reliable power supply, the pantograph-catenary system needs to be monitored periodically [7,8]. The development of efficient detection technologies and methods is significant to ensure both availability and safety in electrified railways [9].

1.2 Railway pantograph-catenary system description

1.2.1 General

Most high-speed trains in operation today are powered by electricity since internal combustion locomotives are essentially unable to generate energy to reach high speeds [10]. The main task of the railway catenary system, or overhead contact line (OCL) system, is to supply uninterrupted and steady electricity to the trains. The electrical power is then used both for the traction and for the supply of the auxiliary services on board.

As of January 2019, the Norwegian electrified railway cover 2451 km, which accounts for 58.4% of the total Norwegian railway network, as shown in Table 1.1.

The distribution of electrified and non-electrified railways in Norway are illustrated in Fig. 1.1. Ice accretion on the catenary system may result in additional loads and even prohibit the pantograph from contacting the contact wire, which will interrupt the train's power supply [1]. This phenomenon makes the design of railway catenary in colder climates more difficult. However, the electrified railways are successfully built all over Norway, and the electrification of the north is now in the planning stages.

Table 1.1. Norwegian railway network as of January 2019 [11].

	Length [km]	Percentage
Electrified railway	2451	58.4 %
Non-electrified railway	1749	41.6 %
Total	4200	

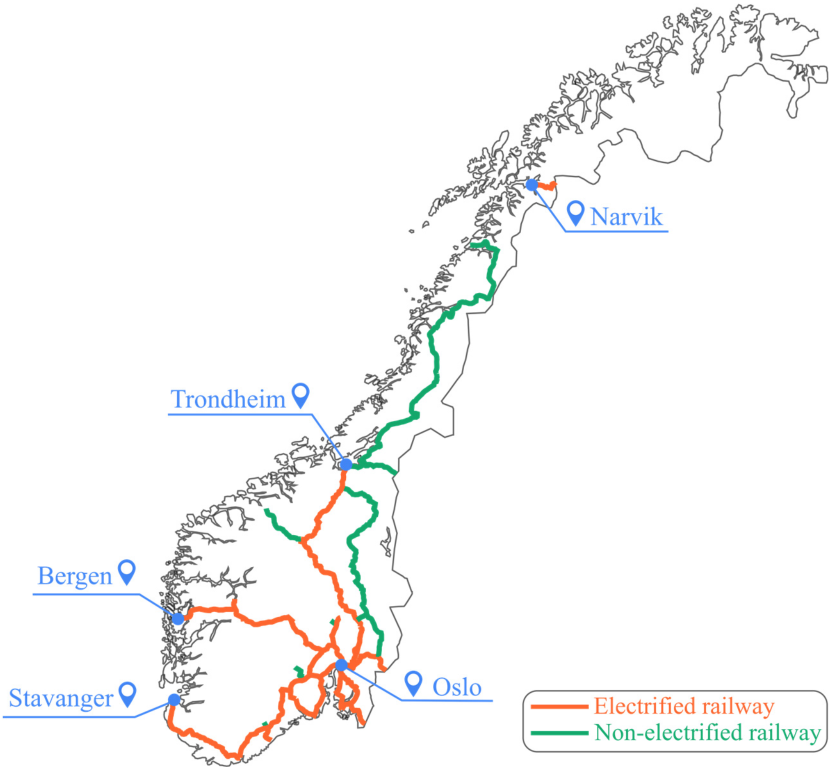

Fig. 1.1. Norwegian railway network. Data: Bane NOR. Drawing: Tengjiao Jiang.

1.2.2 The catenary system

There are three main types of high-speed catenaries implemented globally: simple catenary, stitch wire catenary, and compound catenary [12], as shown in Fig. 1.2. The catenary system's main structural components comprise contact wire, messenger wire, droppers, fixed points, and tension devices [1], indicated in Fig. 1.3. All three catenary types have the same common components with different design features. The catenary needs to be suspended by cantilevers at poles in regular intervals by fastening the messenger wire on the brackets. The typical spacing is 50 m, but it can be adjusted due to line curves, surrounding structures, etc. The contact wire is the component in contact with the pantograph and follows a zigzag pattern called stagger. The stagger ensures that the sliding-contact point moves over the panhead from side to side to distribute the wear. The correct horizontal geometry of the contact wire is achieved by using registration arms.

The simple and stitch wire catenary are widely adopted on high-speed railways in the world. They are both designed to use messenger wire to suspend the contact wire to the required height, achieved by droppers clamped between both wires [13]. The difference between simple and stitch wire catenary types is the adoption of stitch wires. The main task of stitch wires is to improve the stiffness uniformity near the poles. The uniform stiffness could minimise the pantograph's vertical movement, which is critical for high-speed trains. The simple and stitch wire catenary are designed with a pre-sag of 1/1000 to improve the stiffness uniformity [14].

The compound catenary, commonly used in the Japanese Shinkansen lines, uses the auxiliary messenger wire to suspend the contact wire. The messenger wire is designed to suspend the auxiliary messenger wire by droppers. The compound catenary advantage is that it maintains almost constant stiffness while guaranteeing the uniform height of the contact wire without pre-sag [12].

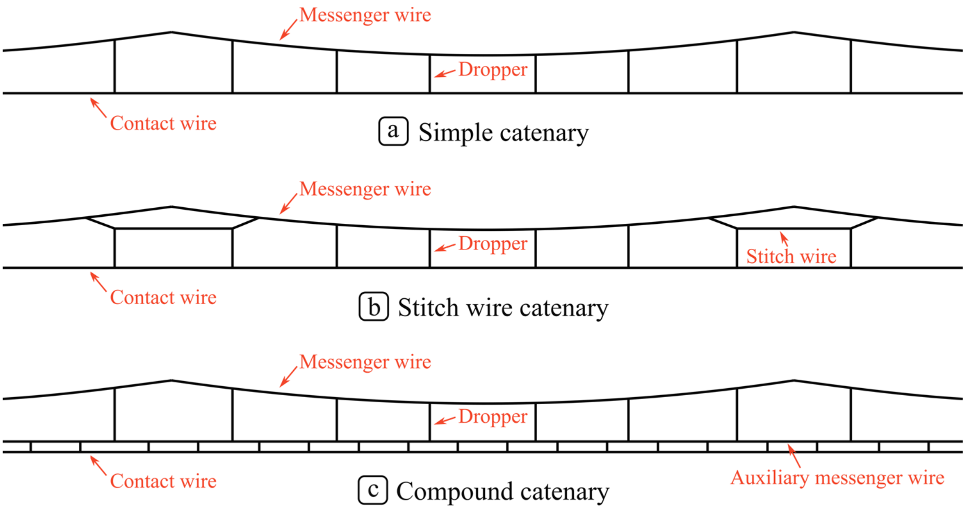

Fig. 1.2. Different type of high-speed catenaries implemented in the world.

Different design speed requires different design geometries. That is, as the railway design speed increases over the years, new catenary systems are developed and implemented. In Norway, the now-outdated system "Tabell 54" is being replaced by the newer "System 35" (150 km/h), "Systems 20" (200 km/h) and "System 25" (250 km/h) [15]. The corresponding design parameters are listed in Table 1.2.

Fig. 1.3. Stitch wire catenary in Oslo airport line in Norway. Photography: Tengjiao Jiang/NTNU.

Table 1.2. Catenary system parameters in Norway. CW: contact wire. MW: messenger wire.

Catenary type	Tension [kN]		Maximum speed [km/h]	Stitch wire
	CW	MW		
Tabell 54	6.1	4.9	80	No
Tabell 54 op	10	5	130	No
System 35	7.1	7.1	150	Yes/No
System 20 A	10	10	200	Yes
System 20 B	10	10	160	No
System 20 C1	13	13	200	Yes/No
System 20 C2	13	13	160	No
System 25	15	15	250	Yes

Tabell 54 is the older catenary system, initially designed for low train speeds up to 80 km/h. After an upgrade, with the tension force changed to 10 kN and 5 kN in the contact and messenger wire, respectively, to improve the catenary system dynamic performance, the allowed speed is today 130 km/h. Tabell 54 is still used and is a major part of the Norwegian railway network, but it is no longer considered for new constructions.

System 35 is a catenary system designed after Tabell 54, with a maximum design speed of 150 km/h. This catenary system could be designed with or without stitch wires.

System 20, a newer system than System 35, is divided into four types: Standard A, B, C1 and C2, according to the different design parameters.

System 25 is the latest catenary system among the four, with a maximum speed of 250 km/h, and contact and messenger wires' tension increases to 15 kN. This system only exists in newly built lines.

Each catenary section has a limited length of about 1-1.5 km due to thermal expansion and tension variation at each cantilever [16]. The catenary tension force can be provided by springs or by fixing, but more commonly by mechanical tensioning devices, including weights and pulleys mounted at both ends of each catenary section, as shown in Fig. 1.4. The contact and messenger wire are fixed at the section midpoint. The tensioning devices can maintain constant tension with only minor changes in the tension force induced by temperature, friction and defects. This solution is reliable and straightforward and makes catenary tension easy to adjust by increasing or decreasing weights.

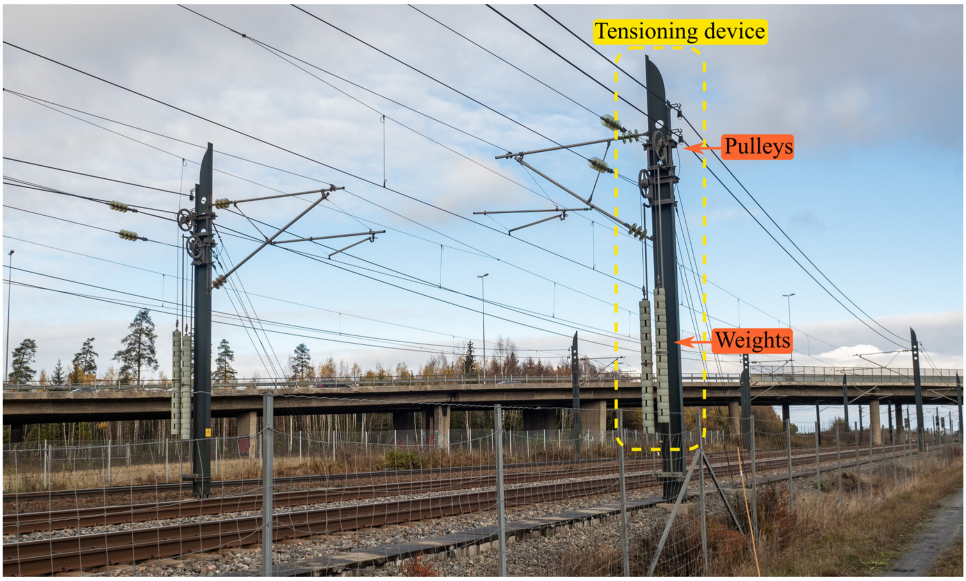

Fig. 1.4. Tensioning device at the end of catenary sections. Photography: Tengjiao Jiang/NTNU.

1.2.3 The pantograph

The pantograph is a device mounted on the electric locomotive roof to collect electric current by sliding contact with the contact wire, and the return current is transmitted through the rails. The pantograph can be categorized into three types, including single-arm, diamond-shaped, and wing-shaped.

Single-arm pantograph has been widely adopted today and exhibits compact and responsive performance at high speeds. The main components include the panhead, upper and lower arms, guiding and coupling rods, lifting control device and insulators, as shown in Fig. 1.5. Carbon contact strips are mounted on the top of panhead. These carbon strips are able to conduct electricity and reduce wear compared to a pure metal strip.

The pantograph lifting is achieved by the lifting device that generates a force in the base, raising the pantograph until the carbon strips make contact with the contact wire. The static contact force between the contact wire and contact strips is adjustable. The lifting device lifts or lowers the pantograph's vertical position to ensure the best possible contact force when the train is running.

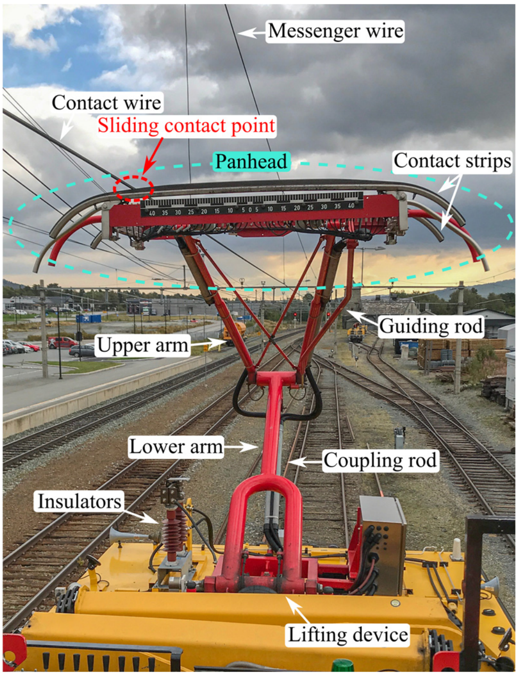

Fig. 1.5. Single-arm pantograph composition. Photography: Tengjiao Jiang/NTNU.

A multiple pantograph configuration is usually adopted when it is necessary to collect enough energy required by the electrical engines to reach high operational train speeds or when multiple-unit trains are adopted [17]. However, the multiple pantograph operation leads to new challenges that the single pantograph operation does not have, such as the deterioration of the rear pantograph's current collection quality [18], which needs to be appropriately numerical simulated [17]. The double pantograph is a more common type of multiple pantograph system in many countries, especially in China. Thus, the double pantograph-catenary interaction has gradually become the primary design consideration in the newly built railway lines to enhance the capacity of high-speed trains [18].

1.3 Catenary uplift monitoring methods

Catenary systems will, over time, be exposed to normal wear, structural damage, and general fatigue, all influenced by the pantograph load, power transmission and weather conditions. During the technical life of the structural system, it can be expected to have a response from unduly low to excessively high uplift of the contact wire [1]. Structural damage will introduce changes in catenary systems' geometric and mechanical characteristic, making the system deviate from its design values. Stiffness and damping are two important structural properties for the structural response, where both can be affected by wear and damage. This makes validation and monitoring of these parameters important to ensure the efficient performance of the railway system.

Catenary system monitoring obtains the current structural state to enhance maintenance and improves structural reliability [13,19]. Many methods have been developed to assess the health condition of catenary systems. Uplift and contact force measurements are increasingly important to evaluate the dynamic response of the pantograph-catenary interaction, especially when the train speed exceeds the initial design speed [1]. According to the Norwegian National Rail Administration [20], the maximum contact wire uplift at the steady arm point should not exceed the safety value of 120 mm at train speeds exceeding 200 km/h. Thus, uplift measurement provides valuable information on the catenary systems' structural condition and operating performance in service. Uplift monitoring methods can be divided into three main types according to the measuring principles: physical contact, partial physical contact and no physical contact methods.

1.3.1 Methods requiring physical contact

Due to the application advantages such as high reliability and accuracy, the monitoring methods requiring physical contact were applied early to the catenary uplift measurement, and the adopted sensors usually include potentiometers [21,22], Fiber Bragg Grating (FBG) transducers [23] and accelerometers [24-26].

The Deutsche Bahn AG (DB) [21] recorded the contact wire uplift during traffic with a measuring device installed at a catenary system cantilever in 2002. The measuring principle used an insulating rope attached to the contact wire to transfer uplift to a potentiometer. An electrical signal induced by the rotation angle at the potentiometer represents the uplift data. The British East Coast Main Line in United Kindom [22] estimated a catenary section displacement and mechanical damping characteristics in 2003. They used drawstring potentiometers connected to the catenary wires to obtain the displacement of five different locations. The experiment was conducted using an impulse excitation generated by forcing the wires downwards followed by a quick release. The Norwegian National Rail Administration (Jernbaneverket) [27] measured the uplift during traffic with a fixed measuring equipment at a cantilever in 2008. An optical cable fixed to the contact wire was adopted to transfer the uplift data.

In 2009, Laffont et al. [23] used three displacement sensors based on Fiber Bragg Grating (FBG) transducers to monitor the 3D contact wire displacement. FBG transducers are mounted on the support structure above the contact wire. Three mobile rods are linked to springs for transmitting the contact wire displacement to the transducers. Traditional sensors have shortcomings, such as little flexibility for the positioning due to the need for fixed structures (e.g., cantilevers) and wire arrangement. To overcome these limitations, Nåvik et al. [24,25] presented a newly developed wireless sensor system consisting of a tri-axis gyroscope, a tri-axial accelerometer and a Digital Motion Processor in 2016. The sensor system is mounted on the wires to carry out arbitrary point field measurements. The uplift is approximated by the acceleration integration [28]. Vo Van et al. [26] also obtained the catenary system acceleration by using four tri-axis accelerometers installed on catenary wires. In the latter, excitation was achieved by dropping masses attached to the catenary wires.

1.3.2 Methods requiring partial physical contact

Partial physical contact methods require the marker or target installation on contact wires to achieve measurement, and track access is necessary. Thus, these methods are not wholly non-contact and may interrupt train daily operation.

Korea Railroad Research Institute [29] developed a high-speed image measurement system with a template matching technique to measure the contact wire uplift in 2009. The system was installed at a cantilever to track a marker installed on the contact wire for uplift measurement. Karwowski et al. [30] used laser measuring equipment in Poland to measure the contact wire uplift. This approach requires a reflective plate installed on the contact wire with a laser displacement meter fixed on the top catenary support structure. The train detection and speed measurement were realised by using a laser rangefinder. Frøseth et al. [28] in Norway used a calibrated stereo camera system to measure the uplift in the field by tracking a well-defined marker attached to the catenary wire. One week of train passages was recorded and statistically evaluated to study the dynamic behaviours of an existing catenary system.

1.3.3 Methods requiring no physical contact

No physical contact methods could achieve uplift measurements in a long distance without the marker installation on contact wires, which greatly improve applicability and operability.

Only a few publications studied the no physical contact methods. In 2007, Hietzge et al. [31] developed a mobile uplift measuring device consists of four camcorders. Two camcorders estimated the contact wire uplift close to the first and last dropper within the span. The third camcorder recorded the midspan uplift, and the fourth one estimated the train's running speed. In 2011, Vázquez et al. [32] used an infrared screen to project the light to pass through the contact wire to a line-scan camera and measure the contact wire uplift by the projection in images. Zou et al. [33,34] performed non-contact measurements via photogrammetry without markers in a laboratory. The contact wire was excited by single-point lifting, and the uplift was estimated by using an edge detection technique in post-image processing. The damping ratio and Rayleigh damping coefficients were estimated by the continuous wavelet transform (CWT) method.

1.3.4 Research status summary

All of the physical and partial physical contact methods meet the resolution requirement for uplift measurement, but they have the common problem of requiring track access and equipment or marker installation on the contact wire or the mounting of the measuring devices to the support structure of the catenary system. This means that these devices require substantial time and a workforce to install while disrupting traffic.

For fixed long-term monitoring, these devices are capable of obtaining the required uplift data. However, a portable measurement device is still necessary for inspectors to perform multi-point measurements more conveniently and quickly without disrupting traffic. For field testing, portability, robustness in varying environmental conditions, low power consumption, and the possibility of battery operation play a primary role in the choice of the equipment [35]. Thus, it is necessary to develop a complementary portable and robust device for the uplift measurement, convenient and easy to install and use.

Compared with the publications of physical and partial physical contact methods, there are a few studies on no physical contact methods, and all of the published no physical contact methods adopted camera technologies. However, the general problem, which is that the contact wire is challenging to track without markers in front of a noisy background, has not been addressed. Thus, this thesis focuses on developing a novel line-tracking algorithm against the noisy background with a portable vision-based uplift measuring device.

1.4 Vision-based techniques

Computer vision (CV) technology uses cameras and post-image processing to detect, track and measure targets and even train computers to understand digital images or videos. Vision-based (or image-based) optical techniques is a branch of computer vision and has been applied to many engineering fields due to its ability to perform non-contact measurement at long distances and without interference to the daily structure operation, and its concept illustrates in Fig. 1.6.

Vision-based techniques can take every pixel in the camera's view into a vibration sensor, increasing the availability and obtaining more useful structural responses. However, when the structure response, e.g., displacement, accelerations and strain, is subtle, reliable and accurate measurements may not be achieved by using vision-based techniques due to the resolution limitations of digital image sensors [36].

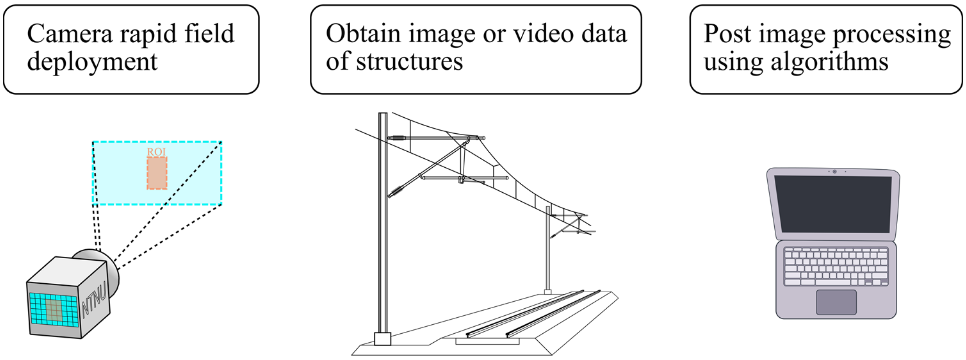

Fig. 1.6. Vision-based monitoring concept.

1.4.1 Workflow for structure monitoring

Vision-based techniques for structural monitoring include acquiring image sequences or videos using one or several cameras and conducting post-processing to get the required information. The vision-based methods mainly include four main blocks, illustrated in Fig. 1.7.

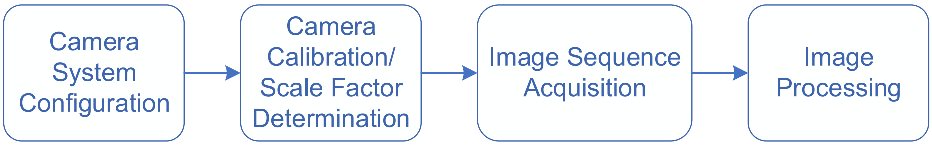

Fig. 1.7. Block diagram of vision-based techniques for structural monitoring.

The four main steps are generally introduced as follows:

Camera System Configuration - Camera system configuration mainly consists of building a set of devices for camera operation in varying environment, wiring, data transmission and storage, and power supply.

Camera Calibration/Scale Factor Determination - Camera calibration obtains the parameter of a lens and a camera image sensor to remove lens distortion or determine the geometric transformation (scale factor). A pinhole camera calibration model adopted in this thesis is detailed in Section 3.2.3.

Image Sequence Acquisition - This step sets up the camera system and acquires image sequences/video of the structure in operation.

Image Processing - The user adopts an algorithm to detect and track the structure by processing the image sequences/videos. Image processing algorithms have received more attention, and there are many kinds of literature to develop algorithms when applying vision-based techniques to different fields. A novel line-tracking algorithm for monitoring railway catenary systems is proposed in this thesis in Section 2.3.

1.4.2 Catenary system monitoring

Due to the sliding contact with the pantograph, the catenary system experiences wear that eventually must be addressed in maintenance or results in severe damage that inhibits the ability of the catenary system to supply power to locomotives. Vision-based techniques have been developed and performed in a variety of tasks in catenary monitoring, such as measuring the catenary motion [28,37-39], monitoring the catenary part [9,40-44] and measuring catenary geometry parameters [6,45]. Many studies usually install cameras on the train roof to sample images with artificial lights to improve availability in low-light situations, e.g. night or tunnel, and the schematic is shown in Fig. 1.8.

A vision-based method based on deep convolutional neural networks (DCNNs) achieved automatic defect detection of fasteners on the catenary support device in research by [29]. This method was verified on the Wuhan-Guangzhou high-speed railway line, China. The study [39] investigated wave reflection occurring at the dropper junctions by using a high-speed linear camera, because the catenary wave propagation property affects the interaction performance.

More frequently, vision-based methods have also been used to detect the catenary part, e.g. contact wire, dropper, cantilever, steady arm and pole. For instance, [41] proposed a dropper failure and defect detection method, which consists of a multialgorithm fusion image processing technique, a faster R-CNN algorithm and a subpixel dropper defect detection model. The performance was verified by the catenary images taken from a practical high-speed railway. A catenary fault inspection system by using the wavelength band of ultraviolet (UV) and Infrared (IR) camera to measure the insulation of corona and temperature of catenary wires was introduced in [44].

Catenary geometry parameter measurement is another application of vision-based techniques. A vision-based measurement system using binocular line-scan cameras for railway catenary geometry parameters was built in the study [6]. The article [45] measured the contact wire height and stagger by an inspection vehicle, consisting of the laser emission system, the image acquisition system and the image processing system. A laser emitter and a camera are installed on the device platform and controlled by a computer to collect image sequences.

Other applications include measuring the catenary wear, in research by [46], using supplementary laser light and binocular linear array camera. The study [47] analysed the measurement uncertainty for measuring the contact wire position by using a vision-based method, performed with the use of the Monte Carlo Method.

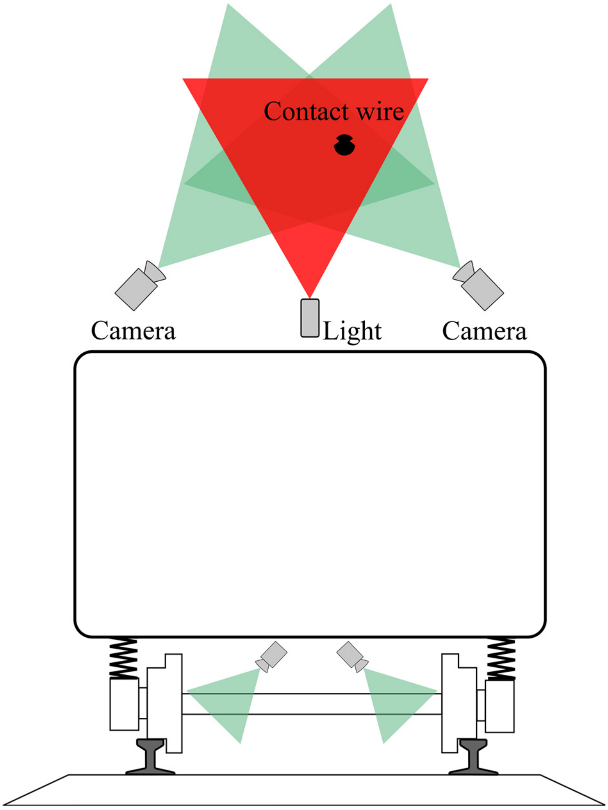

Fig. 1.8. Schematic of vision-based techniques for railway catenary monitoring.

1.4.3 Pantograph monitoring

The pantograph strip ensures the contact wire's sliding contact. The strip is designed to wear faster than the wire, thus needing to be replaced frequently. Excessive wear or defects of contact strips affects pantograph-catenary interaction and results in faster wear of contact wire.

Strip damage detection is one of the primary detection items. A novel contact strip 3D inspection system was first presented in the literature [48] by adopting a specialised camera and a laser line generator. This device was performed on a railway line, and after scanning the contact strip surface, the surface damage could be 3D visualised. The automatic analysis algorithms of contact strip's wear were also introduced in this study. The literature [49] also described an automatic visual inspection system made of a 3D laser scanner and a 2D high-resolution camera, which could achieve automatic monitoring of the health state of the contact strips.

In addition to the use of lasers, the transverse displacement signal of the contact wire could be analysed to detect the contact strip's critical damage. For instance, [50] introduced a visual strip damage detection method by using a 2D camera to measure the contact wire's transverse displacement. Because the velocity signal of the transverse displacement has a comparable level to the identical damage, the critical damage location could be identified. However, this method is not sensitive to subtle surface damage.

The overall pantograph health is another monitoring item, which vision-based techniques can also perform. For example, the work [51] proposed a predictive maintenance method using a fuzzy classifier. A camera and a temperature sensor obtain image and temperature data as input to the fuzzy classifier to monitor the pantograph health. The remaining usable time of the pantograph-catenary system and existing faults could be estimated.

1.4.4 Contact and arc monitoring

The pantograph-catenary contact quality hugely affects the current collection quality. As such, contact point monitoring and arc detection play an important role in evaluating contact quality. An infrared camera was adopted in work by [52] to investigate the pantograph-catenary interaction. To detect the contact strip temperature, a segment-tracking algorithm based on Hough transformation was developed. The work [53] deals with a method based on kernel-based object tracking to estimate the pantograph-catenary interaction. The contact point and occurred arcs were detected by combining tracking and foreground detection methods. The pantograph strip faults were detected by employing S-transform. An FPGA (Field Programmable Gate Arrays) based new fault detection method was proposed in the research [54] to detect the arcs and the contact point by attaching a camera to the FPGA kit and saving images to SDRAM and RAM blocks. The article [55] proposed a novel approach for image processing-based monitoring and fault diagnosis to monitor contact points and assess the pantograph-catenary interaction. The pantograph surface is divided into the fault, dangerous and safe regions to determine each region's effects on system performance.

Deep learning is another approach to detect the pantograph-catenary interaction. For instance, a CNN (Convolutional Neural Network)-based method was introduced in [56] for arc detection. The study [19] developed a robust pantograph-catenary interaction condition monitoring method based on a deep convolutional network. The pantograph strip was detected and segmented by a deep pantograph network (DPN), and the edge detection and the Hough transform was used to detect the contact wire. The contact point was found by calculating the intersection between the contact wire and the pantograph strip surface. Similarly, a two-stage detection method based on a convolution neural network was proposed in the article [57] to detect the contact point. YOLO V3 network detected the pantograph-catenary contact region in images, and the contact point was obtained by intersection calculation. The research [58] also achieved arc detection and recognition by using a CNN-based model.

1.5 Objectives and scope

1.5.1 Objectives

The primary objective of this thesis is to develop a vision-based measuring system for the dynamic performance of railway catenary systems. To achieve this goal, the following research objectives must be realised.

Build a set of vision-based hardware equipment for measuring line-like structure

According to the current hardware device status, Section 1.3.4 puts forward the new uplift measuring system's requirements, include non-track-access, non-contact and non-marker measurement, good portability and robustness, rapid field deployment, easy operation, and high accuracy. Vision-based techniques meet these requirements, and equipment can be mounted at a distance from the railway while uplift measurements are carried out in a non-contact way. Thus, a vision-based system needs to be built for measuring the uplift successfully.

Develop an image-processing algorithm for addressing the essential challenge of tracking slender wires without markers against noisy backgrounds

The image background generally consists of a non-uniform or noisy background that makes it challenging to identify and track the contact wire. In simple approaches to track the contact wire in front of a noisy background, the tracking algorithm may lose the tracking or mistake, for instance, a tree branch for the contact wire and disrupt the performance of the measurement system. Therefore, it is necessary to impose restrictions on the search for contact wire tracking. A novel line-tracking algorithm needs to be developed to track wires without markers against noisy backgrounds.

Investigate uplift and damping of an existing railway catenary span under regular train operation

Damping plays an essential role in numerical simulations of pantograph-catenary interaction, especially for multiple pantographs. However, damping estimation of existing catenary sections is recognised as a challenge, and only a few studies have been published with single values of damping estimations. Thus, the spatially distributed uplift and damping of the catenary span are significant to be investigated under regular train operation. Rayleigh damping coefficients need to be estimated and recommended for numerical models.

Study pantograph-catenary interaction and transition at the section overlap span experimentally

Section overlap spans are locations where the peak contact force appears, which hugely affects the current collection quality. However, there are only a few publications regarding the dynamic behaviour assessment of section overlap spans. Due to the measurement challenge of overlapping contact wires, a measuring method for estimating the contact wires' uplift and the crossing point is necessary. The reasons for the high contact forces and the contact loss rendering arcing at overlap spans need to be investigated. It is significant to study the pantograph-catenary interaction and transition at the overlap span experimentally.

1.5.2 Scope

The scope of the thesis is to develop a vision-based uplift measuring system with a line-tracking algorithm to study the dynamic response of railway catenary systems under regular train operation. A novel line-tracking algorithm focuses on addressing the essential challenge of tracking slender wires without markers against noisy backgrounds. Both numerical and field experiments verify the accuracy, robustness and applicability of the vision-based system.

Part of the scope is the collection of sufficient data to evaluate structural dynamic characteristics of the catenary-pantograph interaction considering both normal and overlap spans. A normal span was chosen to estimate the structural damping variation over one span between two poles. The vibration response data at each dropper is collected separately due to the limited camera number, the telephoto lens employed, and the cropped frame. The structural damping can only be estimated from measurements of existing catenary systems. Thus, the damping results estimated from data collected by the vision-based system are evaluated by comparison to measured damping from the literature.

The measurement challenge of the overlap span is different from that of the normal span. The spatial variation of the dynamic contact wire crossing point was evaluated by measurements of the vision-based system. To evaluate the structural dynamic characteristics, the investigation of the crossing-point spatial variation focused on the transition section distance and the contact wire uplift, with a comparison of single and double pantograph passages.

The collection of many samples for statistical analysis is considered outside the scope of this thesis. A sufficient number of train passages were collected for both normal and overlap span investigation.

1.6 Outline of thesis

Chapter 2 develops a robust line-tracking image processing algorithm to address the essential challenge of tracking wires without markers against a noisy background. Numerical experiments and field application validations have been carried out, and robust and efficient uplift measurements of railway catenary systems are achieved in Oppdal railway station, Norway.

Chapter 3 describes a detailed investigation of the uplift and damping of an existing railway catenary span in traffic using the vision-based line-tracking system. Full-span uplift measurements are successfully achieved to identify damping. The spatial distribution and train direction dependency of the structural damping are presented, and the recommended Rayleigh damping coefficients for numerical models are also proposed.

Chapter 4 studies the pantograph-catenary interaction and transition at the section overlap span experimentally. An overlap measuring method was developed and performed to measure the dynamic spatial vibration of the contact wires' crossing point. The whole process of the dynamic interaction and transition at the overlap span is detailed. The analyses explore reasons for the high contact forces and the contact loss rendering arcing. The important transition section distance, i.e., the length where the pantograph runs on both contact wires, was obtained and compared with the train speed to study correlations.

Chapter 5 concludes the main findings of this thesis and suggestions for future work.

Chapter 2

A robust line-tracking photogrammetry method for uplift measurements of railway catenary systems in noisy backgrounds

Tengjiao Jiang, Gunnstein T. Frøseth, Anders Rønnquist and Egil Fagerholt,
Mechanical Systems and Signal Processing, 144 (2020) 106888.

Abstract

For electrical railways, contact wires are used to ensure stable and continuous power supply to trains operating on the infrastructure. One crucial design parameter used to control the catenary design is the vertical displacement. The traditional uplift measuring equipment of catenary systems usually requires that targets are installed on the wire, and/or that measurement devices are mounted on the support structure of catenary systems or temporary poles. These methods require track access and substantial time and manpower for installation and measurement. Thus, a portable vision-based tracking system is proposed to enable remote, non-contact and non-target uplift measurements of catenary systems. The challenge in measuring the catenary displacement is to detect a linear rigid body in a noisy background environment with a high sampling frequency. To detect the displacement, a vision-based system with a novel line-tracking technique

is used to achieve robust and accurate measurements. The proposed technique is based on a coarse subset and line search and subpixel detection. The line-tracking method is successfully employed for the identification of the important vertical displacements of contact wire in front of a noisy background. The accuracy, robustness and applicability of the proposed tracking method are demonstrated through numerical experiments, the field uplift measurement of the railway catenary system and the identification of the contact wire in a diverse city environment.

2.1 Introduction

Railways are essential to most modern societies as they provide a fast, comfortable, energy-efficient, environmentally friendly and reliable mode of transportation for both passengers and goods. Catenary systems are an important part of modern railways as they provide an inexpensive, clean and continuous power supply to trains operating the infrastructure. The state of catenary systems directly affects the operation of railway systems and thereby society as a whole. One way of improving and ensuring the reliability of catenary systems is to monitor the current state to carry out maintenance on the system before serious faults occur [13,19,58,59].

Excessive vibration of the catenary system can cause contact loss between the contact wires and the pantograph, which not only interrupts the power supply of trains but also causes arcing and speeds up wear [7,60,61]. Thus, it is important to monitor the vibration of contact wires to control the maximum uplift. Moreover, the uplift measurement of the contact wire is one of the most important tests to assess the maximum acceptable speed for new electric vehicles and pantographs [29].

Researchers have developed different methods to measure the displacement response of catenary systems. Laffont et al. [23] used three displacement sensors based on Fiber Bragg Grating (FBG) transducers to monitor the 3D displacement of the contact wire. FBG transducers are mounted on the support structure above the contact wire, and they comprise three mobile rods linked to springs for transmitting the displacement of the contact wire to the transducers. Vázquez et al. [32] used an infrared screen to project the light to pass through the contact wire to a line-scan camera and measure the uplift of the contact wire by the projection in images. Karwowski et al. [30] used laser measuring equipment to measure the uplift of the contact wire. This approach requires a reflective plate installed on the contact wire with a laser displacement meter fixed on the top support structure. Nåvik et al. [24,25] presented a newly developed wireless sensor system consisting of a tri-axis gyroscope, a tri-axial accelerometer and a Digital Motion Processor^{TM}. This needs to be mounted on the wires to carry out arbitrary point field measurements of the dynamic behaviour of railway catenary systems.

All of the above methods meet the resolution requirement for measurement, but they have the common problem of requiring track access and equipment installation on the contact wire or the mounting of the measuring devices to the support structure of the catenary system or the temporary poles. This means that these devices require substantial time and manpower to install while disrupting traffic.

For fixed long-term monitoring, these devices are capable of obtaining the required uplift data. However, inspectors still need more portable measurement equipment that can carry out multi-point measurements more conveniently and quickly without disrupting traffic. For field testing, portability, robustness in varying environmental conditions, low power consumption and the possibility of battery operation play a primary role in the choice of the equipment [62]. Thus, it is necessary to develop a complementary portable and robust device for the uplift measurement, convenient and easy to install and use.

Photogrammetry meets these requirements, and equipment can be mounted at a distance from the railway while uplift measurements are carried out in a non-contact way. Park et al. [29] developed a high-speed image measurement system to measure the uplift of the contact wire. This system uses a template matching technique to track a target installed on the contact wire for uplift measurement. Zou et al. [33,34] used a photogrammetric system with an edge detection technique to measure the uplift of a catenary part in a laboratory. Frøseth et al. [28] used a calibrated stereo camera system to measure the uplift of the catenary system in the field by tracking a well-defined target attached to the catenary wire. However, the general problem, which is that the contact wire is challenging to track without the target in front of a noisy background, has not been addressed.

The digital image correlation (DIC) technique [63-66] is the most common image processing technique used to measure full-field displacements. Non-contact measurement by DIC has been carried out in, for example, experimental mechanics [67,68], biomechanics [69,70], civil engineering [71,72], mechanical engineering [73-78], additive manufacturing [79,80] and aerospace engineering [81-83]. However, for the uplift measurement of a railway catenary wire in front of a noisy background, DIC does not work very well due to the loss of correlation caused by the noisy background. The current paper presents a vision-based tracking system for remote, non-contact and non-target uplift measurements of the contact wire. The challenge to detect a linear rigid body motion in front of a noisy background environment with subpixel accuracy has been addressed by a novel line-tracking technique. In this work, components of the vision-based tracking system are first described. Next, the principles of the line-tracking technique are described in detail. The proposed technique uses two different subpixel detection methods to handle different working conditions to increase applicability.

Finally, the accuracy, robustness and applicability of the line-tracking method are demonstrated through numerical experiments, the field uplift measurement of the railway catenary system and the identification of the contact wire in a diverse city environment. The proposed line-tracking technique can also be modified to be applied to identify and track linear objects in other fields, such as lane line detection and tracking [84], linear welded seams detection [85], or power line detection and inspection [86,87].

2.2 Tracking problem in front of a noisy background

The railway catenary system is a power supply system, the task of which is to continuously transmit electricity through the pantograph-catenary interaction to power trains. The main structural parts of the catenary system are a contact wire, a messenger wire and droppers (occasionally also including a stitch wire) [24], all shown in Fig. 2.1. The contact wire moves on the panhead from side to side as the train goes along the track, as shown in Fig. 2.2. If there is an additional small horizontal motion from the vibration of the wire, this will be negligible for the interaction between the pantograph and contact wire. Therefore, the uplift measurement is more important than the horizontal displacement measurement.

The vision-based tracking system, used to perform the measurements, is set next to the railway and is perpendicular to the contact wire in the horizontal plane ($\beta = 0$). A schematic overview of the uplift measurement and the vision-based tracking system is given in Fig. 2.3. The system consists of a high-speed area scan camera (Basler ACA2000-165 μm), a fixed-focal optical lens (the focal length of the lens can be changed according to the actual condition), a trigger, a laptop and a laser range finder (Leica DISTO™ D8). The entire system is powered by the laptop battery/ power supply. A laser range finder is used to measure the horizontal distance L_H from the system to the catenary wire and the tilt angle α of the optical axis, which are important parameters for camera calibration. The tilt angle α is small but usually not equal to 0 in the field measurement.

Under ideal conditions, the background of the image taken by the camera is uniform, as shown in Fig. 2.4(a). In general, however, the background of the image consists of a nonuniform or noisy background that makes it challenging to identify and track the contact wire, as shown in Fig. 2.4(b). In simple approaches to track the contact wire in front of a noisy background, the tracking algorithm may lose the tracking or mistake, for instance, a tree branch for the contact wire and disrupt the performance of the measurement system. Therefore, it is necessary to impose restrictions on the search for the contact wire tracking. A novel line-tracking technique has been proposed to track the contact wire in front of a noisy background while avoiding the above issue.

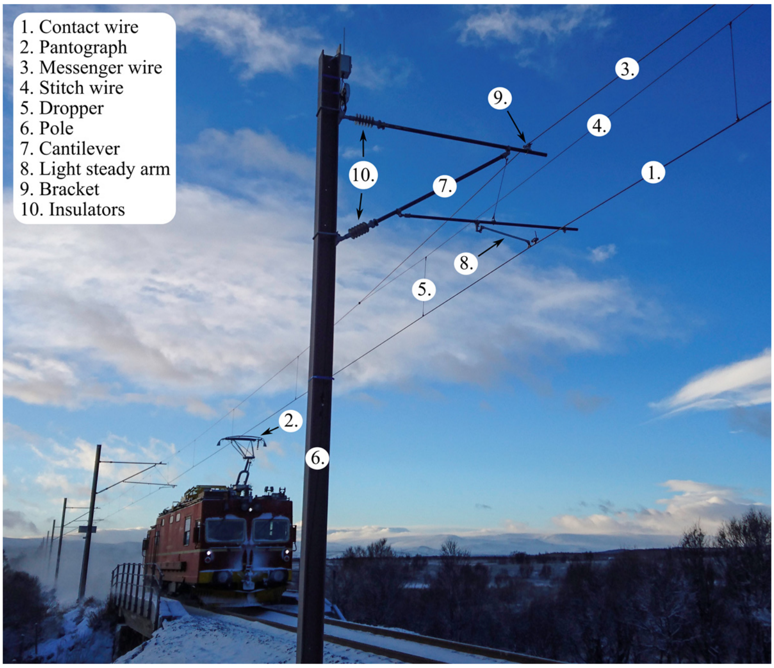

Fig. 2.1. Main structural components of a railway catenary system. Photo: Petter Nåvik/NTNU.

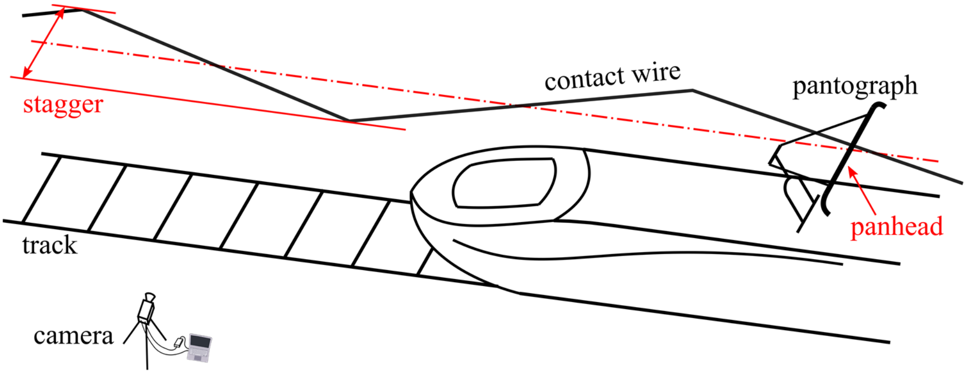

Fig. 2.2. Stagger of the contact wire.

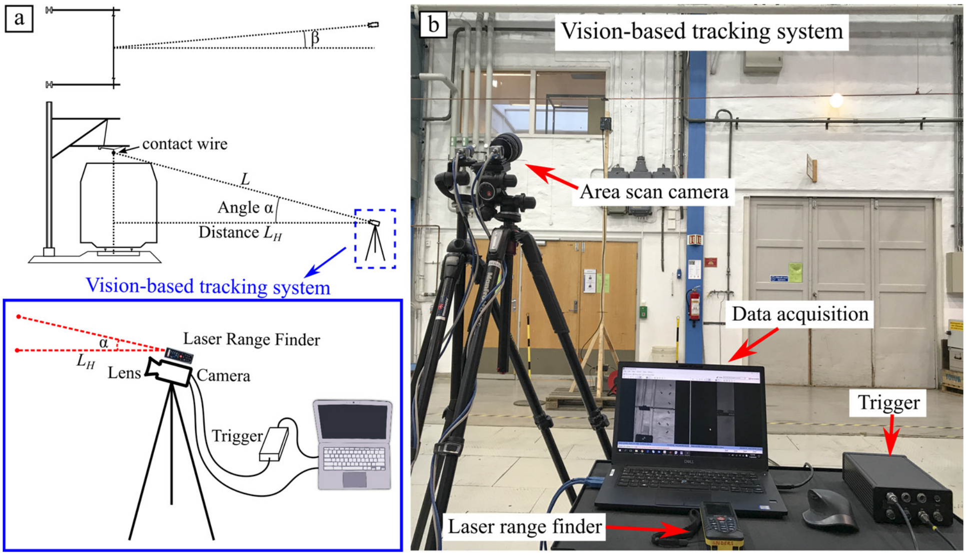

Fig. 2.3. The main components of the vision-based tracking system. (a) A schematic overview of the uplift measurement of a railway catenary system. (b) The vision-based tracking system.

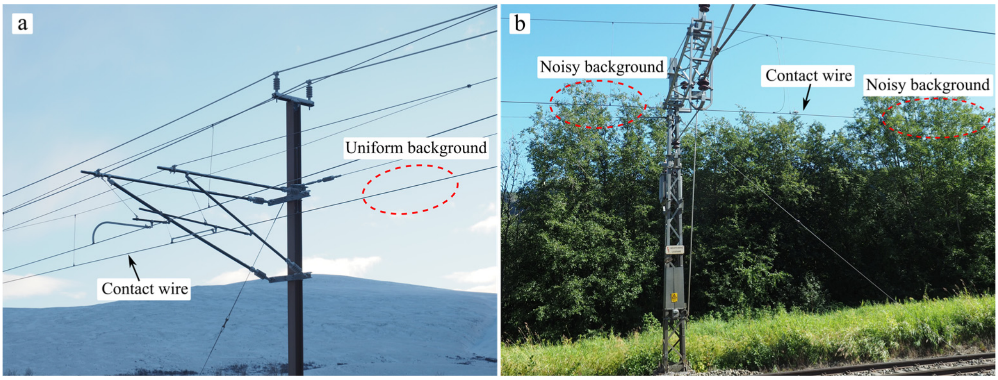

Fig. 2.4. Different backgrounds for the contact wire tracking. (a) Uniform background. (b) Noisy background. Photo: Petter Nåvik/NTNU.

2.3 Line-tracking technique for tracking contact wire in a noisy background

For the purpose of successfully tracking the contact wire in a noisy background, a novel line-tracking technique is proposed. There are three main features of this specific tracking problem that will be used to establish a robust line-tracking algorithm.

A. The contact wire is assumed to be a straight line in all images.

B. The contact wire has a similar intensity magnitude along the wire in monochrome images, and there is generally a sufficient intensity difference between the wire and the background.

C. The contact wire crosses the image from left to right.

Regarding point A, the most common span lengths of contact wires range from 40 to 60 m, where the contact wire is prestressed and suspended by droppers. Vibration measurements require only a short segment (1 m or shorter), rendering the final cropped segment of the contact wire in the images a straight line. Regarding point B, the similar intensity magnitude along the wire in monochrome images means that the intensity value of the contact wire in the images is usually stable, and parts along the wire stay at similar intensity values. For 8-bit images, the intensity ranges from 0 to 255, with 0 meaning black, and 255 meaning white. For most background scenes, there is generally a sufficient intensity difference between the background and the contact wire. For scenes where this is not the case, e.g., tunnel or metro railway systems, artificial lighting may be necessary to successfully track the contact wire. Finally, regarding point C, every measurement setup aims to have the contact wire centred and close to horizontal in the images. Thus, the contact wire always crosses the image from left to right. In certain situations, the camera view is momentarily obstructed during measurements. In these cases, line tracking may still be possible if horizontal sections of the image that are not obstructed are cropped from the original image and used in the line-tracking algorithm.

Based on these three main configuration points, an algorithm for detecting and tracking linear objects in front of a noisy background is proposed. The line-tracking algorithm consists of a coarse search followed by subpixel detection. The coarse search aims to identify the linear objects in noisy background environments. Subsequently, the subpixel detection method aims to find the position of the contact wires more accurately. The workflow of the tracking algorithm is shown in Fig. 2.5.

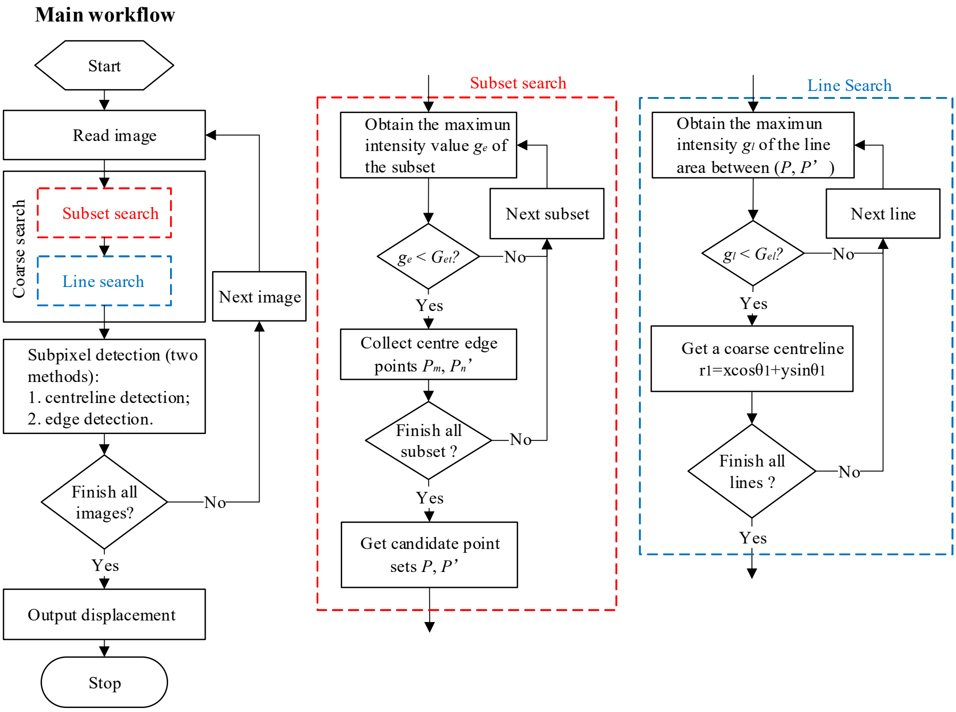

Fig. 2.5. The main workflow of the line-tracking algorithm, including the coarse search method and the subpixel detection method.

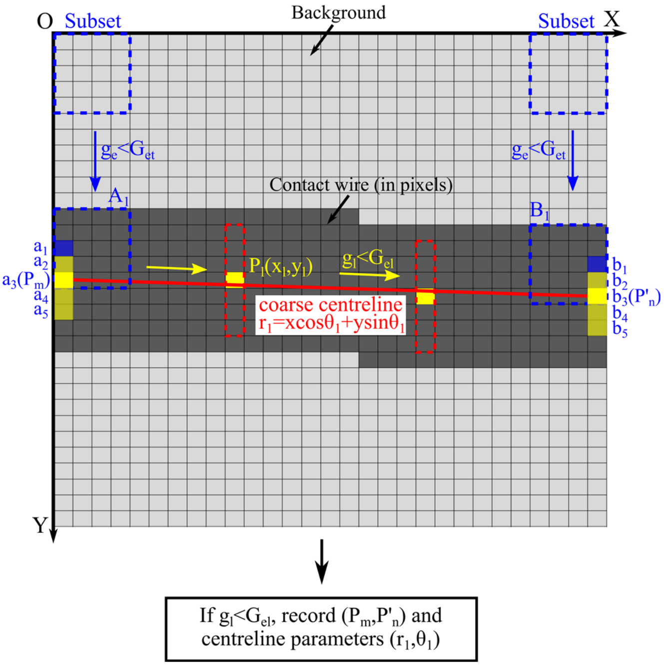

Fig. 2.6. The sketch of the coarse search method, including the subset search and line search.

2.3.1 Coarse search

The coarse search includes two parts: a vertical subset search followed by a line search, where the detailed flow is shown in Fig. 2.5. The image coordinate system is defined with the origin in the upper-left corner of the image. The intensity values in the image are defined by $f(x, y)$ where x is the column number and y is the row number.

The subset is a square region that contains a part of the image. The vertical subset search aims to identify candidate endpoints of the wire in the image. This is carried out by a "sliding" region-of-interest (ROI) or subset moving in the vertical direction at the left and right sides of the image. For each vertical position, the maximum intensity value g_e inside the subset is found. If g_e is less than a threshold G_{et}, the subset is considered an endpoint candidate of the contact wire. The intensity threshold G_{et} can be taken as smaller than the background intensity and larger than the contact wire intensity, usually taken as the average value of both. The idea, here, is that a good candidate subset should be covered entirely by the contact wire. Thus, a subset size smaller than the diameter of the contact wire should be chosen. Initially, this procedure is carried out both on the left and right sides of the image.

In Fig. 2.6, subset A_1 meets the requirement ($g_e < G_{et}$), and the centre edge point a_1 of the subset is obtained as a candidate point. Similarly, b_1 is obtained from subset B_1. Because the subset size is selected to be significantly smaller than the contact wire diameter, several neighbouring candidate points will be obtained as well (illustrated by a_1 to a_5 in Fig. 2.6). Here, the centre point P_m of a_1 to a_5 is calculated and chosen to represent a_1 to a_5 as a single candidate point.

If one of these vertical searches fails to find the candidate points (either at the left or the right side of the image), the algorithm steps a few pixels horizontally towards the centre of the image and carries out a new vertical search. This is done until at least one qualified candidate point is found both for the left and right sides of the image. The vertical search may, however, result in multiple candidate point sets P (left) and P' (right), as illustrated in Fig. 2.7.

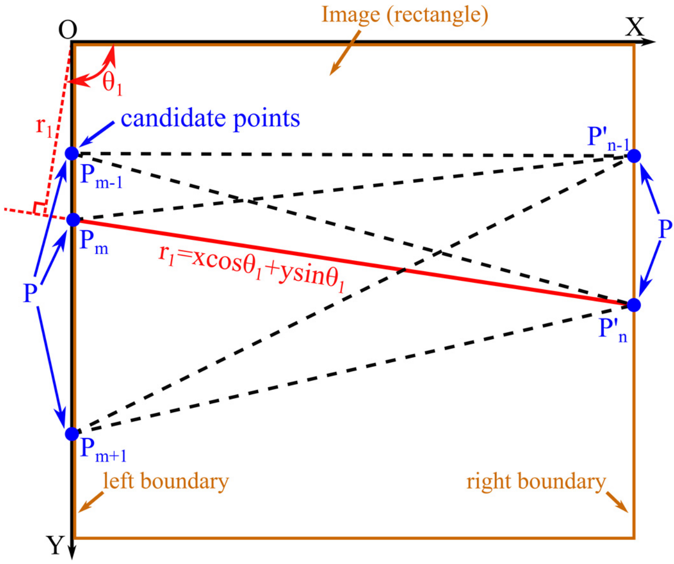

Fig. 2.7. Line search.

The line search aims to reduce the sets of candidate points *P* and *P′* only to contain endpoints of the wire. For all combinations of *P*-*P′*, the maximum intensity value g_l along the line between points in *P* and *P′* is found. The lines are illustrated in Fig. 2.7. As discussed in conditions A and B, the contact wire is assumed to be a straight line in all images with a similar intensity magnitude along the wire. Thus, the maximum intensity value of the line area of the "true" contact wire stays at a low-intensity range. For a noisy background, as is often the case in most working conditions, there are always higher intensity values in the search line area caused by the background sky, leaves, etc.

As shown in Fig. 2.6, every point on the search line $r = x\cos\theta + y\sin\theta$ is represented as $P_l\,(x_l, y_l)$. $r = x\cos\theta + y\sin\theta$ is the linear expression used in the Hough transform [88], shown in Fig. 2.7, where r is the distance from the origin O to the closest point on the straight line, θ is the angle between the X-axis and the line connecting the origin O with the closest point, and the coordinate system is still the original XOY coordinate system.

The search line area between candidate points P_m and P'_n is set by building search windows (red dashed rectangle in Fig. 2.6) centred on $P_l\,(x_l, y_l)$ along the search line. The search window aims to obtain the maximum intensity value g_l of this line area and then compared with the intensity threshold G_{el}. If g_l is smaller than G_{el}, this line is considered the approximate wire position, and the combination (P_m, P'_n) and the coefficients (r_l, θ_l) of the coarse centreline $r_l = x\cos\theta_l + y\sin\theta_l$ are obtained. The height of the search window is set to be a value smaller than the diameter of the contact wire to reduce the probability of detection error. In the example in Fig. 2.6, the height of the search window (red dashed rectangle) is set to 7 pixels, while the diameter of the contact wire is approximately 9 pixels.

The line function $r = x\cos\theta + y\sin\theta$ is used instead of $y = a + bx$ to avoid the problem of calculating the slope when the line is vertical. In this study, the contact wire is assumed to be positioned horizontally in the image. However, by choosing a more general mathematical line formulation, the algorithm can handle lines with arbitrary rotation, which may be encountered when this line-tracking algorithm is applied in other fields.

In conclusion, if the maximum intensity values g_e and g_l for the vertical subset search and the line search meet the requirement of Eq. (2.1), the object is considered to be one of the target linear objects.

$$\begin{cases} g_e < G_{et} \\ g_l < G_{el} \end{cases} \tag{2.1}$$

2.3.2 Subpixel detection

In the coarse search described in the previous section, all points were represented as integer pixel positions. However, the detection of the contact wire can be improved by applying subpixel detection methods. In this study, two different approaches for subpixel detection of the contact wire were applied, i.e., a centreline detection algorithm, and an edge detection algorithm.

Depending on the specific working conditions, one of these two detection methods can be selected to increase the applicability of the proposed algorithm. For example, when intense sunlight shines at the top of the contact wire, the dark areas of the contact wire become smaller, and the centreline detection method may not work very well. However, there can still be sufficient intensity difference between the lower part of the wire and the background, enabling the edge detection method. Moreover, when the background is very noisy and it is challenging to detect the edge of the contact wire, the centreline detection method can be used to track the contact wire. The reason for proposing two different detection methods is to handle different working conditions.

2.3.2.1 Method 1: subpixel centreline detection

The coarse search obtains the locations of the contact wire endpoints at integer pixel positions. The subpixel centreline algorithm then carries out intensity value interpolation in local areas centred on these endpoints.

The method is similar to the previously described vertical subset search. However, here, the intensity values of the subsets are calculated at subpixel positions using bicubic interpolation. The main idea is to use bicubic interpolation to approximate the upper and lower edges of the contact wire to calculate the centre points of the target area accurately. The main calculation process is as follows:

a) Find the vertical search scope (see Fig. 2.8). The search scopes are centred on the endpoints and should be large enough to contain both the upper and lower edges of the wire.

b) A subpixel subset is defined with a suitable size (red dashed rectangles in Fig. 2.8). The subpixel subset should be entirely covered by the wire, so the subset size should be at least smaller than the diameter of the wire. The intensity values of the subset unit are interpolated using bicubic interpolation. The subpixel subset is used to search both the left and right search scopes vertically. For the sake of clarity, a vertical step interval of 0.5 pixels was applied in Fig. 2.8. By following a similar procedure as presented in the coarse subset method, the upper and lower edges of the wire are found with 0.5-pixel resolution. Here, the same criteria as in the coarse subset method were applied, i.e., if the maximum intensity value g_e within a subset at a given position is less than the threshold G_{et}, the subset is considered to be entirely covered by the wire. The centre edge point of this subset is obtained as a candidate point (yellow rectangles in Fig. 2.8).

c) When all candidate points are found in both the left and right search scopes, these candidate points are usually neighbouring and continuous (yellow bands in Fig. 2.8). Therefore, the centre point of the yellow band is chosen to represent these candidate points as a single candidate point for this region. Here, the centre points $P_{centre1}$ (x_{ave1}, y_{ave1}) and $P_{centre2}$ (x_{ave2}, y_{ave2}) are shown in Fig. 2.8 (red rectangles). A line between these two centre points is the centreline $r_2 = x\cos\theta_2 + y\sin\theta_2$. Finally, a point on this centreline can be selected as a tracking point P_{track} (x_k, y_P). x_k is a constant user-defined x coordinate, and the tracking point P_{track} (x_k, y_P) satisfies $r_2 = x_k \cos\theta_2 + y_P \sin\theta_2$.

Note that the uplift measurement of the contact wire needs to measure the displacement in the y-direction only, so the x coordinate of the tracking point P_{track} is set as a fixed value x_k in Fig. 2.8. The centreline may not be the actual centreline of the cross-section of the contact wire because the apparent line is affected by the brightness of the light irradiating on the contact wire. To be more precise, the apparent line is the centreline of the partial area of the contact wire, the intensity value of which is less than the threshold G_{et}. This phenomenon does not affect the detection of the contact wire because the natural light usually does not change frequently, so the centreline detection can always track the same position of the contact wire.

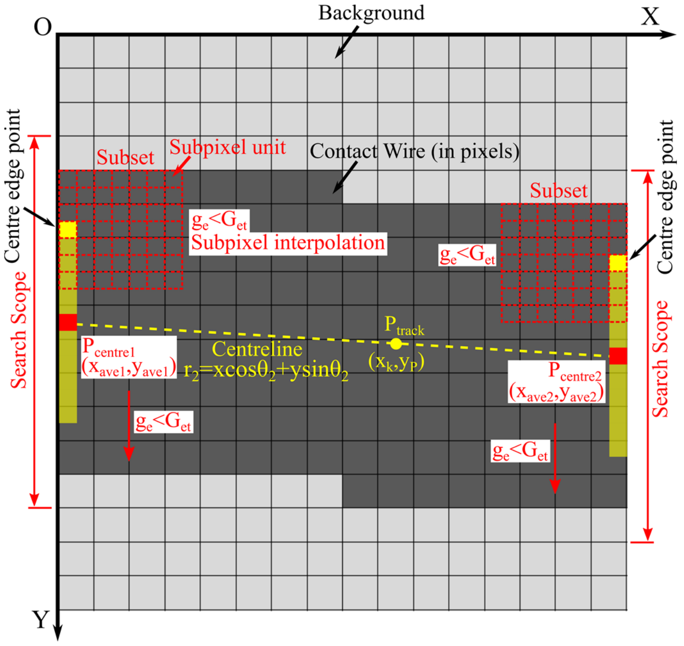

Fig. 2.8. Subpixel centreline detection.

2.3.2.2 Method 2: subpixel edge detection

In contrast to centreline detection, subpixel edge detection focuses on tracking the edge point in the tracking window. The edge is one of the most basic and key features of an image, and edge detection is a main feature extraction method of image analysis. Since the contact wire in the image is considered a straight line, the edge can also be considered a straight line, represented by the equation $y = a + bx$, where the coordinate system is still defined with the origin in the upper-left corner of the image. The subpixel edge detection method based on the partial area effect, introduced in [89], is used in this part.

If an edge passes through the pixel point (i, j), mentioned in [89,90], the intensity value of this pixel is considered as follows:

$$f(i,j)=\frac{AS_A+BS_B}{h^2} \tag{2.2}$$

Where $f(i,j)$ is the intensity value of the pixel point (i,j); A and B are intensity values at both sides of the edge, S_A and S_B are the areas covered by the two intensity values A and B, respectively, in the pixel point (i,j), and h is the side length of the pixel, usually taken as 1, see Fig. 2.9.

Due to $h^2 = S_A + S_B$,

$$f(i,j)=B+\frac{A-B}{h^2}S_A \tag{2.3}$$

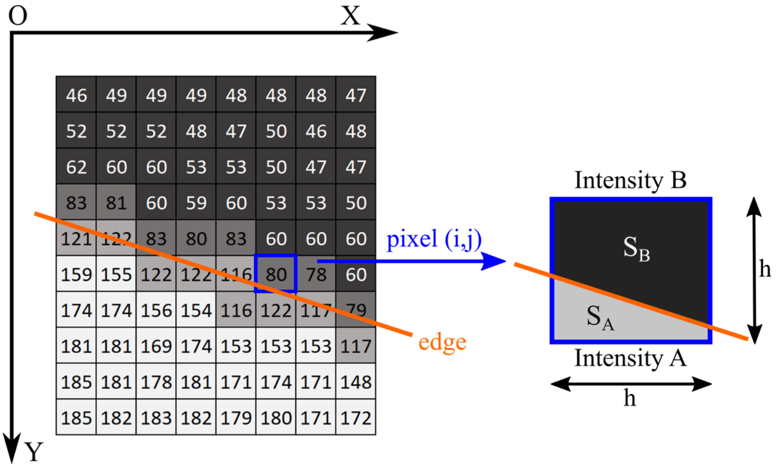

46	49	49	49	48	48	48	47
52	52	52	48	47	50	46	48
62	60	60	53	53	50	47	47
83	81	60	59	60	53	53	50
121	122	83	80	83	60	60	60
159	155	122	122	116	80	78	60
174	174	156	154	116	122	117	79
181	181	169	174	153	153	153	117
185	181	178	181	171	174	171	148
185	182	183	182	179	180	171	172

Fig. 2.9. Origin of the intensity value of the pixel (i, j).

Before starting the edge detection, to reduce the influence of the noisy background, the original image is smoothed using a 3×3 Gaussian smoothing kernel. Gaussian smoothing is used to blur the image by attenuating high-frequency measurement noise and suppressing details in the background. This is achieved by image convolution. The size 3×3 means that the 3×3-pixel points are convoluted by using the 3×3 Gaussian smoothing kernel, and the obtained intensity value is assigned to the central pixel point. The 2D function of an isotropic Gaussian is as follows:

$$G(x,y)=\frac{1}{2\pi\sigma^2}e^{-\frac{x^2+y^2}{2\sigma^2}} \tag{2.4}$$

Eq. (2.4) is used to calculate the weight of each point of a 3×3 Gaussian smoothing kernel, and the sum of all weights should be equal to 1. In general, larger σ means more smoothing, i.e., more details are removed in the image. σ should not be too big because it smears the edge of the contact wire and makes it non-distinct, but it should be big enough such that it attenuates measurement noise and suppresses details in the background sufficiently. In practical applications presented in work for this article, a kernel of size 3x3 with σ =1.5 has shown to give the appropriate level of smoothing and has been used in all results presented in the article.

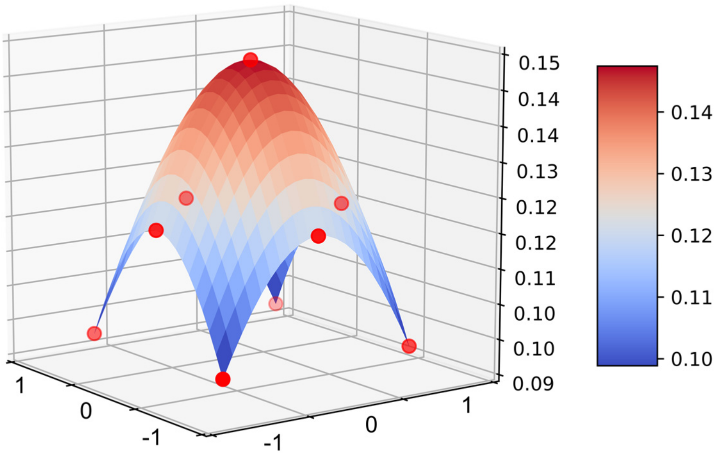

Fig. 2.10. 3×3 Gaussian smoothing kernel.

Fig. 2.10 shows the weight distribution of the 3×3 Gaussian smoothing kernel with σ =1.5. The red dot indicates the weight value of the corresponding point of the pixel on the Gaussian smoothing surface. At the bottom of the coordinate is the 3×3-pixel convolution region. Red means significant influence on the intensity value of the central convoluted pixel, and blue means little influence. The closer to the central pixel, the higher the weight coefficient and the greater the influence. The reason why the kernel size is 3×3 is that the edge detection area is small, and the large kernel will affect the detail quality of the image. To retain the edge intensity gradient, the minimum kernel size is selected.

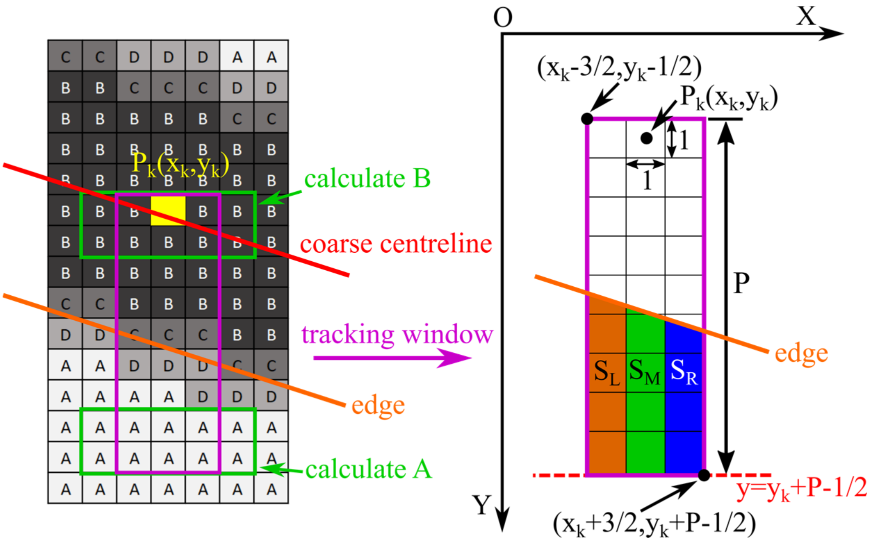

C	C	D	D	D	A	A
B	B	C	C	C	D	D
B	B	B	B	B	C	C
B	B	B	B	B	B	B
B	B	B	B	B	B	B
B	B	B		B	B	B
B	B	B	B	B	B	B
B	B	B	B	B	B	B
C	C	B	B	B	B	B
D	D	C	C	C	B	B
A	A	D	D	D	C	C
A	A	A	A	D	D	D
A	A	A	A	A	A	A
A	A	A	A	A	A	A
A	A	A	A	A	A	A

Fig. 2.11. Subpixel edge detection.

In the previous coarse search, the point P_k (x_k, y_k) was obtained from the coarse centreline (red line as shown in Fig. 2.11, where P_k satisfies $r_1 = x_k\cos\theta_1 + y_k\sin\theta_1$). To improve the smoothing efficiency, the smoothing area can be a small area centred on point P_k (x_k, y_k) and at least larger than the edge detection area. The edge detection area contains the tracking window and the area for calculating intensities A and B. After smoothing, a $P\times3$ tracking window (purple rectangle) with the top edge centred on point P_k (x_k, y_k) is built to detect the subpixel edge. The reason for choosing the lower edge of the contact wire to identify is that the lower edge is usually not illuminated by light, so this edge has a stronger intensity contrast with the background and is easier to identify. The main calculation process is as follows:

First, according to Eq. (2.3), the sum of the intensity values of every column inside the tracking window is calculated:

$$\begin{aligned} L &= \sum_{n=y_k}^{n=y_k+P-1} f(x_k-1,n) = PB + (A-B)S_L \\ M &= \sum_{n=y_k}^{n=y_k+P-1} f(x_k,n) = PB + (A-B)S_M \\ R &= \sum_{n=y_k}^{n=y_k+P-1} f(x_k+1,n) = PB + (A-B)S_R \end{aligned} \tag{2.5}$$

Where L, M, and R are the sums of intensity values of the left, middle and right columns of the tracking window, respectively. P, the height of the tracking window, can be taken as the diameter of the contact wire with integer pixels. In this way, the edge line can be located in the centre of the tracking window. The side length h is taken as 1. S_L, S_M, and S_R are the areas of each column under the edge, as shown in Fig. 2.11, and the expressions are as follows:

$$\begin{aligned} S_L &= \int_{x_k-3/2}^{x_k-1/2} [(y_k+P-1/2)-(a+bx)]\cdot dx = y_k - bx_k + P - a + b - 1/2 \\ S_M &= \int_{x_k-1/2}^{x_k+1/2} [(y_k+P-1/2)-(a+bx)]\cdot dx = y_k - bx_k + P - a - 1/2 \\ S_R &= \int_{x_k+1/2}^{x_k+3/2} [(y_k+P-1/2)-(a+bx)]\cdot dx = y_k - bx_k + P - a - b - 1/2 \end{aligned} \tag{2.6}$$

Then, combining (2.5) and (2.6), we can obtain the parameters (a, b) of the edge line:

$$\begin{aligned} a &= y_k - bx_k + P - \frac{1}{2} - \frac{M-PB}{A-B} \\ b &= \frac{L-R}{2(A-B)} \end{aligned} \tag{2.7}$$

One of the most important factors affecting the accuracy of subpixel edge detection is the calculation of A and B, which are the average intensity values of the background and the contact wire, separately. When the background has smooth luminosity gradients, to reduce the influence of noisy pixels on the overall calculation accuracy, it is preferred to calculate the average intensity values in a large area of the background and the contact wire. Thus, A and B can be calculated separately by adding the intensity values of 2 rows and 5 columns of pixels (or even larger) at the bottom of the tracking window (entirely covered by the background) and at the top (entirely covered by the wire), see the green rectangle in Fig. 2.11. The values can be expressed as:

$$\begin{aligned} A &= \frac{1}{10}\sum_{m=-2}^{m=2}\sum_{n=-1}^{n=0} f(x_k+m, y_k+P-1+n) \\ B &= \frac{1}{10}\sum_{m=-2}^{m=2}\sum_{n=0}^{n=1} f(x_k+m, y_k+n) \end{aligned} \tag{2.8}$$

However, when the background has sharp luminosity gradients, it is preferred to calculate the average intensity values of 2 rows and 3 columns of pixels at the bottom and top inside the tracking window.

When the edge line $y=a+bx$ has been obtained, the edge point P_e $(x_k, a+bx_k)$ can be selected as the tracking point to track the displacement response of the contact wire, while x_k is also the same user-defined constant x coordinate.

Multiple tracking windows may increase measurement accuracy and increase robustness in cases where a single window fails due to, e.g., unfavourable background. In addition, the edge detection requires the edge to cross the tracking window to calculate the integration function Eq. (2.6), so when the edge slope b is too large, the coordinate system should be changed to avoid the edge being close to vertical. However, for contact wire detection, this is not a problem since the contact wire is usually close to horizontal.

The edge detection method in [89] uses traditional derivative masks to compute the intensity gradient for every pixel to determine the location of edge pixels. This edge detection method is adapted to detect the contact wire by using the proposed coarse search method to find the wire edge. This change makes the edge detection more efficient for the specific case of identifying a contact wire from noisy backgrounds.

2.4 Numerical experiment validation

Four sets of numerical experiments, i.e., analysis on synthetically generated image sequences, were conducted to test the performance of the proposed line-tracking method. The first numerical experiment tests the accuracy and stability of the proposed method by tracking the contact wire with precisely controlled motions in front of a noisy background. The algorithm application is introduced in detail in this experiment. The second numerical experiment tests the minimum recognizable diameter of the contact wire in the image and the effect of the diameter change of the contact wire on tracking accuracy. The third numerical experiment adds Gaussian noise to the image to test the noise sensitivity of the tracking method. The fourth experiment simulated the illuminated wire and background to test the performance of the line-tracking method under different light intensity situations.

2.4.1 Tracking accuracy with a noisy background

To demonstrate the accuracy and robustness of the proposed method with a noisy background, numerical experiments with different subpixel moving distances of the contact wire were conducted. An image (540×778 pixels) with many tree branches and leaves was used as a noisy background. To accurately control the subpixel movement of the contact wire, a straight black line was used as the contact wire, as shown in Fig. 2.12. According to the general measurement, the 12-mm diameter of the contact wire was approximately 18.79 pixels in the image with the horizontal distance of 12 m and the focal length of the lens of 105 mm. To increase the difficulty of tracking, the diameter of the introduced black line was reduced to 5 pixels to closely resemble the size of the tree branch.

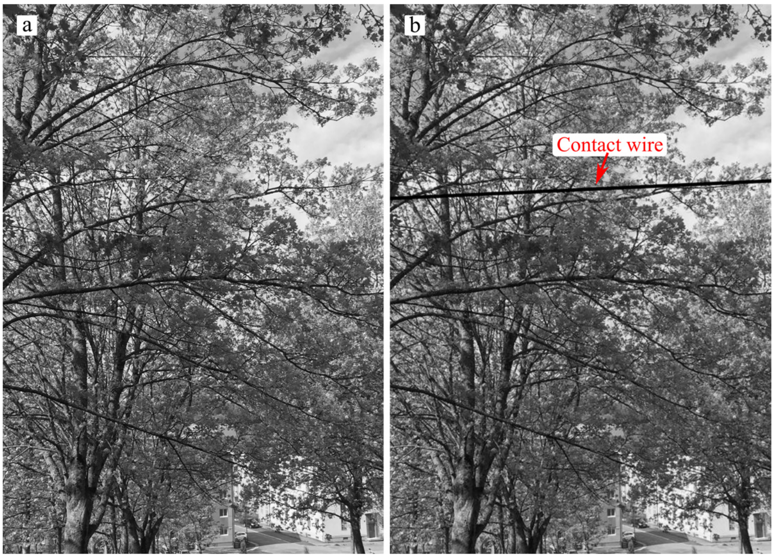

Fig. 2.12. Noisy background image. (a) Original image. (b) A black line is used as a contact wire in front of the noisy background. Photo: Tengjiao Jiang/NTNU.

The contact wire was moved downwards with a displacement interval of 0.1 pixels, meaning that each time a 0.1-pixel movement was completed, a new image with a new contact wire position was saved. The 0.1-pixel displacement was achieved by upscaling the background image by a factor of 10 using bicubic interpolation, drawing the line with the displacement of 1 pixel and finally downscaling the image by a factor 10. With the displacement ranging from 0 to 8.0 pixels, a sequence of 81 images was generated and then processed separately by three different subpixel detection methods, i.e., centreline detection, edge detection with and without Gaussian smoothing.

The detection result of the contact wire in front of the noisy background is shown in Fig. 2.13. The left and right boundaries of the image are set as the coarse search columns. After the subset search, the candidate point sets *P* and *P'* for the left and right boundaries are obtained, respectively. *P* has seven candidate points, and *P'* has one candidate point, where the maximum intensity value g_e is less than the intensity threshold G_{et}. Then, after a line search, the contact wire is successfully identified, and the coarse centreline (solid red line) and point P_k (red point) are obtained, as shown in Fig. 2.13.

Next, the three detection methods process the image separately. For centreline detection, the algorithm detects search scopes at both ends of the contact wire. After the search, the centreline (yellow dashed line) and the tracking point P_{track} (yellow point) can be obtained, as shown in Fig. 2.13.

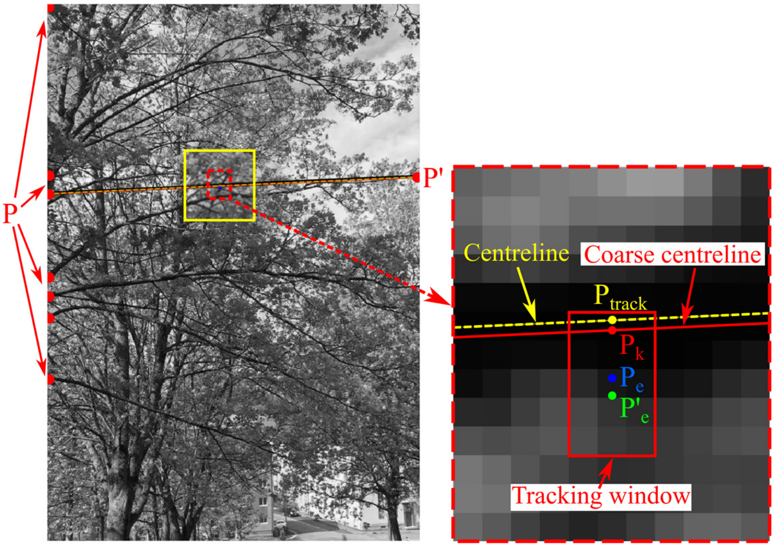

Fig. 2.13. Contact wire detection results.

For edge detection without Gaussian smoothing, the 5×3 tracking window (red rectangle in Fig. 2.13) is built with the pixel point P_k as the centre of the top edge. After edge detection in the tracking window, the edge tracking point P'_e (green point) can be obtained. For edge detection with Gaussian smoothing, first, the algorithm needs to smooth the edge detection area. The edge detection area covers the tracking window and the area of calculating intensities A and B; therefore, the smoothing area should be at least larger than the edge detection area. The Gaussian smoothing kernel with size 3×3 and σ =1.5 has been used in all results presented in the article, and the smoothing effect is shown in Fig. 2.14. In this case, to show the smoothing result more clearly, the size of the smoothing area is selected as 60×60 pixels, shown as the yellow rectangle in Fig. 2.13. Next, building the tracking window and the edge detection are performed in the same manner as in the edge detection without Gaussian smoothing, and the edge tracking point P_e (blue point) is obtained.

After all images are processed and the tracking points P_{track}, P_e and P'_e of the three subpixel detection methods are acquired separately, the vertical displacement of the contact wire can be obtained. Fig. 2.15 shows the measured vertical displacement of the contact wire for the three detection methods with the image serial number. The black line is the exact displacement, and the red, blue and green lines are the displacement results by the centreline detection method, the edge detection method with and without Gaussian smoothing, respectively. Table 2.1 shows the statistical analysis of the displacement error of these three different methods relative to the exact displacement. From Fig. 2.15 and Table 2.1, it can be concluded that the centreline detection has better accuracy and robustness in this numerical experiment. The measured displacement data of the centreline detection fluctuates only slightly around the exact displacement, which shows the stability of this method.

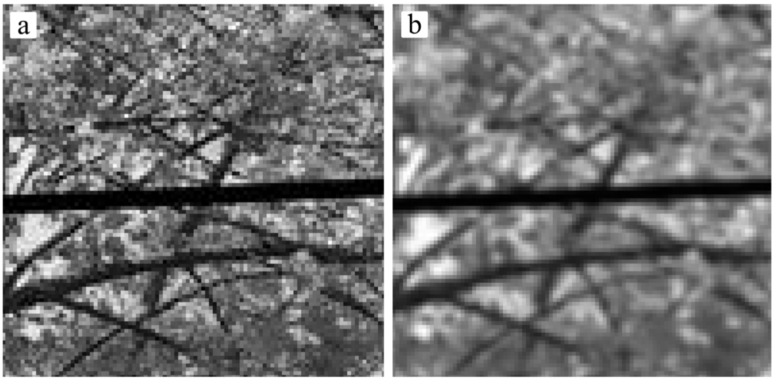

Fig. 2.14. Smoothing effect. (a) before smoothing; (b) after smoothing.

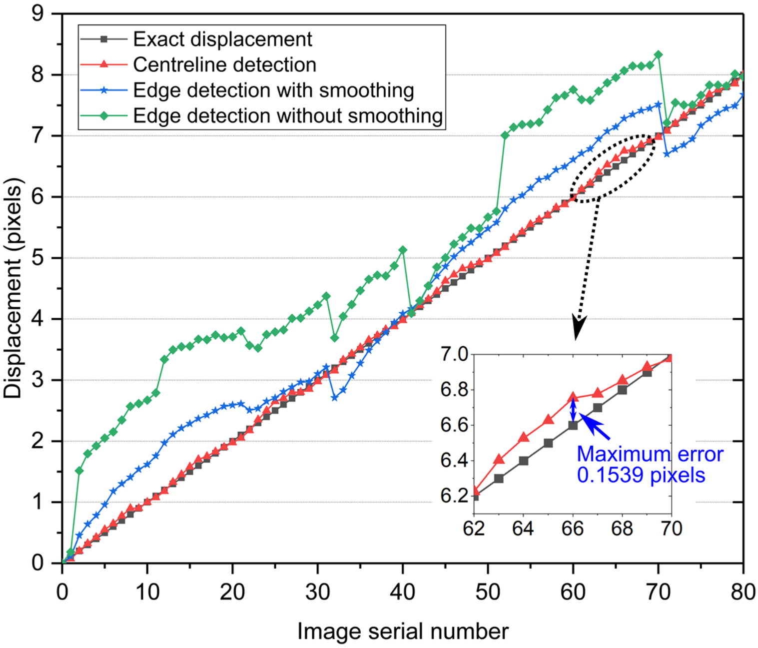

Fig. 2.15. Accuracy comparison of the measured vertical displacement by the three subpixel detection methods.

Table 2.1. Displacement error analysis of the three subpixel detection methods compared with the exact displacement.

	Mean (pixels)	Standard deviation (pixels)	Maximum value (pixels)	Minimum value (pixels)
Centreline detection	0.0456	0.0382	0.1539	0.0000
Edge detection with smoothing	0.4372	0.2235	0.8123	0.0128
Edge detection without smoothing	1.1494	0.6379	2.1961	0.0077

In Fig. 2.15 and Table 2.1, the edge detection with Gaussian smoothing (blue line) and without smoothing (green line) are compared to determine how much the Gaussian smoothing improves the accuracy of edge detection. We can obtain from Fig. 2.15 that the displacement result of the edge detection without smoothing is more volatile and unstable and is susceptible to environmental changes, leading the tracking data to oscillate substantially. By comparing their mean values and standard deviations of the displacement error, it can be concluded that the accuracy and stability of edge detection without smoothing is much worse than that with smoothing. Thus, a proper smoothing has a favourable influence on the accuracy of edge detection, and we suggest using smoothing for edge detection, especially in noisy environments.

2.4.2 Effect of diameter change of contact wire on tracking accuracy

The minimum recognizable diameter of the contact wire in the image is tested, and the effect of the diameter change of the contact wire, related to measurement distance, on tracking accuracy is studied. According to the pinhole camera model introduced in [71], the 12-mm diameter of the contact wire was approximately 22.909 to 2.864 pixels in the image with a lens focal length of 105 mm and the horizontal distance changing from 10 to 80 m, as shown in Table 2.2. Thus, the diameter increased from 3 to 23, with a total of 21 groups. Similar to the first numerical experiment, the black line with different diameters was used as the contact wire in the above background image. To test the robustness of the proposed algorithm, the contact wire was randomly distributed in the image and then moved by the same displacement of 50 pixels. Three detection methods tracked the contact wire, and the displacement error was obtained by comparing the displacement data with 50 pixels. This process was carried out 10 times, and 10 random positions are the same for each diameter group. The mean and standard deviation of the displacement error of each group are shown in Fig. 2.16.

Table 2.2. The diameter of the contact wire at different horizontal measurement distances.

Distance (m)	10	20	30	40	50	60	70	80
Diameter (pixels)	22.909	11.455	7.636	5.727	4.582	3.818	3.273	2.864

In Fig. 2.16, the error bars show the means and standard deviations of the displacement error of three subpixel detection methods. The midpoint is the mean, and the upper and lower caps present the standard deviation of the displacement error. The mean result shows that the displacement error of the centreline detection and edge detection with Gaussian smoothing remains low, but the displacement error of edge detection without Gaussian smoothing is relatively higher. The reason is that smoothing can reduce the negative impact of the background noise on the accuracy of edge detection, so without Gaussian smoothing, the tracking accuracy of the edge detection method is reduced, and the displacement data become more unstable. These results demonstrate that smoothing is helpful to improve the accuracy and robustness of the edge detection method. Through a comparison of the standard deviation, the standard deviation of the centreline detection method always remains low, and far less than the standard deviation of the other two methods.

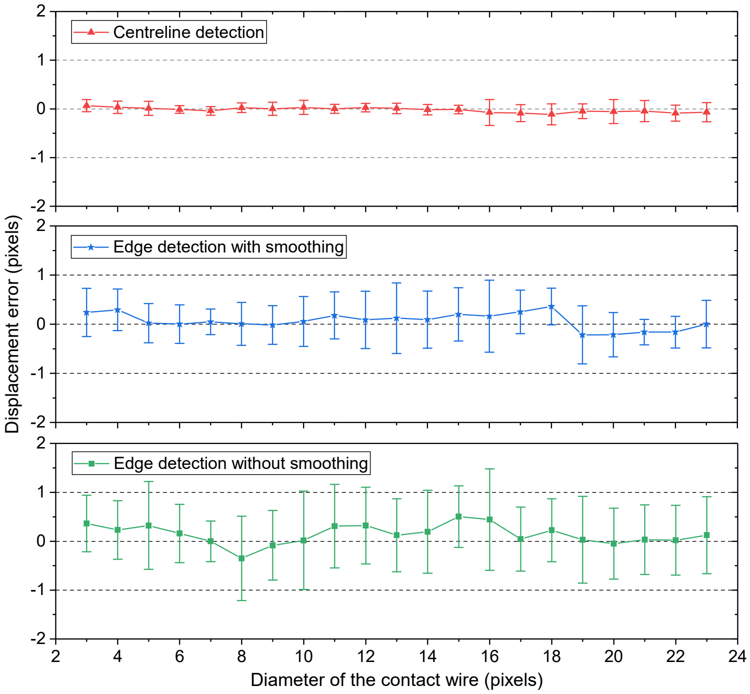

Fig. 2.16. Means and standard deviations of the displacement error of three subpixel detection methods.

The results also show that the three detection methods can successfully detect a minimum diameter of 3 pixels, which is sufficient to meet the regular uplift measurement of the catenary wire, with a measuring distance of less than 30 m and a minimum diameter of 8 pixels. The lower diameter, i.e., 1 or 2 pixels, has been tested, but it is challenging for the algorithm to detect. A longer telephoto lens can also be used to increase the effective measurement distance. The long measurement distance makes remote measurement relatively convenient and applicable, but it should be mentioned that the data instability caused by ultralong distance measurement needs to be noted. In the actual field measurement, a greater measurement distance would be more affected by atmospheric effects, light or other environmental conditions. Through a comparison of the effects of the diameter change on the accuracy, it can be concluded that the diameter change slightly affects the accuracy of the three subpixel detection methods in the case of a noisy background.

2.4.3 Noise sensitivity

The robustness is very important for the tracking method during engineering applications, and the addition of Gaussian noise to the image was used to test the robustness of the tracking method. Different degree of Gaussian noise was added to the image by increasing the standard deviation σ_{noise} of the Gaussian function from 1 to 60 in increments of 5, with the contact wire remaining stationary, as shown in Fig. 2.17. Thus, there are 13 groups for different degrees of Gaussian noise, and every group generates 50 images of a random noise distribution. Fig. 2.17 (d)-(f) show the local areas of (a), (b) and (c), respectively. With σ_{noise} increasing from 1 to 60, it can be seen that the number of noise points increases gradually and that the image, including the contact wire, is increasingly blurred. Especially for $\sigma_{noise} = 60$, there are many noise points on the contact wire, and the difference between the contact wire and tree branches in the background is tiny. Thus, the edge of the contact wire is harder to identify than that for $\sigma_{noise} = 1$.

Then, the three subpixel detection methods were used to identify the position of the contact wire, and the detection error was obtained by comparing the position results with the original position ($\sigma_{noise} = 0$). The signal-to-noise ratio (SNR) was used to estimate image noise in the imaging system. A higher SNR value means that the image quality is better. There are several image-based SNR definitions, and a simple SNR definition [91] is:

$$SNR = \frac{\sigma_{image}}{\sigma_{noise}} \tag{2.9}$$

Where σ_{image} is the standard deviation of the intensity value of the original image, and σ_{noise} is the standard deviation of the added Gaussian noise. Thus, as the standard deviation σ_{noise} of the Gaussian noise increases from 1 to 60, the SNR decreases from 57.11 to 0.95, and the image quality becomes low. The average detection errors of 13 groups with the change of SNR is shown in Fig. 2.18.

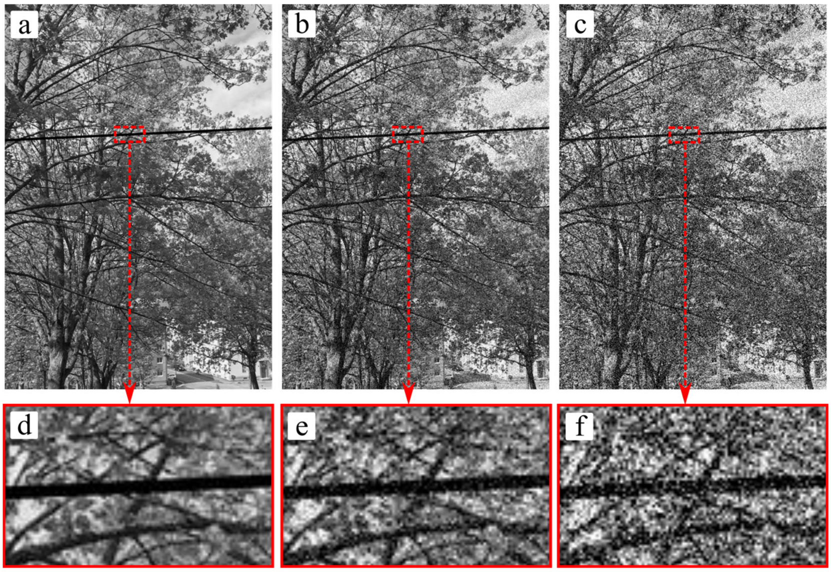

$\sigma_{noise} = 1$
SNR=57.11

$\sigma_{noise} = 30$
SNR=1.90

$\sigma_{noise} = 60$
SNR=0.95

Fig. 2.17. Adding different degrees of Gaussian noise to the image. (a), (d) σ_{noise} =1, SNR=57.11; (b), (e) σ_{noise} =30, SNR=1.90; (c), (f) σ_{noise} =60, SNR=0.95.

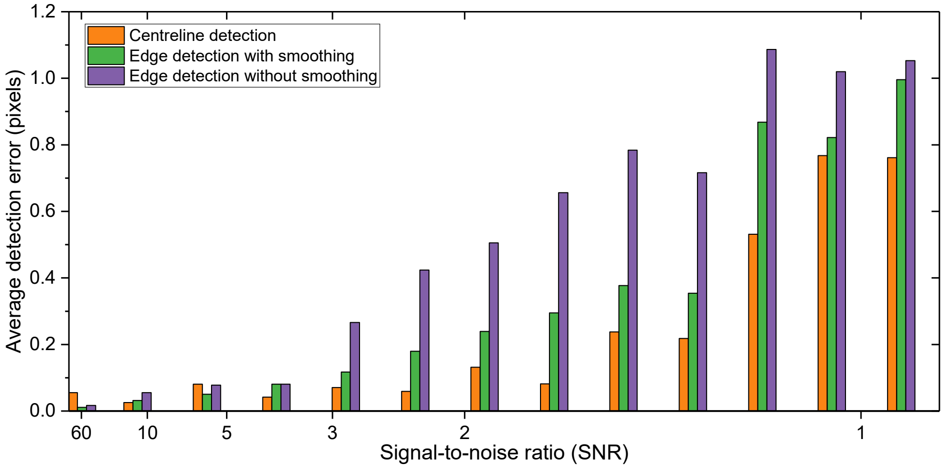

Fig. 2.18. Average detection errors of three detection methods under different degrees of Gaussian noise.

As shown in Fig. 2.18, when the SNR is less than 3, the average detection error of the two edge detection methods begins to increase significantly. In contrast, the error of the centreline detection begins to increase significantly when the SNR is less than 1.5. In general, for the capacity to resist Gaussian noise, the centreline detection and edge detection with Gaussian smoothing are better than that of edge detection without

Gaussian smoothing in this case. By comparing the two edge detection methods, it is shown that Gaussian smoothing is very useful for reducing the impact of noise, confirming edge detection to be relatively robust and accurate. When SNR = 0.95, centreline detection and edge detection can still reasonably accurately identify the contact wire, which shows the robustness of these two methods. In general, the real environment of the uplift measurement of the contact wire is much better than the condition SNR = 0.95. Thus, centreline detection and edge detection are competent for the most general conditions.

2.4.4 Different light intensities

Under different light intensities, the performances of the three subpixel detection methods are tested. An illuminated wire, under intense sunlight, is simulated by changing the intensity gradient from top to bottom, as shown in Fig. 2.19.

When the ambient light changes, the brightness of the background will also change. The light intensity of the background is simulated by adjusting the exposure compensation of a background image in an image processing software. The light intensity has been divided into four groups, exposure compensation + 0.5, + 1.0, + 2.0 and +3.0, as shown in Fig. 2.19. The wire movement is similar to the numerical experiment in Section 2.4.1. The wire was moved downwards with a displacement interval of 0.1 pixels, from 0 to 8.0 pixels, and a sequence of 81 images was generated and then processed separately by three different subpixel detection methods.

Fig. 2.20 is the displacement comparison results. The black line is the exact displacement, and the red, blue and green lines are the displacement results obtained by the centreline detection method and the edge detection method with and without Gaussian smoothing, respectively. Through the comparison, it can be found that the edge detection accuracy increases when the light intensity increases. The reason for this increase is that, as the light intensity of background increases, the intensity difference between the wire and the background becomes larger. The significant intensity difference is beneficial to edge detection.

In some parts of Fig. 2.20, the accuracy of edge detection with Gaussian smoothing performs better than centreline detection, especially for the high light intensity. As mentioned above, the edge detection method is more suitable for the high light intensity situations because the lower edge has an obvious intensity gradient with the background and is easier to detect. This is why both methods have been introduced. Depending on the specific working situations, one of these two detection methods can be selected to increase the applicability of the proposed algorithm.

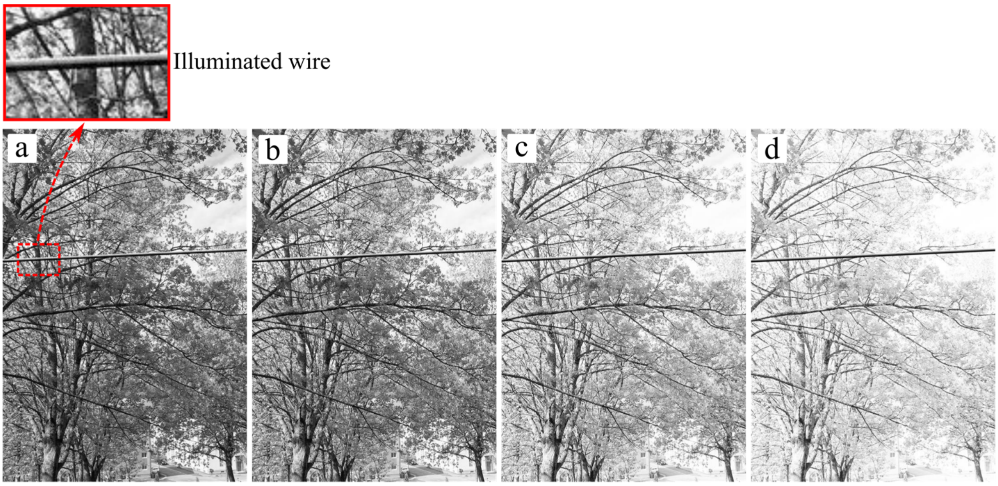

Exposure +0.5 Exposure +1.0 Exposure +2.0 Exposure +3.0

Fig. 2.19. Simulation of different ambient light intensities.

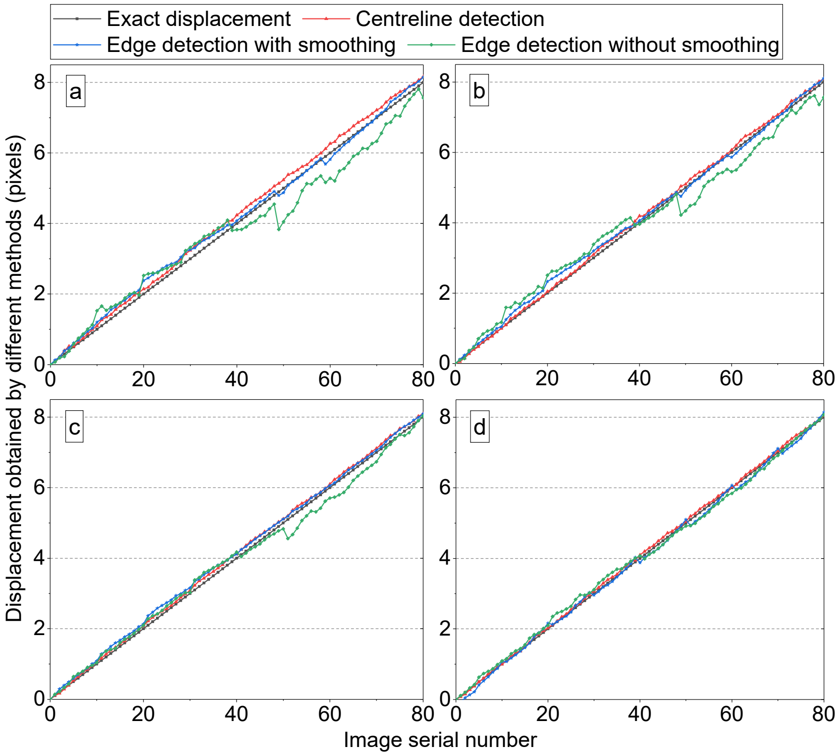

Fig. 2.20. Accuracy comparison under different ambient light intensities. (a) exposure +0.5; (b) exposure +1.0; (c) exposure +2.0; (d) exposure +3.0.

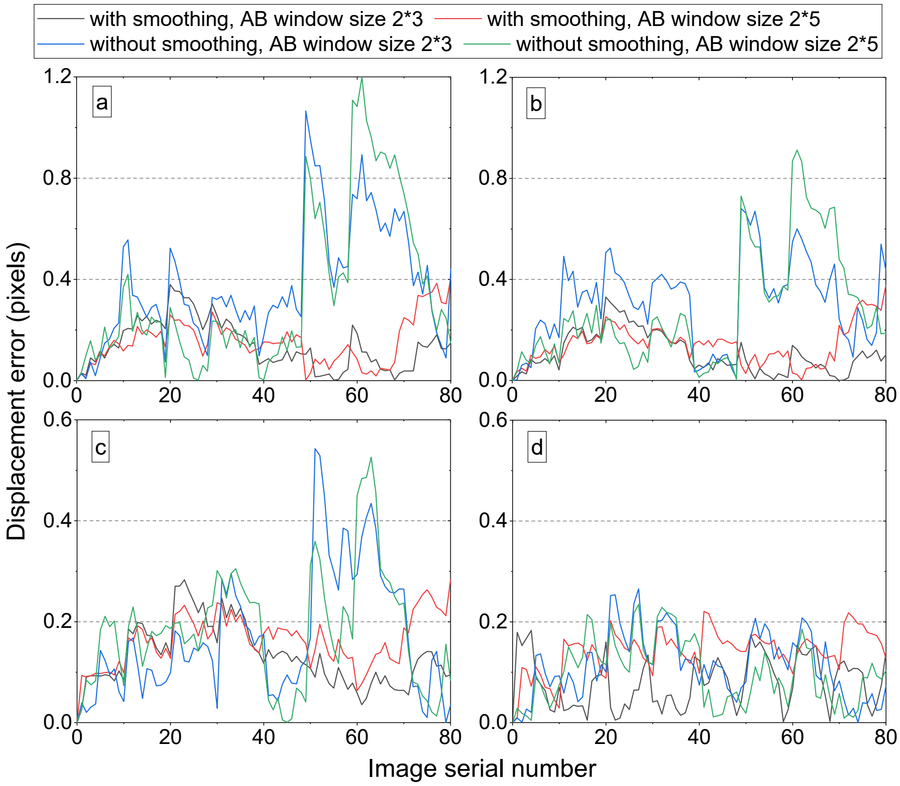

Fig. 2.21. The influence of different window sizes on the edge detection accuracy. (a) exposure +0.5; (b) exposure +1.0; (c) exposure +2.0; (d) exposure +3.0.

As mentioned in Section 2.3.2.2, one of the most critical factors affecting the accuracy of edge detection is the calculation of A and B, which are the average intensity values of the background and the contact wire, separately. Different window sizes will also affect the calculation of A and B. Therefore, under different light intensities, the influence of window sizes on the edge detection accuracy is tested.

Similarly, the light intensity is divided into four groups, and edge detection with and without smoothing methods are still used to detect the contact wire from the above 81 images. However, the different window sizes, i.e., 2 rows and 3 columns, 2 rows and 5 columns, are used for the edge detection methods, separately. Finally, the displacement results are compared with the exact displacement, and the displacement error results are obtained, as shown in Fig. 2.21. The large window is more susceptible to the background intensity change under the sharp luminosity gradients. For the exposure compensation +3.0 group, the influence of the window sizes decreases, because the background is bright, and the intensity gradient of the background decreases. Therefore, it can be concluded that for the background with sharp luminosity gradients, the window size of 2 rows and 3 columns is recommended for the calculation of intensity values A and B.

2.5 Field application validation

2.5.1 Field uplift measurement of railway catenary systems

To test the performance of the proposed vision-based tracking system in an outdoor environment, the field uplift measurement of the railway catenary system was carried out. The accuracy of the vision-based tracking system is tested by comparing the vision-based tracking system with the laser displacement meter. In the field test, the vision-based tracking system was mounted at a distance from the railway and measurements were carried out without contact to the catenary system. A laser displacement meter (DME ODS200) was mounted on the support structure above the contact wire, and a laser reflecting plate was mounted on the contact wire to measure the uplift. A schematic overview of the field uplift measurement is shown in Fig. 2.22.

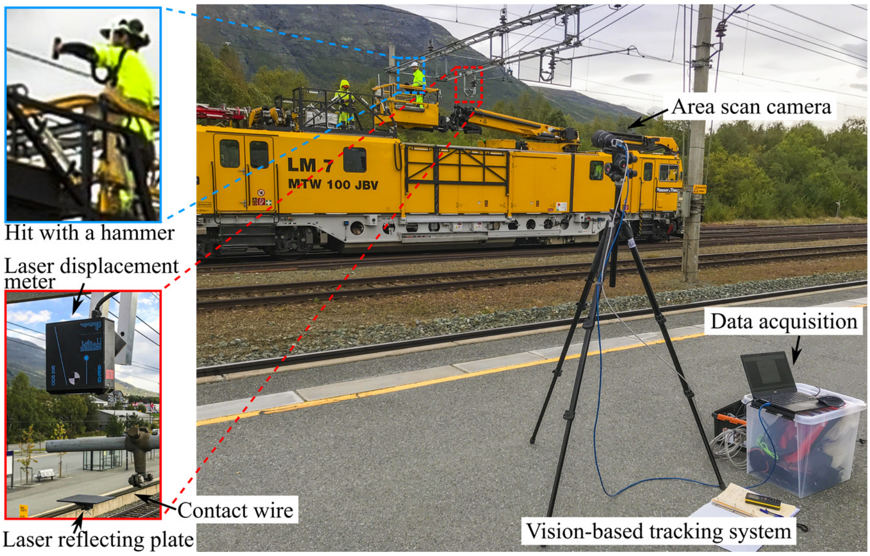

Fig. 2.22. Uplift measurement of a railway catenary system by the vision-based tracking system and laser displacement meter. Photo: Tengjiao Jiang/NTNU.

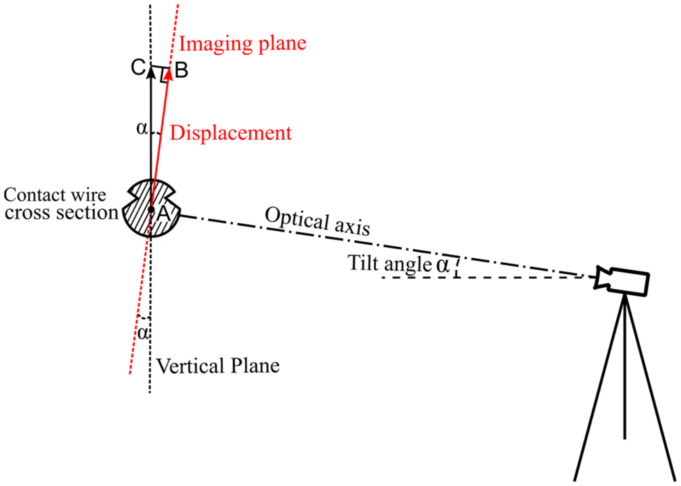

Fig. 2.23. The angle α between the imaging plane and the vertical plane.

In this case, the contact wire was fixedly excited by an impulse model hammer, and then, the uplift data of the contact wire were obtained by these two devices simultaneously with the sampling frequency of 200 Hz. A medium telephoto lens (Sigma AF 105 mm f/2.8 Macro DG OS) was used with a focal length of 105 mm. The horizontal distance L_H between the contact wire and the camera was 7.65 m, and the tilt angle α was 25.35°, measured by the laser range finder. Through the image processing by the proposed line-tracking algorithm, the displacement of the contact wire (in pixels) is obtained. To compare with the laser displacement meter, the displacement in pixels was converted to physical units in millimetres by using the pinhole camera calibration model, described in [71]. Due to the continuous movement of the contact wire throughout the whole image, the scaling factor from the pixel displacement to physical units is not constant and changes slightly. In this case, the scaling factor depends on various parameters, including the image coordinates of the tracking point, the tilt angle α of the camera, the focal length f of the camera lens, as well as the object distance L of the measurement point.

Due to the tilt angle α, the imaging plane usually does not coincide with the vertical plane, and there is also an angle α, as shown in Fig. 2.23. Because the angle α is small and the vibration of the contact wire is mainly in the vertical direction, the vertical displacement can be estimated as $AC = AB/\cos\alpha$. There is only a small error between the real vertical displacement and the estimated one, AC. AB is the displacement in the image plane. The tilt angle, 25.35°, is in the upper range that we can accept in the field measurement.

The accuracy of the laser is approximately 0.05 mm for the measuring range 10 to 30 cm and is considered to be ground truth for this application. Two groups of the displacement data obtained from these two devices are compared with each other in a time series. Both groups obtained data for more than 80 seconds, and the comparison results of the first 20 seconds are shown in Fig. 2.24.

Fig. 2.25 shows that the two measurement methods correlate well, indicating that the accuracy of the tracking system is very close to the laser displacement meter. This is also confirmed by the displacement differences between the two measurement methods in time series, shown in Fig. 2.26, and the distributions of the displacement differences, shown in Fig. 2.27. Fig. 2.27 shows that a Gaussian distribution fits well with the data. The mean values of group 1 and 2 are 0.077 and -0.0036 mm, and the standard deviations are 0.32 and 0.31 mm, respectively. The accuracy of the proposed vision-based tracking system is ± 0.6 mm at 95% confidence, with compensation for the tilt angle. From the application results, it can be concluded that the proposed vision-based tracking system, with the line-tracking method, can successfully and accurately measure the uplift of the railway catenary system.

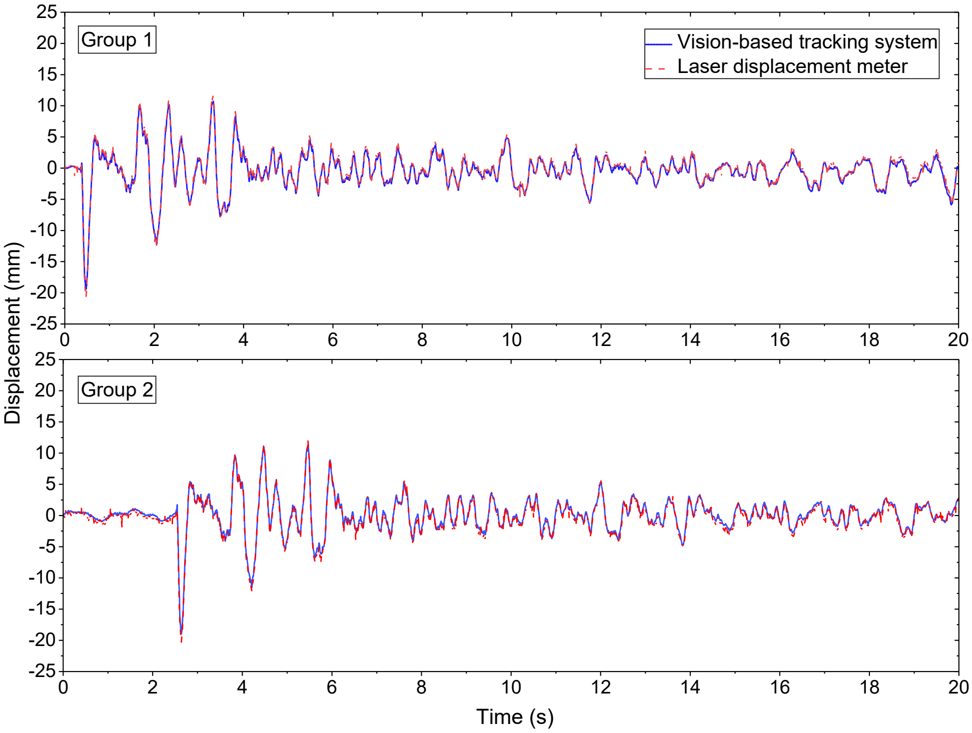

Fig. 2.24. Displacement obtained by the vision-based tracking system and the laser displacement meter.

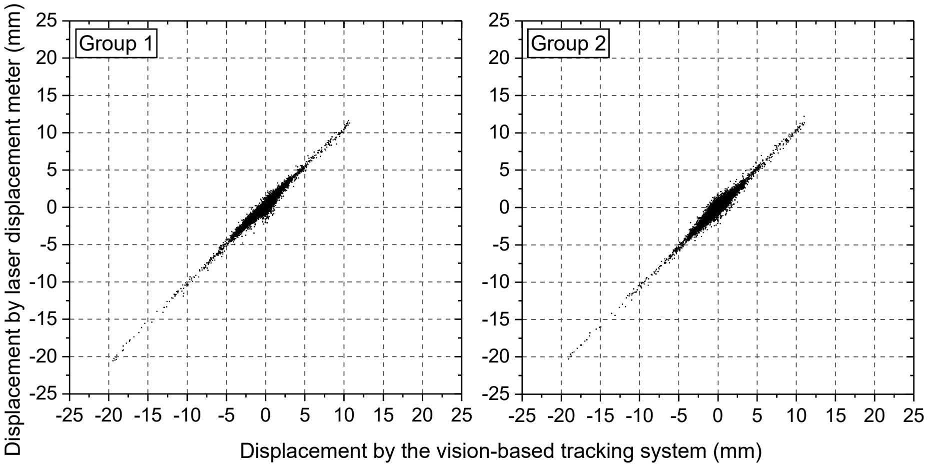

Fig. 2.25. Displacement comparison between the vision-based tracking system and the laser displacement meter.

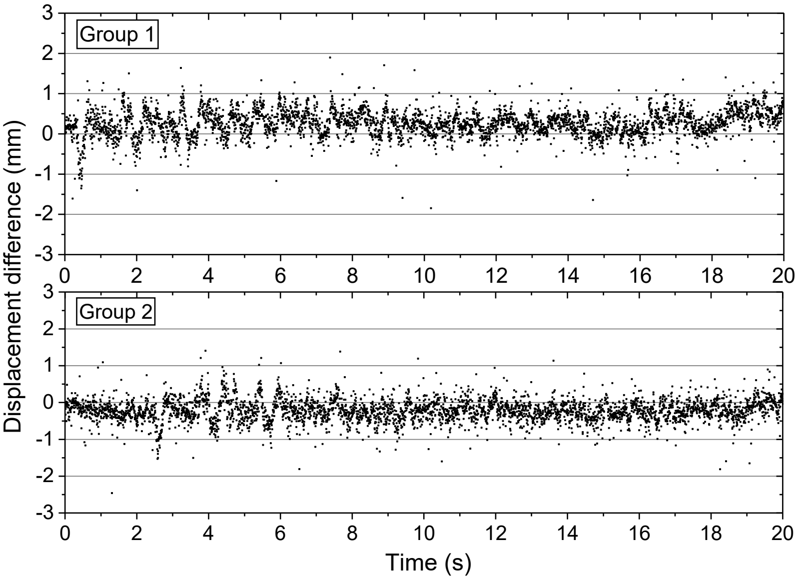

Fig. 2.26. Displacement differences between the vision-based tracking system and the laser displacement meter in time series.

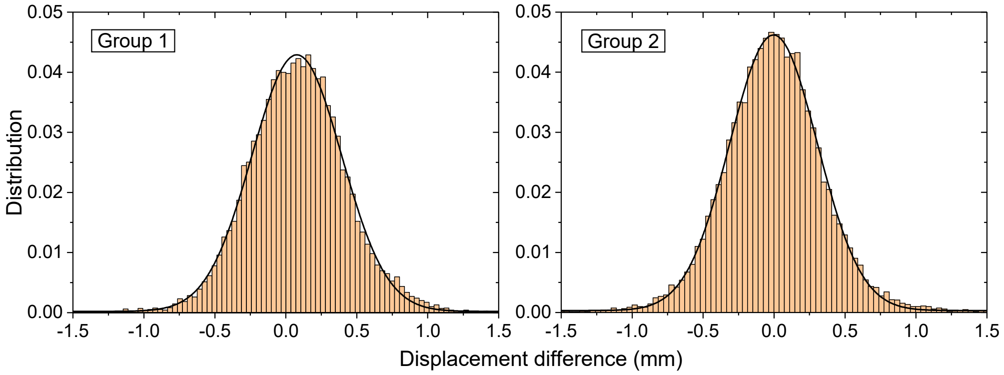

Fig. 2.27. Distributions of the displacement differences between the vision-based tracking system and the laser displacement meter.

2.5.2 Identifying the contact wire in a diverse city environment

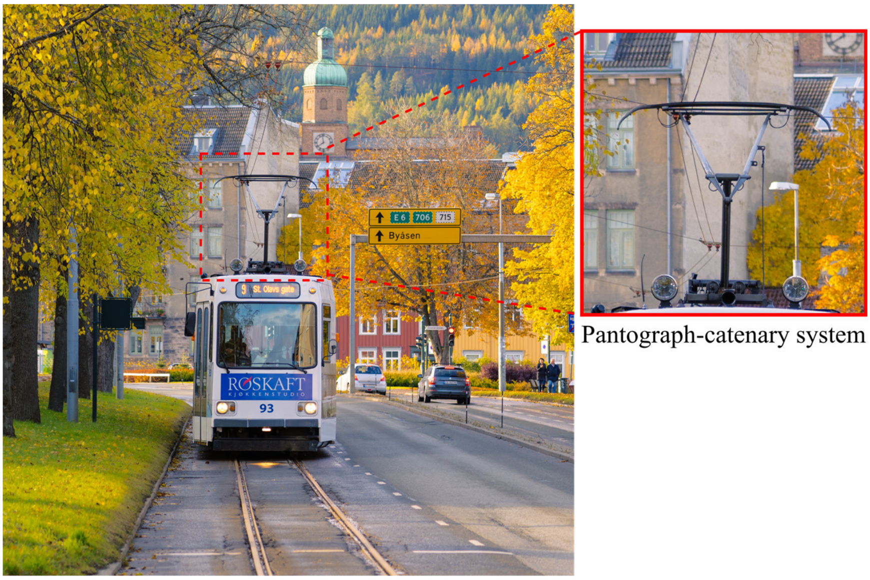

Fig. 2.28. Trams with the pantograph-catenary system. Photo: Tengjiao Jiang/NTNU.

This section demonstrates the ability of the proposed tracking algorithm to identify a contact wire in a diverse environment. Fig. 2.28 shows the Trondheim city tram and its pantograph-catenary system. The city environment provides challenging scenes for contact wire detection, as shown in the examples in the left column of Fig. 2.29. The middle column of Fig. 2.29 depicts obtained images at the contact wire location, and the right column shows the identification results of the contact wire with the algorithm. The right column images also show the candidate endpoints as red dots at the left and right boundaries and the identified contact wire as a red line. The images with many tree branches generally have the most candidate points, see, e.g., the bottom right image in Fig. 2.29. This is expected because these tree branches are similar to contact wires and are correctly identified as candidate points. However, the line search ensures that the contact wires can be found in the noisy background. Fig. 2.29 shows that the contact wire is correctly identified in all example scenes.

After comparing different scenes, the background with tree branches is considered to be the most difficult case because it induces the largest number of candidate points. To test the robustness of the algorithm, more applications with different tree branches as backgrounds are carried out, as shown in Fig. 2.30. The resulting images show that the candidate points on both boundaries increase dramatically as tree branches are identified as possible contact wire endpoints. However, again, after line search, the algorithm has successfully identified the contact wires.

Through the identification of the contact wire in a diverse city environment, it can be concluded that the algorithm can deal with many different types of noisy backgrounds in diverse working conditions. In all applications with different noisy levels, the algorithm can successfully identify contact wires, which shows the robustness of the algorithm.

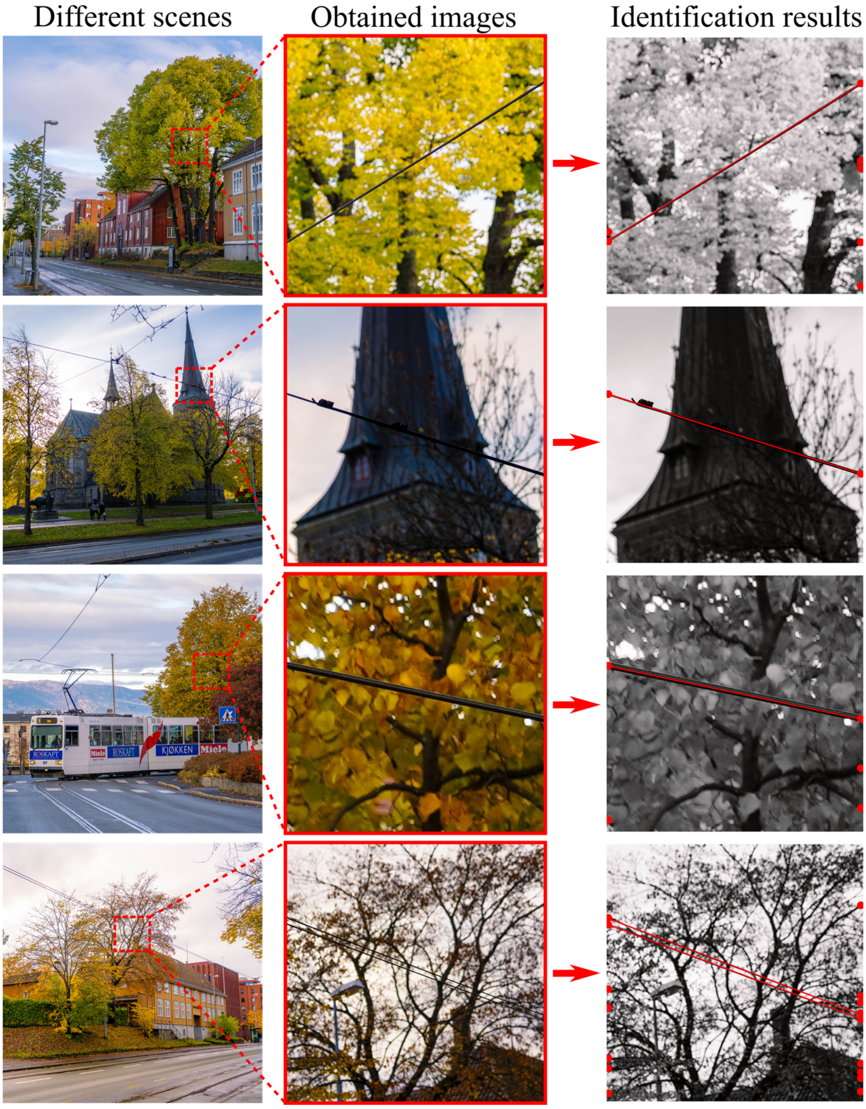

Fig. 2.29. Identification of contact wires. Photo: Tengjiao Jiang/NTNU.

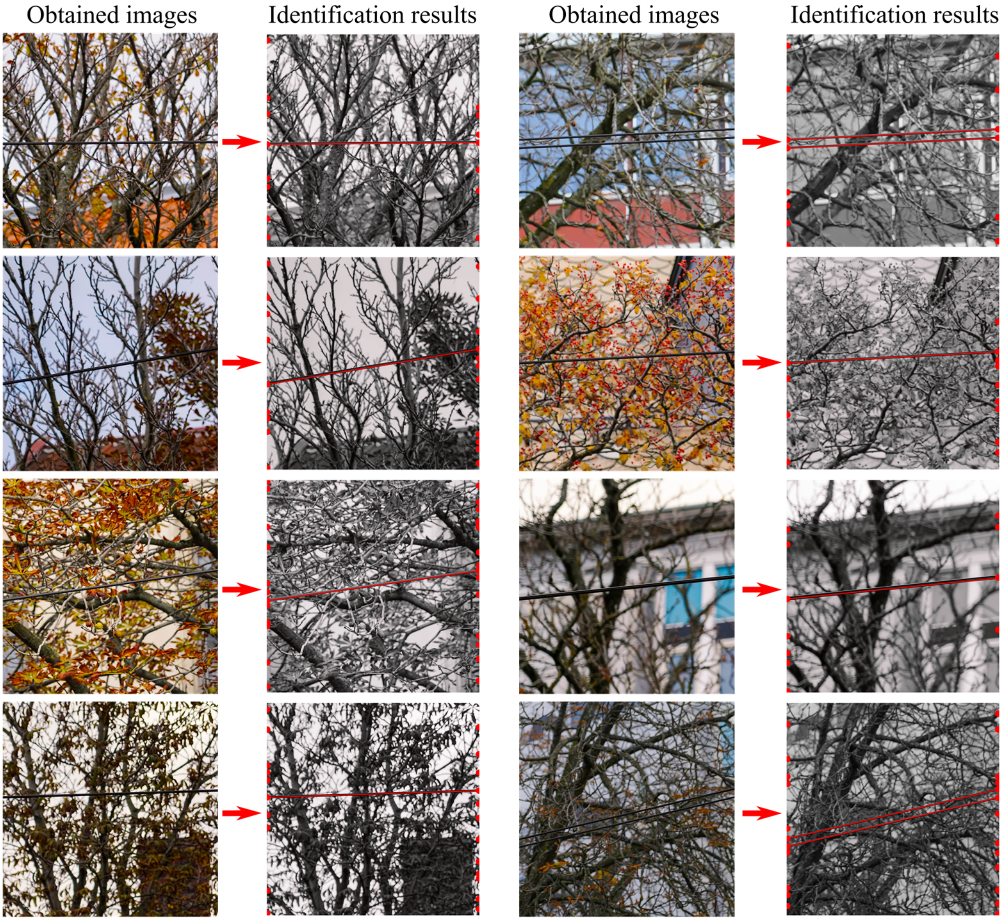

Fig. 2.30. Applications with more complex backgrounds. Photo: Tengjiao Jiang/NTNU.

2.6 Conclusions

A portable vision-based tracking system is proposed to be applied for truly remote, non-contact and non-target uplift measurements of a catenary system. To address the general problem, which is that the contact wire is challenging to track without a target in front of a noisy background, a robust line-tracking technique based on a coarse subset and line search and subpixel detection is proposed to track linear objects in front of a noisy background. Components of the vision-based tracking system and principles of the line-tracking technique are described in detail. Subpixel detection includes two methods, centreline detection and edge detection. These two methods complement each other's application scope, and one of these two subpixel detection methods can be used according to different application environments to improve the applicability of the whole system.

The accuracy, robustness and applicability of the vision-based tracking system are demonstrated through numerical experiments, the field uplift measurement of the railway catenary system and the identification of the contact wire in a diverse city environment. From the obtained results, it can be concluded that the proposed line-tracking method can successfully track the contact wire in front of a noisy background.

Chapter 3

A detailed investigation of uplift and damping of a railway catenary span in traffic using a vision-based line-tracking system

Tengjiao Jiang, Anders Rønnquist, Yang Song, Gunnstein T. Frøseth and Petter Nåvik,
Submitted for journal publication, 2021.

Abstract

For electrified railways, the catenary dynamic behaviour is critical to ensure a robust and steady current collection quality for electric trains. The current collection is achieved as the catenary directly interacts with the pantograph, installed on the car-body roof, to provide an electrical current to the engine. Damping plays an essential role in numerical simulations of pantograph-catenary interaction, especially for multiple pantographs. However, damping estimation of existing catenary sections is recognised as a challenge, and only a few studies have been published with single values of damping estimations. This study aimed to estimate the spatially distributed damping of an existing catenary span through uplift measurements using a vision-based line-tracking system (VIBLITE). A detailed study was performed at critical locations along the catenary span. Sixty-nine single/double-pantograph train passages were acquired during scheduled

train operation. Time series of uplift and acceleration were obtained through a line-tracking image-processing technique. The uplift amplitude was statistically analysed, where the damping ratios were identified using the covariance-driven stochastic subspace identification (Cov-SSI) method. The results were presented as Rayleigh damping coefficients, which shows a notable spatial variation to be considered in numerical simulations. The system was mass proportional dominated, and the coefficients were larger towards the poles compared to the midspan. A small but clear train direction dependency of the damping distribution was observed over the entire span. Thus, it is recommended to consider the spatial damping distribution's influence when conducting future numerical simulations, especially when energy dissipation can be a vital component.

3.1 Introduction

The length of electric railways is increasing in the global railway network. The pantograph-catenary system is an essential part of the electric railway because its responsibility is to supply uninterrupted electricity to power trains [14,92,93]. The pantograph mounted on the top of the trains is in slide contact with the catenary wire to collect the electrical current [16,94]. The main structural components of the catenary system are the contact wire, messenger wire, and droppers, and occasionally also include stitch wires [24], as shown in Fig. 3.1 (a). The pantograph consists of the panhead, upper and lower arms, guiding and coupling rods, lifting device and insulators, as shown in Fig. 3.1 (b).

Dynamic behaviour of the catenary is a direct reflection of pantograph-catenary interaction. The catenary system is considered to be a very lightly damped system [95], and the damping characterisation is significant, especially for multiple pantographs [14,60,96]. The catenary wave excited by the leading pantograph makes the trailing pantograph easily acquire contact loss, thereby causing arcing and disturbing the contact quality. The catenary damping will eliminate the negative effect of wave propagation [18]. Damping plays an essential role in simulations of pantograph-catenary interaction [16,60,96-99], contact force estimation [100], multiple pantograph operations [12,18,101], etc. Damping coefficients used in the literature are shown in Table 3.1. It can be found that much damping-related research applied damping coefficients in simulations but seldom measured damping from built catenary systems. The damping coefficients adopted in simulations are different.

Small damping differences may significantly affect the final simulation results [96]. Therefore, the damping must be estimated to describe the structural behaviour as accurately as possible [24]. Practical Rayleigh damping is suggested to be used in simulations of pantograph-catenary interaction [33,96]. However, for a real catenary, the damping estimation is still recognised as a challenge due to the closely spaced modes and measuring equipment [24,33,60]. The damping ratio is usually considered equal for the whole span in the simulations [102], which does not consider the spatial damping variation over the span.

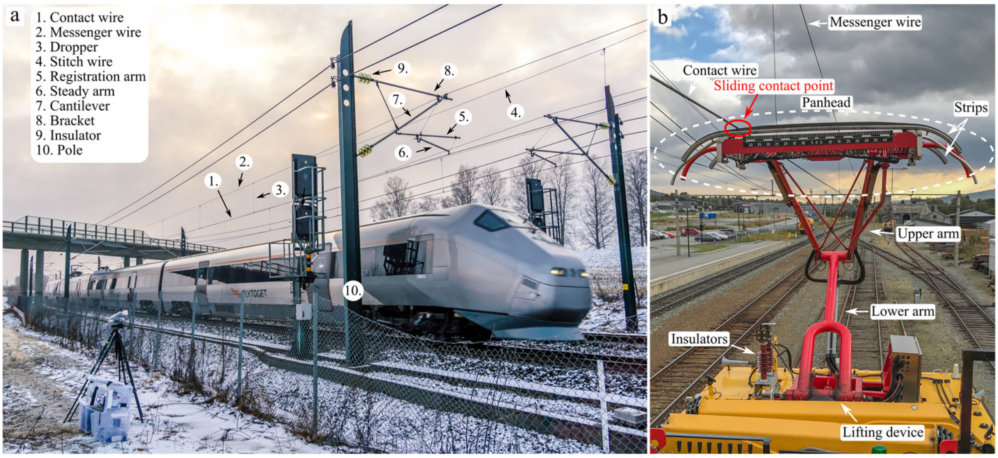

Fig. 3.1. Railway catenary system. (a) Catenary system. (b) Pantograph-catenary interaction. Photography: NTNU/Tengjiao Jiang.

Few studies have been published on the damping estimation of existing catenary sections. The published estimation methods include measuring displacement (uplift) [22,33,96,103] and acceleration [24,26] of the catenary in the laboratory or field. Stickland et al. [22] estimated the damping ratio of a catenary section of the British East Coast Main Line. Drawstring potentiometers connected to the catenary wires were utilised to obtain the displacement of five different locations. An impulse excitation was generated by forcing the wire downwards and then releasing it quickly. Vo Van et al. [26] obtained Rayleigh damping coefficients by using four tri-axis accelerometers installed on catenary wires. Excitation was achieved by dropping masses attached to the catenary wires. Zou et al. [33] performed non-contact measurements via photogrammetry without markers in the laboratory. The damping ratio and Rayleigh damping coefficients were estimated by the continuous wavelet transform (CWT) method. The catenary wire is excited by single-point lifting in the laboratory tests. Nåvik et al. [24] presented a wireless sensor system, consisting of 10 tri-axis accelerometers, to measure the accelerations of catenary wires. The sensor system requires the mounting of sensors on catenary wires. Rayleigh damping coefficients of three existing catenary systems under train operation were successfully identified by using the covariance-driven stochastic subspace identification (Cov-SSI) method.

However, except for Nåvik et al. [24], others measure catenary responses by artificial excitations, which do not reflect the complexity of pantograph-catenary interactions in traffic. The excitation of pantograph-catenary interactions includes forward and backward waves and moving loads caused by the sliding contact of the pantograph. Consequently, it is difficult to present this situation in artificial excitations. Therefore, measuring responses of exciting catenary sections under train operation is a more appropriate way to estimate damping truthfully and accurately.

Table 3.1. Damping coefficients found in the literature, where α and β are the mass and stiffness damping coefficients, respectively, known as the Rayleigh damping coefficients, and ζ is the damping ratio. CW and MW are the contact wire and messenger wire, respectively.

Year	Paper	α_{cw}	β_{cw}	α_{mw}	β_{mw}	ζ_{cw}	ζ_{mw}	Research
2003	Stickland et al. [22]					0.05	0.05	Measurement
2006	Seo et al. [97]	0.01	1e-4	0.05	1e-4			Simulation
2006	Zhang et al. [104]					0.01	0.01	Simulation
2008	Cho [105]					0.01	0.05	Simulation
2010	Bianchi et al. [106]	0	3.25e-3	0	3.25e-3			Simulation
2012	Ambrósio et al. [12]	0	0.0027–0.027	0	0.0027–0.027			Simulation
2012	Ambrósio et al. [60]	0	0.027	0	0.027			Simulation
2012	Jung et al. [100]					0.01	0.05	Simulation
2015	Bruni et al. [96]	0.0125	1e-4	0.0125	1e-4			Simulation
2016	Liu et al. [101]					0.02	0.02	Simulation
2016	Zou et al. [33]	0.02845	0.00274	0.02845	0.00274	0.01	0.01	Measurement
2016	Nåvik et al. [24]	0.062	6.13e-6	0.062	6.13e-6			Measurement

2017	Cazzani et al. [102]					0.02	0.02	Simulation
2019	Gregori et al. [98]	0.0125	0.0001	0.0125	0.0001			Simulation
2020	Antunes et al. [16]	0.0125	0.0001	0.0125	0.0001			Simulation

The above research measures only the response and damping of a few points in the span. To the best of the authors' knowledge, there is no report on the spatially distributed uplift and damping over one span. The damping distribution will promote more realistic simulations of the pantograph-catenary interactions. Particularly for multiple pantograph operation [60,96], the damping distribution may also expand the knowledge that can be used to improve the contact quality of the trailing pantograph to reduce the contact loss.

Except for the closely spaced modes, another challenge in the damping estimation is the measuring equipment. The existing response detection methods mainly involve contact, i.e., the installation of sensors [23-26,92], markers [28-30] or other equipment [22] on catenary wires. These methods require track access and may interrupt train operation. The mass loading induced by sensors, etc., may interfere with the dynamic response of the catenary system. The aerodynamic effect may also be altered. Therefore, a non-contact measurement technique is desired for the uplift measurement and damping estimation.

Computer vision (CV) technology has been widely adopted in civil engineering [36,107,108], mechanical engineering [28,109-114] and aerospace engineering [81,82], etc. For field testing, portability, robustness in varying environmental conditions, low power consumption, and the possibility of battery operation play primary roles in the choice of the equipment [35,37]. The challenges in fieldwork, e.g., the usage of many sensors, cable wiring for power supplies and data transmission, make the contact methods time-consuming, inconvenient and high-cost tasks. CV-based methods can achieve non-contact, long-distance measurement, low costs and labour, and low interference to the daily structure operation [36].

This study aims to investigate the damping and uplift of an existing catenary span under scheduled train operation. A vision-based line-tracking system (VIBLITE), presented in previous work [37], was adopted to achieve a non-contact uplift measurement. The railway catenary span is located on the Oslo Airport line with a train speed up to 210 km/h. To investigate the in-traffic dynamic behaviour of the catenary in detail, the uplift at critical locations along the whole span was measured during scheduled train operation. The critical locations include the dropper clamps (on contact, messenger and stitch wires), midspan point, and steady arm. VIBLITE sampled 69 single/double-pantograph train passages in total throughout the three-day measurement period. The uplift was statistically analysed, and the uplift distribution was obtained. The damping ratios were identified with the covariance-driven stochastic subspace identification (Cov-SSI) method. The spatial distribution and variation of Rayleigh damping coefficients over the span were established and further analysed.

Fig. 3.2 shows the workflow of the uplift measurement, postprocessing and subsequent analysis. The remainder of this article is organised as follows: Section 2 introduces VIBLITE components and a simplified pinhole camera model for camera calibration. In Section 3, the measurement setup and measurement of the train speed are described in detail. Section 4 presents the image processing and results using the line-tracking technique. In Section 5, the uplift and acceleration are evaluated and analysed, and the power spectral density (PSD) at all measuring points is estimated. In Section 6, the Cov-SSI method is implemented to estimate the damping ratios and Rayleigh damping coefficients. Finally, conclusions are provided in Section 7.

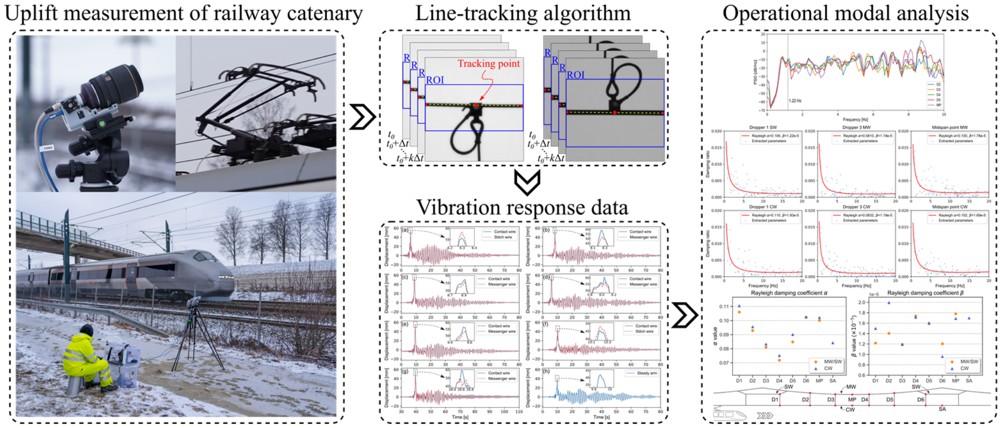

Fig. 3.2. Workflow of the uplift measurement of the railway catenary system using VIBLITE. Photography: NTNU/Tengjiao Jiang.

3.2 Vision-based line-tracking system

3.2.1 System components

A vision-based line-tracking system (VIBLITE) [37] with a corresponding line-tracking image-processing technique [115] was adopted in the measurements, as shown in Fig. 3.3. VIBLITE has been demonstrated to successfully achieve remote, non-track-access, non-contact and non-marker displacement measurements of catenary systems. VIBLITE properly addresses the essential challenge of tracking slender wires without markers against a noisy background. VIBLITE consists of one or several high-speed area scan cameras (Basler ACA2000-165 µm), fixed-focal optical lenses (Sigma AF 105 mm f/2.8 Macro DG OS), a trigger (National Instruments NI USB-6210), a laptop (DELL Latitude 7490) and a laser rangefinder (Leica DISTO™ D8). The selection of lenses of different focal lengths depends on the field conditions. For example, for a horizontal distance L_{H} ranging from 10 – 15 m, a lens with a 105-mm focal length is usually adopted. The laser rangefinder measures the horizontal distance L_{H} from VIBLITE to the catenary wire and the pitch angle θ of the camera, which are important calibration parameters. The camera contains a complementary metal-oxide-semiconductor (CMOS) sensor with an 8-bit 2048 × 1088 pixel resolution. The physical sensor size is 11.3 × 6 mm, and the physical pixel size is 5.5 × 5.5 µm. VIBLITE is powered by the laptop battery/power supply. The laptop controls the sampling rate and exposure time of the camera and stores the images obtained by the camera.

VIBLITE does not require track access nor marker installation on the catenary wires. Therefore, measurements can be performed instantaneously without interrupting the train operation. Due to the advantage of the non-contact measurement technique, the additional sensor masses that may interfere with the dynamic response are eliminated. The VIBLITE accuracy is ± 0.6 mm at the 95% confidence level with a measuring distance of 10 m, as confirmed by comparison to a laser displacement meter in [37].

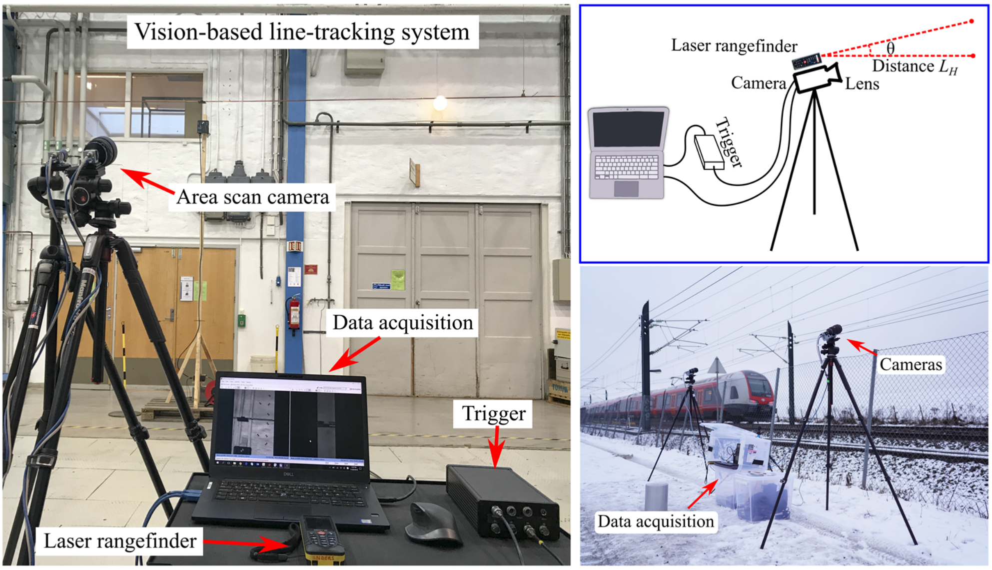

Fig. 3.3. Vision-based line-tracking system (VIBLITE).

3.2.2 Frame-rate improvement

The maximum frame rate (or sampling rate) is limited by frame exposure, readout and transmission time. Frame transmission time is influenced by the USB bandwidth and the size of the frame region-of-interest (ROI). Here, ROI represents the cropped frame on the image plane, which means the pixel data inside the ROI is saved, but that outside the ROI is discarded. Frame ROI improves transmission efficiency and saves the storage cost. The sensor readout time is the sum of all row readout times, so it is influenced by the height (rows) of the frame ROI. Therefore, the sensor readout time will be reduced if the ROI rows are reduced. The reasons are explained as follows.

For the catenary uplift measurement, the vertical displacement is the primary measuring object [37]. Therefore, the frame ROI is usually high in height but small in width, as shown in Fig. 3.4 (a). The blue area is the full-frame (full image plane), and the orange area is the frame ROI (cropped frame). If the camera is rotated 90 º, the ROI size remains unchanged, but the ROI rows are reduced, and then the sensor readout time is further reduced, as shown in Fig. 3.4 (b) and Fig. 3.5.

Fig. 3.5 shows the imaging sensor workflow, which consists of the frame exposure and readout. The small orange rectangle represents the readout time of each row t_{row}. The Basler ACA2000-165 μm camera uses a global shutter sensor [116]. Therefore, the sensor's pixels start and stop exposure at the same time. The sensor readout starts immediately after the exposure stops and continues row by row until all pixel data have been read. For the frame ROI, the sensor readout contains only the rows inside the ROI, which reduces the readout time significantly.

By comparing scenarios with and without the camera rotation in Fig. 3.5, the camera rotation method further reduces the sensor readout time because the sensor readout time is the sum of all row readout times. Therefore, the frame ROI method and camera rotation method can both reduce the sensor readout time and improve the sensor's maximum frame rate.

An effective method to improve the frame rate, for other application fields, is to set the frame ROI with the minimum accepted rows. Whether the camera rotation needs to be adopted depends on the specific applications, e.g., the catenary uplift measurement.

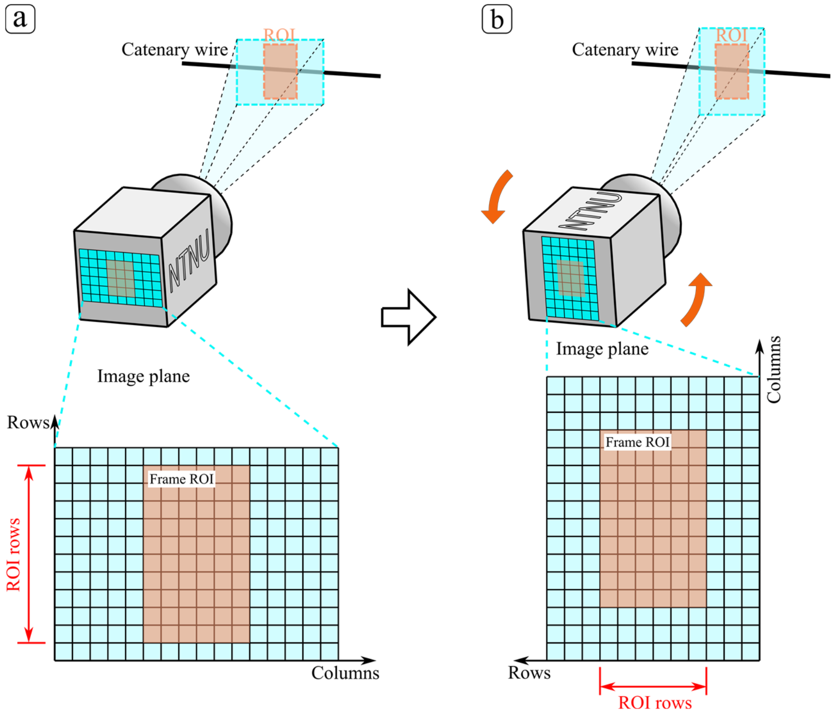

Fig. 3.4. Camera rotation to improve the frame rate.

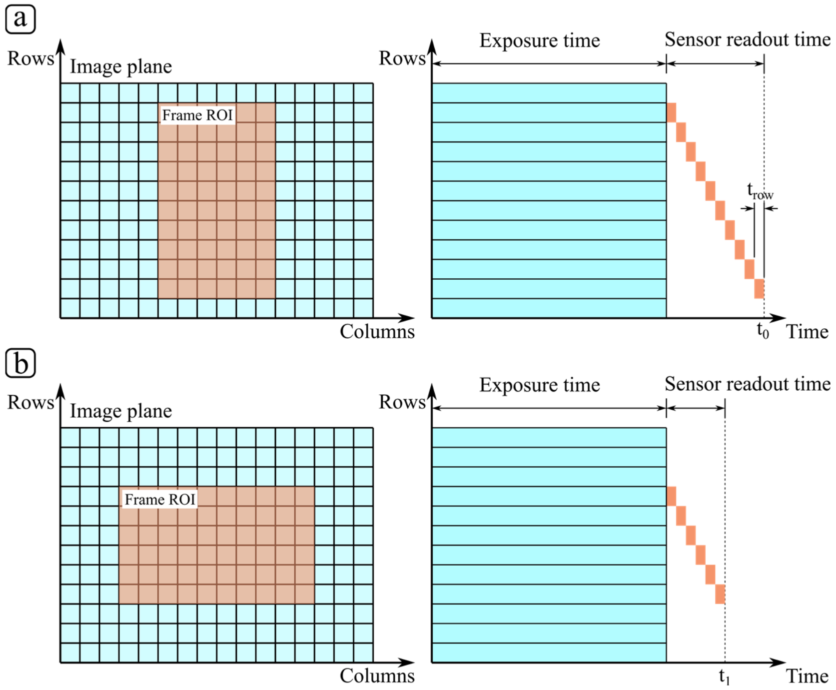

Fig. 3.5. The sensor readout time (a) without and (b) with the camera rotation.

3.2.3 Camera calibration model

Similar to other vision-based measurement methods [108,114,117], a calibration process is necessary for VIBLITE. A pinhole camera calibration model, described in [71], was adapted to the uplift measurement by simplifying the calculation process. A schematic overview of the pinhole camera model is shown in Fig. 3.6. In this case, the scale factor from pixel units to physical units depends on various parameters, including the initial image coordinates (x_0, y_0) of the tracking point, the pitch angle θ of the optical axis, the focal length f of the camera lens, and the distance L from the optical centre to the object [71]. The image plane is the surface of the digital image sensor of the camera, as shown in Fig. 3.6. However, the perspective projection of the object is inverted in the image plane. To simplify the geometric analysis, a virtual image plane is generated, which is located far from the optical centre O at focal length f.

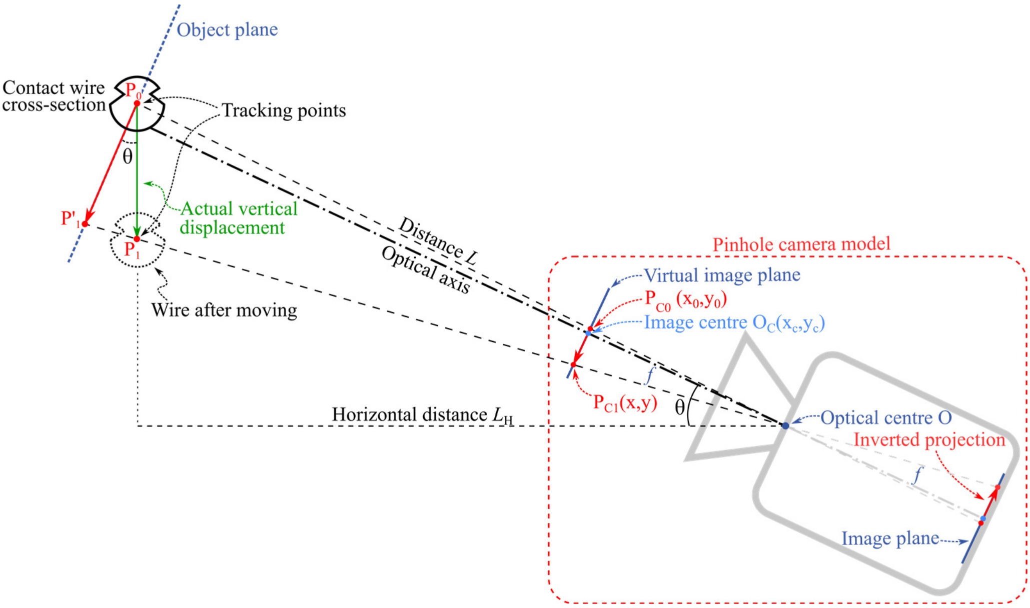

Fig. 3.6. Pinhole camera model of VIBLITE.

As shown in Fig. 3.6, a tracking centre point P_0 of the catenary wire experiences a vertical vibration and moves to a new location P_1, and the projection of the centre point at the new location is P'_1 in the object plane. Their image points move from P_{C0} to P_{C1} in the image plane. According to the homothetic triangle theory, the relation between $P_0P'_1$ and $P_{C0}P_{C1}$ can be expressed as

$$\frac{P_0P_1^{'}}{P_{C0}P_{C1}} = \frac{OP_0}{OP_{C0}} = \frac{L}{\sqrt{[(x_0-x_c)^2+(y_0-y_c)^2]S_c^2+f^2}} \tag{3.1}$$

$$P_{C0}P_{C1} = \sqrt{(x-x_0)^2+(y-y_0)^2}\cdot S_c \tag{3.2}$$

where (x_0, y_0) and (x, y) are the image coordinates of the tracking point in the initial (reference) image and the current image, respectively, point O_C (x_c, y_c) is the centre point of the image plane, S_c is the physical size of each pixel of the image sensor, which is 5.5 µm for the given camera (Basler ACA2000-165 µm), f is the focal length of the optical lens, and L is the object distance from the optical centre to the catenary wire. However, the catenary wire is small, which makes it challenging to use the laser rangefinder to measure the distance L. An alternative and convenient way is to measure the horizontal distance L_H and pitch angle θ. The wire is often photographed at the image centre, so the object distance L can be estimated as $L = L_H/\cos\theta$. The pitch angle θ is usually small in field applications, and the angle $\angle P_0P_1'P_1$ approaches 90°, so the actual displacement P_0P_1 can be estimated as $P_0P_1 = P_0P'_1/\cos\theta$. Hence, the transformation equation of the displacement in pixels into physical units can be written as:

$$P_0P_1 = \frac{P_0P_1'}{\cos\theta} = \frac{L_H/\cos\theta}{\sqrt{[(x_0-x_c)^2+(y_0-y_c)^2]S_c^2+f^2}}\cdot\frac{\sqrt{(x-x_0)^2+(y-y_0)^2}\cdot S_c}{\cos\theta} \tag{3.3}$$

In regard to the uplift measurement of the catenary wire, only the vertical displacement needs to be measured because the vibration primarily occurs in the vertical direction. Therefore, the line-tracking technique is set to track only the vertical movement of the catenary wire in the image. The x coordinate of the tracking point on the wire remains unchanged, both in the reference and current images, so $x - x_0 = 0$. Eq. (3.2) becomes $P_{C0}P_{C1} = |y-y_0|\cdot S_c$. The transformation equation Eq. (3.3) can be simplified as follows:

$$P_0P_1 = \frac{P_0P_1'}{\cos\theta} = \frac{L_H}{\sqrt{[(x_0-x_c)^2+(y_0-y_c)^2]S_c^2+f^2}}\cdot\frac{|y-y_0|S_c}{\cos^2\theta} \tag{3.4}$$

According to Eq. (3.4), two parameters need to be measured in field applications, i.e., the pitch angle θ and horizontal distance L_H. The distance L_H can be measured from 0.05 to 200 m with the Leica DISTO™ D8 laser rangefinder, and the measurement accuracy between 10 and 30 m can be controlled within 0.1 mm. Moreover, the measurement accuracy of the pitch angle is controlled within 0.1°. Hence, the effect of any measurement errors for these two parameters on the measurement accuracy is small enough to be neglected. The coordinates (x, y) of the tracking point in each image are measured by the line-tracking technique.

3.3 Uplift measurement of the catenary span in traffic

3.3.1 Measurement setup

Due to its high flexibility, the catenary vibration is substantial when the pantograph passes. The main objective of the uplift measurement is to control the maximum uplift within a safe range and to study the vibration response of the catenary in traffic. Different catenary systems are implemented in Norway, namely, Systems 20, 25 and 35 [15]. The measured catenary is System 25, which is a section of the Oslo Airport line between Oslo Airport (OSL) at Gardermoen and Oslo downtown, as shown in Fig. 3.7. The tensile section contains 21 spans in total. The 12th span, which has a normal span length and is equipped with six droppers and stitch wire, is selected as the measurement object. The length of the stitch wire is 18.0 m, and the span length reaches 49.8 m. Fig. 3.8 (a) shows the geometry of the measured catenary. The material properties of the contact, messenger and stitch wires are listed in Table 3.2.

System 25 is designed for trains running at a maximum speed of 250 km/h. Two types of high-speed trains run on the airport line, i.e. the Stadler FLIRT Class 74 and GMB Class 71, as shown in Fig. 3.7, with train speeds up to 200 and 210 km/h, respectively.

VIBLITE was set up outside the railway safety fence without disturbing the scheduled train operation. Image series of the catenary wires were obtained as trains passed. The upper and lower clamps of the six droppers, midspan point and steady arm point were selected as the measuring points, as shown in Fig. 3.8 (b). The purpose of selecting the midspan and steady arm points as measuring points was to compare the vibration response of the parts with and without a dropper. The sampling at these two measuring points is important for dynamic analysis [95].

Table 3.2. Material properties.

	Tension [N]	Elasticity modulus [Pa]	Sectional area [mm^2]	Line density [kg/m]	Material
Contact wire	15000	1.20E+11	120	1.07	CuMg
Messenger wire	15000	1.08E+11	65.8	0.596	CuMg
Stitch wire	2800	1.08E+11	34.4	0.31	CuMg

Fig. 3.7. Oslo Airport line. Photography: NTNU/Tengjiao Jiang. Maps courtesy of Kartverket©. Photos of the FLIRT train type courtesy of Norske tog© and the GMB train type courtesy of Flytoget©.

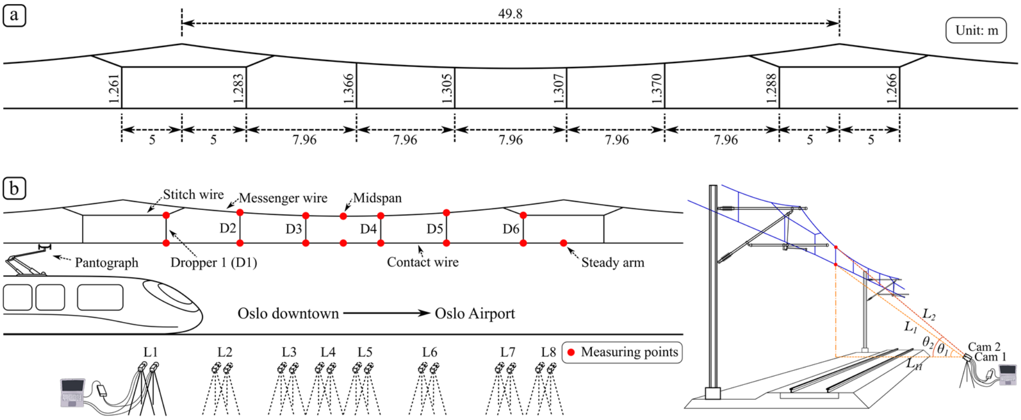

Fig. 3.8. Measurement setup. (a) Size details of the catenary system; (b) measuring points and camera locations.

Two cameras were employed in this study to simultaneously measure the upper and lower clamps. A hardware trigger synchronised the cameras with a sampling frequency of 200 Hz, as shown in Fig. 3.7. One camera can capture only one measuring point due to the telephoto lens employed and the cropped frame. Two cameras were first set at location 1 (L1) to collect the train passage data of the upper and lower measuring points of the dropper 1 (D1), as shown in Fig. 3.8 (b). After a minimum of five single-pantograph train passages was measured, two cameras were then moved to location 2 (L2) to measure the dropper 2 (D2). The same workflow was performed location by location, and at least five single-pantograph train passages were obtained at each location. From L1 to L8, there were eight measuring locations for the six droppers, midspan and steady arm. VIBLITE sampled 69 single/double-pantograph train passages in total throughout the three-day measurement period.

The horizontal distance L_{H} and pitch angle θ of both cameras were measured by the laser rangefinder at each measuring location. The exposure time of the cameras was limited by the sampling frequency and time for the obtained images to be transferred to the laptop, e.g., less than 5 ms at the 200-Hz sampling frequency. Due to the limitation of the USB cable transfer speed at 200 Hz, the pixel resolution of the obtained images was reduced to 500 × 400 pixels.

3.3.2 Train speed

The airport trains contained either single or double pantographs, and the train speed was measured by VIBLITE according to the time interval of the two pantographs passing. The distances between the two pantographs were 105.5 and 107.2 m for the Stadler FLIRT Class 74 and GMB Class 71 trains, respectively. Except for the measured train speed of the double-pantograph trains, the response data of the single-pantograph trains were applied in all results presented in the article. The catenary vibration caused by the two pantographs is different from that caused by a single pantograph.

Table 3.3 summarises the measured train speeds, and the average train speeds were 193.12 and 203.24 km/h for the Class 71 and Class 74 trains, respectively. On this airport line, the two trains attained speeds up to 200 and 210 km/h, respectively. Because the train speed across the measuring span remained relatively stable, the train speed was not included as a variable in the later data analysis.

Table 3.3. Train speeds measured by VIBLITE.

Stadler FLIRT Class 74 (km/h)	188.71	189.64	191.05	191.52	191.52	194.91	195.40	195.40	199.96
GMB Class 71 (km/h)	202.05	202.05	202.05	203.12	203.12	203.65	204.19	204.19	204.73

3.4 Line-tracking image processing

The line-tracking image-processing technique, presented in previous work [37], was adopted to resolve the challenge of detecting the catenary wire against a noisy background at a high sampling frequency. The open-source code has been made available in [115].

In general, there are often trees or buildings on the railway sides, which makes the background of the catenary wire non-uniform or noisy and makes it challenging to identify and track the wire, as shown in Fig. 3.9. For simple approaches, the tracking algorithm may lose tracking or make a mistake, for instance, confusing a tree branch for the catenary wire, and disrupt the performance of the measurement system [37]. Therefore, the line-tracking technique was built for addressing the essential challenge of tracking slender wires without markers against a noisy background.

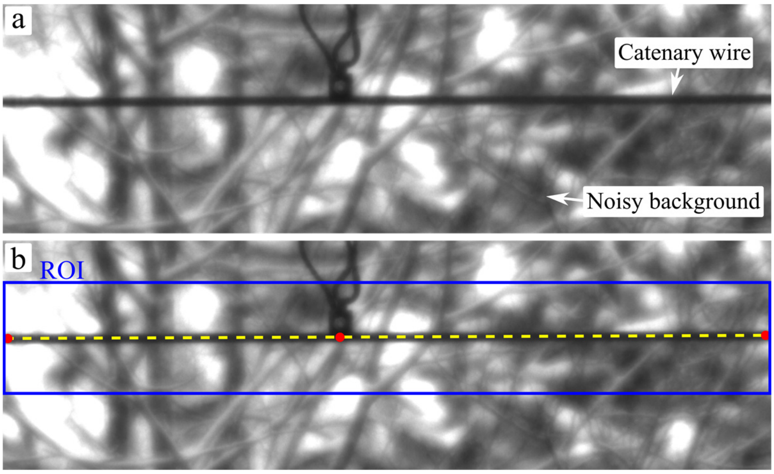

Fig. 3.9. The tracking challenge of the noisy background. (a) Original image. (b) Detection results by using the line-tracking technique. Photography: NTNU/Tengjiao Jiang.

For a better understanding of the line-tracking technique, a brief introduction is appended below. More detailed descriptions can be found in a previous study [37]. The line-tracking technique includes coarse search and subpixel centreline detection. Images are processed by the coarse search first and then processed by the subpixel centreline detection.

The responsibility of the coarse search is to quickly find the line object from noisy backgrounds by comparing the pixel intensity values. This is carried out by a "sliding" subset moving in the vertical direction at the left and right sides of the image to find the candidate endpoints of the line object. The subsets are shown as blue dashed rectangles in Fig. 3.10 (a). Then, a line search between the candidate endpoints from both sides is performed to find the line object. The subsets used in the line search are shown as a red dashed rectangle in Fig. 3.10 (a).

The subpixel centreline detection aims to calculate the centreline accurately by using bicubic interpolation, as shown in Fig. 3.10 (b). The main idea is to use the bicubic interpolation to approximate the upper and lower edges of the line object to calculate the centreline. The found centreline is marked as a yellow dashed line. Finally, points on the centreline can be chosen by users to be tracking points, shown as the point P_{track} in Fig. 3.10 (b).

The obtained image series were processed by the line-tracking algorithm, and the image detection results are shown in Fig. 3.11. A region-of-interest (ROI) is a portion of an image where image-processing operations can be carried out [118]. In this case, the ROI is defined by the user, according to the moving region of the catenary wire, to reduce the search area and improve the detection efficiency, shown as blue rectangles in Fig. 3.11. The left and right sides of the ROI are defined as search columns for sliding subsets to identify the candidate endpoints of the catenary wire. The diameter of the catenary wire is approximately 20 pixels in the images. Considering the intensity change at the wire edge, the subset height is usually defined to be smaller than the wire diameter. The height and width of the subset in the coarse search are defined as 15 and 3, respectively. The detected endpoints are marked as red points on the left and right sides in Fig. 3.11. Then, the subpixel centreline detection uses the bicubic interpolation to approximate the upper and lower wire edges to calculate the centreline. Finally, the centreline was identified and marked as a yellow dashed line in Fig. 3.11. A point on the centreline is chosen to be a tracking point, marked as a red point.

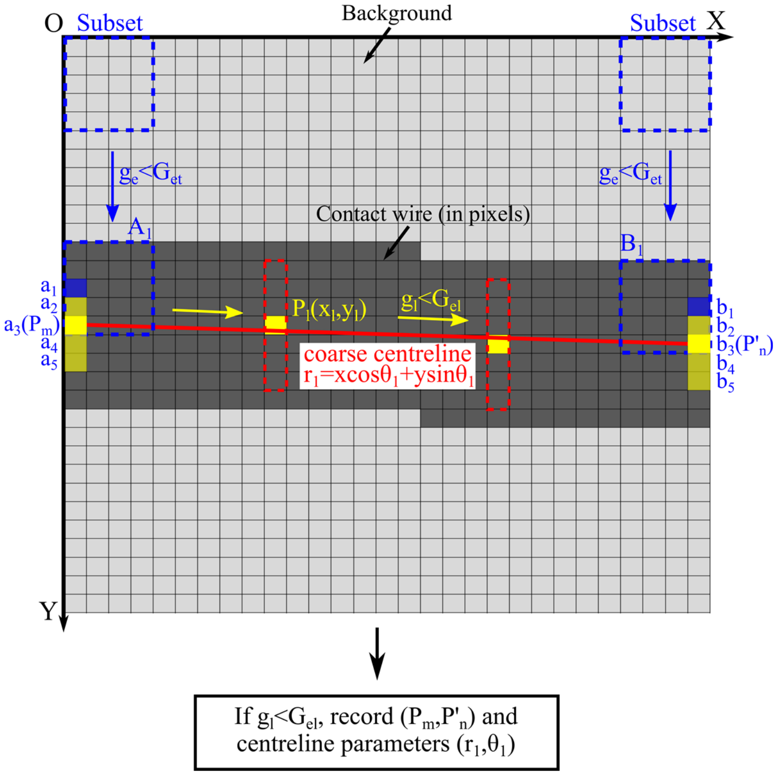

(a) Coarse search.

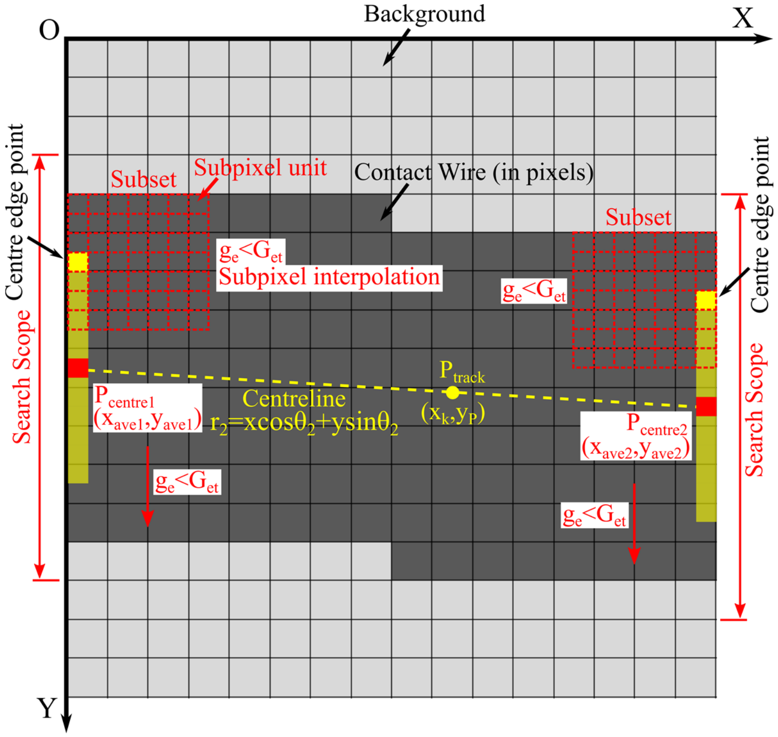

(b) Subpixel centreline detection.

Fig. 3.10. Line-tracking image-processing technique [37], including coarse search and subpixel centreline detection.

After processing the image series of all passages, the displacement data were obtained in pixels. The pinhole camera calibration model, previously described in Section 3.2.3, was employed to convert the pixel displacement into physical units (millimetres). As mentioned above, the parameters used in the calibration model, as shown in Eq. (3.4), include the physical pixel size S_c, the lens focal length f, the pitch angle θ, the horizontal distance L_H, the image coordinate (x_c, y_c) of the centre point of the image plane, and the initial and current coordinates (x_0, y_0) and (x, y) of the tracking point, respectively. All parameters for this case are listed in Table 3.4. The pitch angle θ and the horizontal distance L_H are measured by the laser rangefinder in the field. If the camera location changes, θ and L_H will also change and need to be measured again. Therefore, there are eight sets of θ and L_H for eight camera measuring locations. For example, $\theta = 14.8$ ° and $L_H = 13.122$ m for one of the measuring locations. The image coordinates (x_c, y_c), (x_0, y_0) and (x, y) can be obtained from the above line-tracking technique. After the calibration by Eq. (3.4), the displacement in millimetres can be obtained.

Table 3.4. Parameters of the pinhole camera calibration model.

S_c	f	θ	L_H	(x_c, y_c)	(x_0, y_0)	(x, y)
5.5 μm	105 mm	Measured from field		Obtained from line-tracking technique		

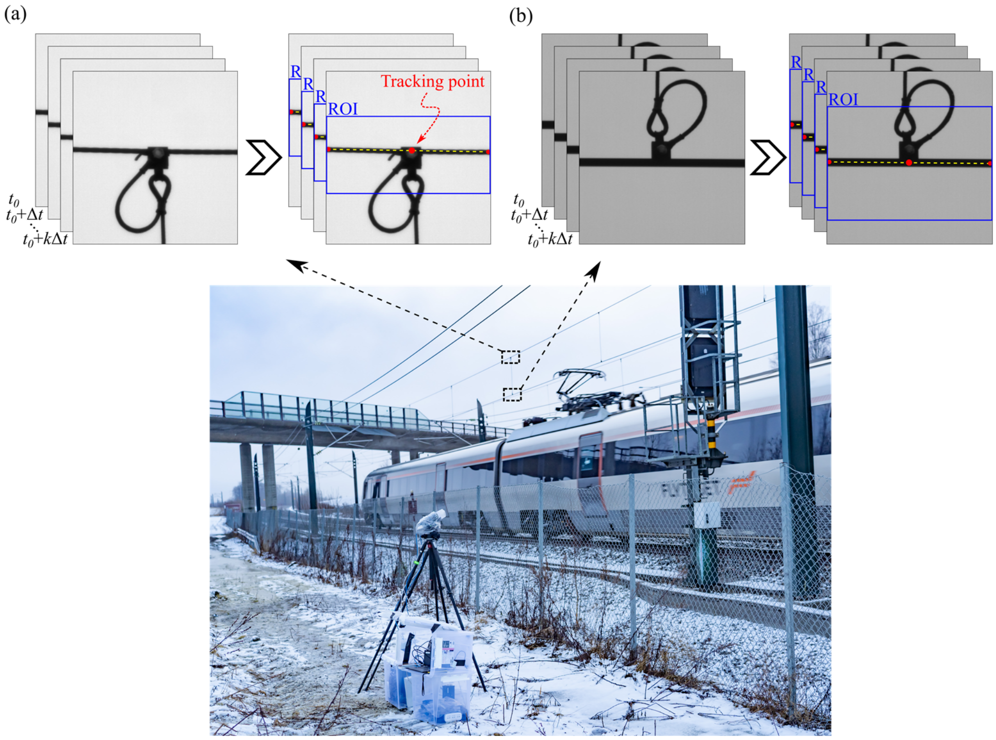

Fig. 3.11. Obtained images. (a) The messenger wire and its detection results; (b) the contact wire and its detection results. Photography: NTNU/Tengjiao Jiang.

3.5 Response assessment

3.5.1 Uplift assessment

The displacement results at all measuring points are shown in Fig. 3.12. A displacement comparison between the contact and messenger wires (or between the contact and stitch wires for droppers 1 and 6) is shown in Fig. 3.13. The comparison results reveal a good synchronisation between the contact and messenger wires or the stitch wire. In regard to droppers 2 – 5 and the midspan point, the maximum displacement of the contact wire was larger than that of the messenger wire. The maximum uplift of the contact wire at the steady arm point should not exceed the safety value of 120 mm at train speeds exceeding 200 km/h, according to the Norwegian National Rail Administration [20]. The maximum uplift was 53.90 mm at the steady arm in all investigated cases, which is within the safe range.

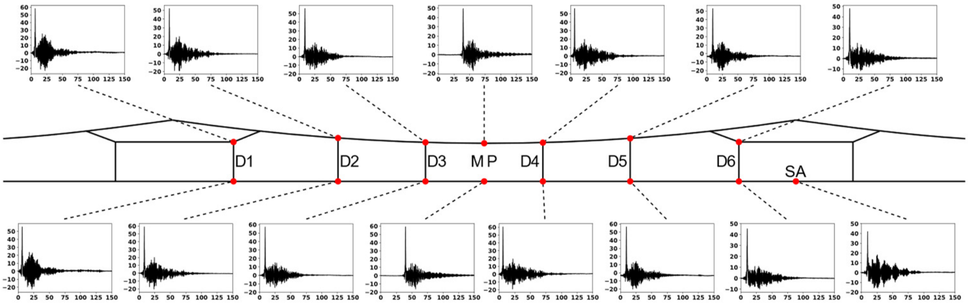

Fig. 3.12. Displacement results at all measuring points.

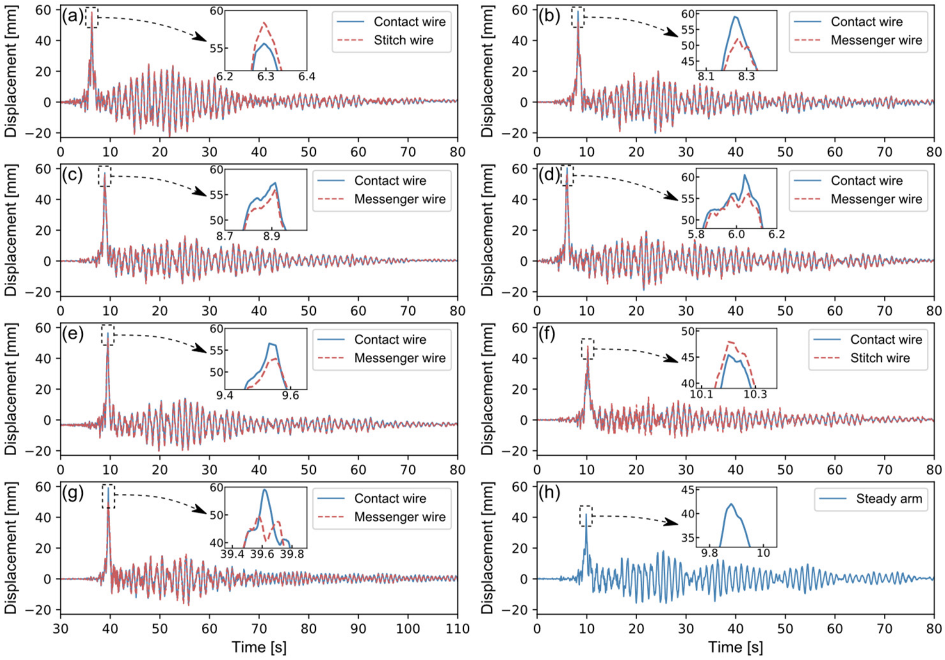

Fig. 3.13. Displacement comparison. (a)-(f) Droppers 1-6; (g) midspan point; (h) steady arm.

Table 3.5. Statistics of the maximum uplift for all passages.

		Mean (mm)	Standard deviation (mm)	Maximum (mm)	Minimum (mm)
Dropper 1	CW	51.28	4.95	58.15	44.51
	SW	52.45	5.61	58.81	43.81
Dropper 2	CW	54.20	4.65	59.05	46.34
	MW	47.80	2.49	52.00	43.60
Dropper 3	CW	52.32	7.11	62.63	41.20
	MW	50.58	6.74	59.73	39.84
Dropper 4	CW	55.83	9.69	70.36	47.76
	MW	52.73	8.10	64.22	45.68
Dropper 5	CW	52.51	6.16	63.28	42.78
	MW	48.56	4.27	54.88	41.66
Dropper 6	CW	44.12	4.77	54.28	39.22
	SW	47.31	4.51	57.26	42.08
Midspan point	CW	57.75	5.32	66.40	49.71
	MW	49.87	4.59	56.35	41.81
Steady arm	CW	47.62	4.41	53.90	41.12

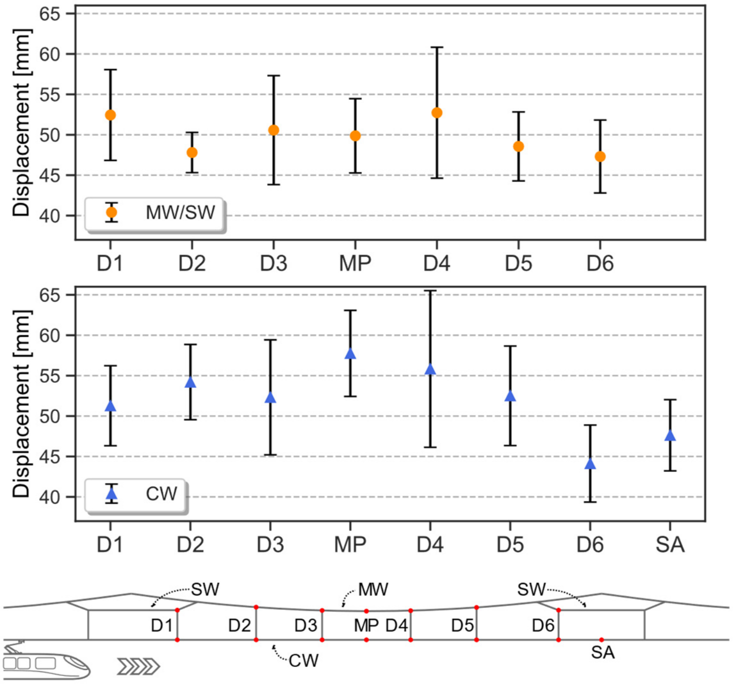

Fig. 3.14. Mean and standard deviation of the maximum displacement. MW-messenger wire, SW-stitch wire, CW-contact wire.

A minimum of five single-pantograph train passages was included for every measuring point to determine the mean, standard deviation, maximum and minimum values of the maximum uplift. All results at the investigated positions are listed in Table 3.5 and Fig. 3.14. The midpoints in Fig. 3.14 are the mean values, and the upper and lower caps indicate the standard deviations. CW and MW/SW are the contact wire and messenger wire/stitch wire, respectively. D1 - D6, MP and SA are droppers 1 – 6, midspan point and the steady arm, respectively. The displacement of the steady arm, used to determine the safety level, is relatively small compared to other measuring points on the contact wire. The midspan point and droppers 3 and 4 usually exhibit a relatively substantial uplift over the whole span, and dropper 6 attains the minimum uplift, as expected from the design of the system. Compared to droppers 1 and 6, a small but clear train direction dependency of the uplift is observed over the span.

3.5.2 Acceleration response

The acceleration was estimated from the displacement signal by using numerical differentiation, as shown in Fig. 3.15. Numerical differentiation necessarily suffers from the magnification of small errors (or noises) [119]. Therefore, high-frequency noises might be induced when converting the displacement signal to acceleration using numerical differentiation [118]. Smoothing and filtering are two methods for removing this error. In smoothing, the estimated error is removed by creating an approximating function that attempts to follow the critical trend of the data and replaces the observed values with the expected or "smoothed" values. In filtering, the critical trend is modelled as a high-amplitude and low-frequency component of the data, and the error or noise is removed by filtering out the low-amplitude and high-frequency components. Filters are widely used in engineering for signal processing [119]. The original sampling rate was 200 Hz, and a low-pass filter at 80% of the Nyquist frequency, i.e., 80 Hz, suggested in [24], was used to process the catenary acceleration data.

The pre-passage, passing, and post-passage stages are shown in the green, red and blue in Fig. 3.15, respectively. For the pre-passage stage, i.e., before the pantograph passage, the catenary wires are excited by the forward wave causing oscillations. The closer the pantograph runs to the measured span, the greater the oscillations are. The passing stage is the pantograph passing through the measured span from one steady arm to another. The acceleration reaches its maximum value first before the displacement reaches its maximum value. The displacement reaches the maximum when the pantograph passes the measuring point, and then it drops rapidly. The time for passing the span is approximately 0.88 s with the average train speed of 203.24 km/h and the span length 49.8 m.

The post-passage response is mainly caused by the excitation of the pantograph uplift, i.e., the short impulse, and following decaying response are dominated by the fundamental frequencies [25,95]. Once the pantograph leaves the measuring span, there will be no contact force on the catenary wire, and it will freely vibrate. The post-passage acceleration data were used for the later operational modal analysis.

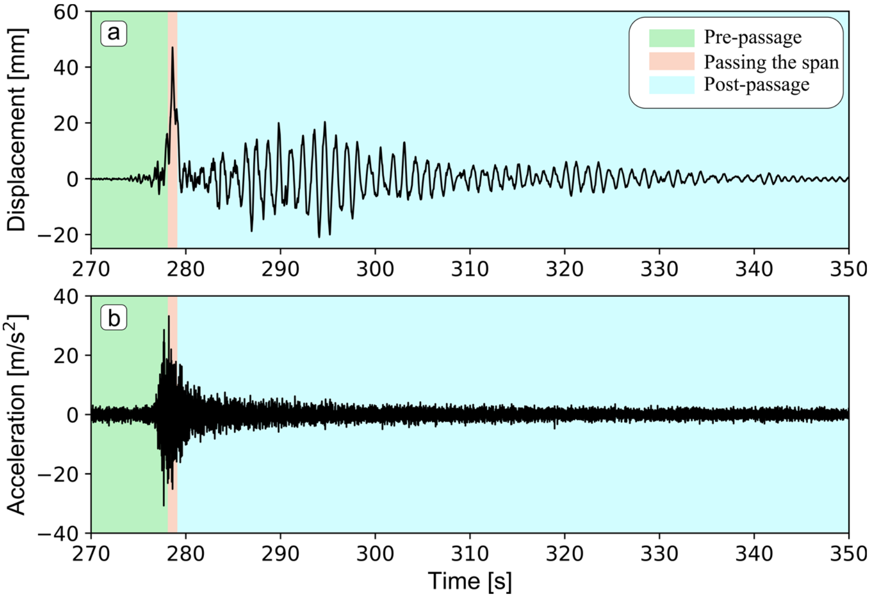

Fig. 3.15. A vibration-response example of a train passage at a measuring point. (a) Displacement; (b) corresponding acceleration.

3.5.3 Power spectral density (PSD) estimation

PSD estimation at all measuring points based on the obtained post-passage displacement data was performed. There are several PSD estimation methods, and Welch's average periodogram method [120] was chosen to estimate the PSDs of the catenary wires. Welch's method has been commonly used in the PSD estimation in railways [121-124], bridges [125-131] or other engineering fields. The time series of each component was divided into eight segments with a 50% overlap. The PSDs were then calculated for each segment using the fast Fourier transform (FFT) method and averaged after applying a Hamming window. The length of the applied window controls the trade-off between bias and variance of the resulting PSDs [132]. A good agreement between the PSDs of the contact, messenger and stitch wires was observed for droppers 1 – 6, as shown in Fig. 3.16 (a) – (f). This implies that the catenary wires have similar modal properties at the same dropper location. The largest difference between the PSD curves occurred at the midspan point, as shown in Fig. 3.16 (g), which is a part without a dropper.

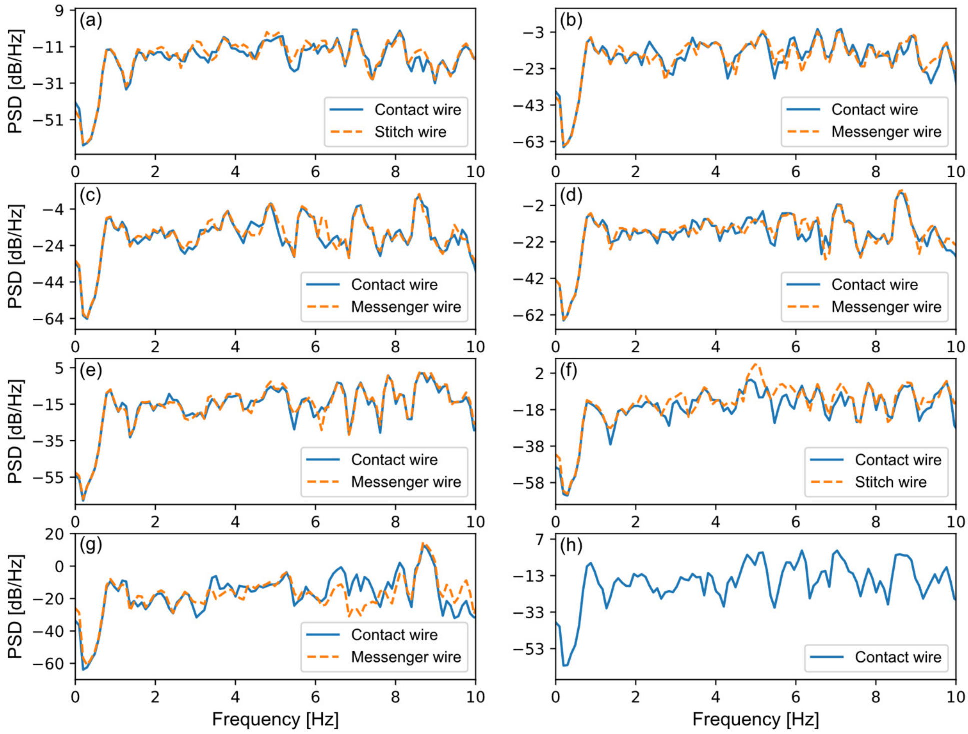

Fig. 3.16. Power spectral density of the response. (a)-(f) Droppers 1-6; (g) midspan point; (h) steady arm.

Table 3.6**.** Modal frequencies

Modal Frequency (Hz)	Dropper 1	Dropper 2	Dropper 3	Dropper 4	Dropper 5	Dropper 6	Midspan point	Steady arm
1st mode	0.84	0.84	0.83	0.83	0.83	0.83	0.85	0.82
2nd mode	/	1.21	1.21	1.23	1.21	/	1.22	/
3rd mode	1.53	1.51	1.50	1.54	1.56	1.52	1.55	1.50

The frequencies at the peaks of the PSD curves are the modal frequencies. Table 3.6 lists the 1st – 3rd modal frequencies obtained at droppers 1 – 6, midspan point and steady arm. It is observed that the 1st and 3rd modes occur at all measuring points, but the 2nd mode is not detected at droppers 1, 6 and the steady arm point, which occur along the segment with the dropper connected to the stitch wire instead of the messenger wire. To reveal this difference more clearly, the PSDs of the contact wire at all measuring locations from 0 to 10 Hz are compared and plotted in Fig. 3.17. The absence of the 2nd mode is clearly observed for droppers 1 and 6 and the steady arm point. The 2nd modal frequency reflects the related mode of the normal droppers, i.e., droppers 2-5. However, the elastic droppers, i.e., droppers 1 and 6, connected to the stitch wire, are insensitive to the 2nd mode.

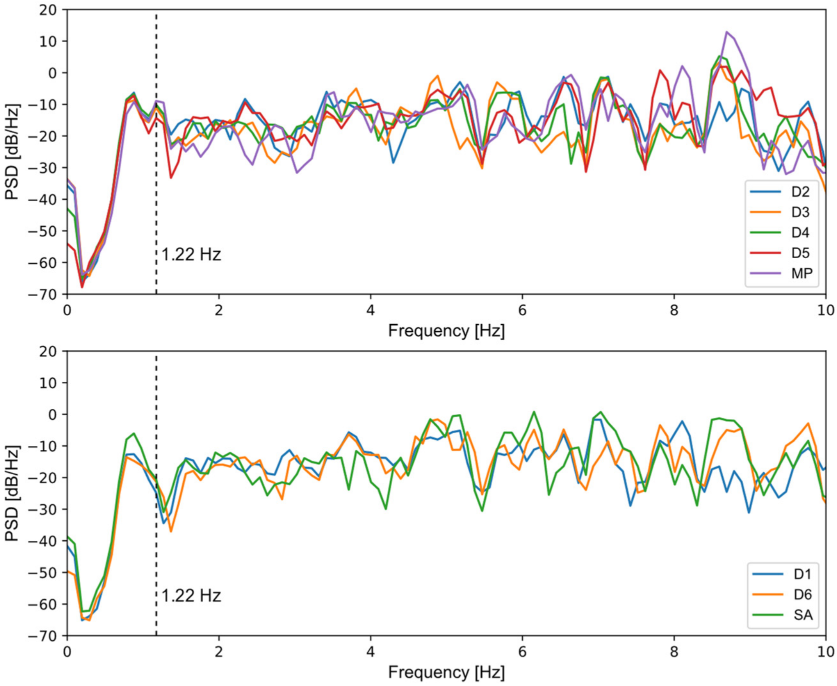

Fig. 3.17. Comparison of the power spectral densities.

3.6 Damping assessment

Damping is an important property in the simulation of pantograph-catenary dynamics, but it is equally challenging to estimate and simulate [12,22]. Damping describes the energy dissipation features of catenary oscillation, and the damping ratio reflects the speed of oscillation attenuation. To describe catenary damping, Rayleigh damping was selected, which is proportional to the linear combination of mass and stiffness. Rayleigh damping has been widely adopted to represent damping in pantograph-catenary interaction studies [16,24,33,98,133]. Classical Rayleigh damping is defined as:

$$[C]=\alpha[M]+\beta[K] \tag{3.5}$$

where $[\boldsymbol{C}]$ is the damping matrix of the object system; $[\boldsymbol{M}]$ and $[\boldsymbol{K}]$ are the mass and stiffness matrices, respectively, of the system; and α and β are the mass and stiffness damping coefficients, respectively, known as the Rayleigh damping coefficients.

For a system with multiple degrees of freedom, α and β can be estimated as:

$$\zeta_k = (\alpha / \omega_k + \beta \cdot \omega_k) / 2, \qquad k = 1, 2, ..., N \tag{3.6}$$

where ω_k is the natural frequency in rad/s; $\omega_k = 2\pi \cdot f_k$, f_k is the natural frequency in Hz; and ζ_k is the corresponding damping ratio. Based on Eq. (3.6), it is observed that the damping ratio ζ_k is proportional to the natural frequency ω_k.

The covariance-driven stochastic subspace identification (Cov-SSI) method [35] was adopted to determine the modal frequencies and damping ratios. KOMA, developed by Kvåle et al. [127,134], is a package suitable for operational modal analysis, including the Cov-SSI method, and has been employed in the article.

The Cov-SSI method uses post-passage acceleration data, i.e., after the passage of the pantograph, as output-only data to identify a stochastic state-space model for each measuring point. The damping ratio and corresponding frequency were extracted through the Cov-SSI method with stable poles up to 20 Hz. The stability diagram, consisting of the PSD and stable poles, is shown in Fig. 3.18. It is observed that the PSD and Cov-SSI methods attain a good agreement in terms of the modal frequencies, i.e., the peaks of the PSD curve. Closely spaced modal frequencies of the catenary wire [24,33] are also shown in Fig. 3.18.

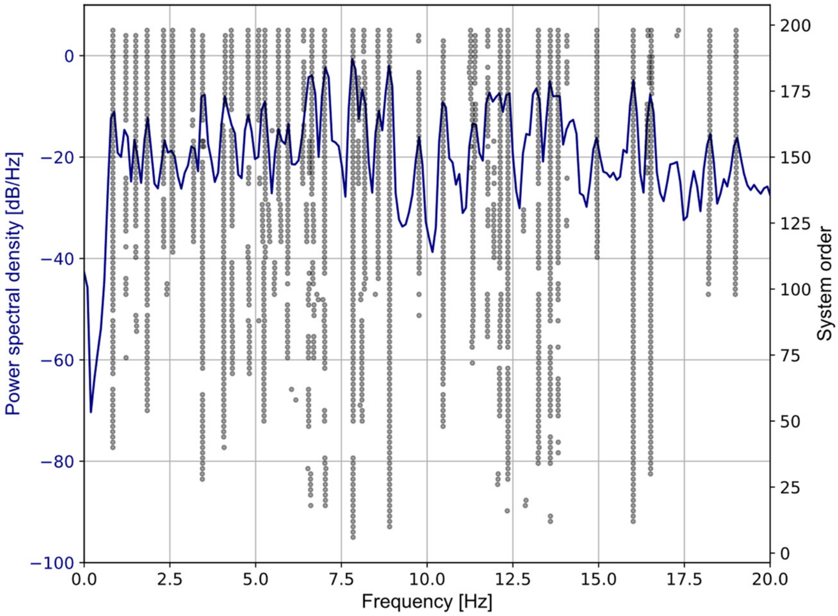

Fig. 3.18. Stability diagram constructed with the Cov-SSI method.

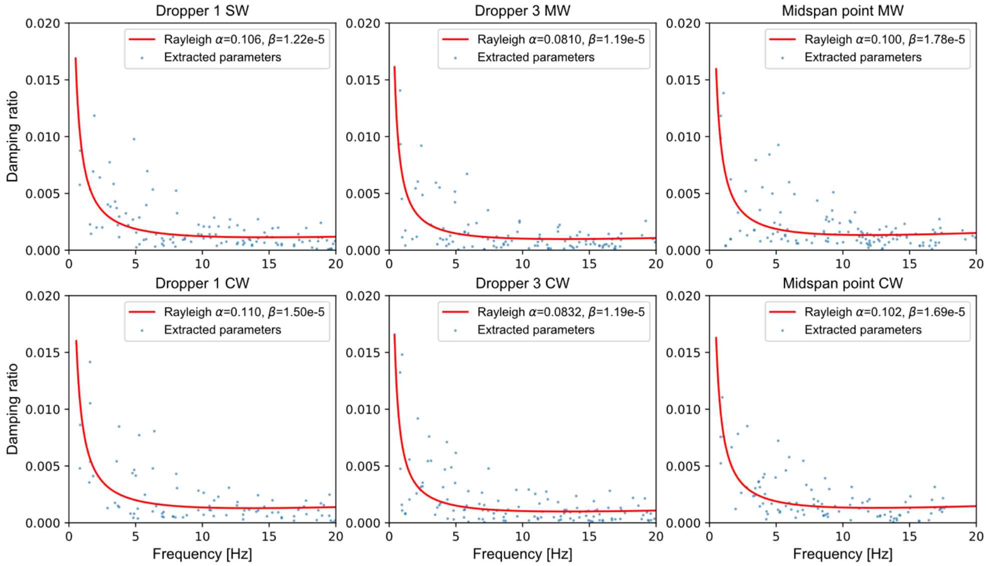

Fig. 3.19. Damping extraction and Rayleigh damping curve fitting from the measurements.

Different extracted parameters, i.e., the damping ratio and corresponding frequency, are applied to estimate the Rayleigh damping coefficients, as shown by the blue points in Fig. 3.19. For the sake of clarity, the frequency in rad/s is converted into Hz. Rayleigh curve fitting was performed to estimate the damping coefficients α and β. The estimated coefficients α and β, the corresponding Rayleigh curves and the extracted parameters are shown in Fig. 3.19 for droppers 1 and 3 and the midspan point. In all cases, the damping ratio is high at a low frequency, and it rapidly decreases with increasing frequency as expected. This trend indicates that the damping matrix $[\boldsymbol{C}]$ of the catenary wire is mainly determined by the mass-proportional part and only slightly influenced by the stiffness-proportional part. The estimated coefficients at all measuring locations are listed in Table 3.7.

Table 3.7**.** Rayleigh damping coefficients α and β at all measuring locations.

Measuring locations		α	β
Dropper 1	CW	0.110	1.50 E-5
	SW	0.106	1.22 E-5
Dropper 2	CW	0.0955	1.99 E-5
	MW	0.0929	1.40 E-5
Dropper 3	CW	0.0832	1.19 E-5
	MW	0.0810	1.19 E-5

Dropper 4	CW	0.0751	1.71 E-5
	MW	0.0718	1.74 E-5
Dropper 5	CW	0.0900	1.60 E-5
	MW	0.0848	1.59 E-5
Dropper 6	CW	0.102	9.59 E-6
	SW	0.102	1.20 E-5
Midspan	CW	0.102	1.69 E-5
	MW	0.100	1.78 E-5
Steady arm	CW	0.0841	1.70 E-5
Averaged over all locations	CW	0.0929	1.54 E-5
	MW/SW	0.0913	1.45 E-5

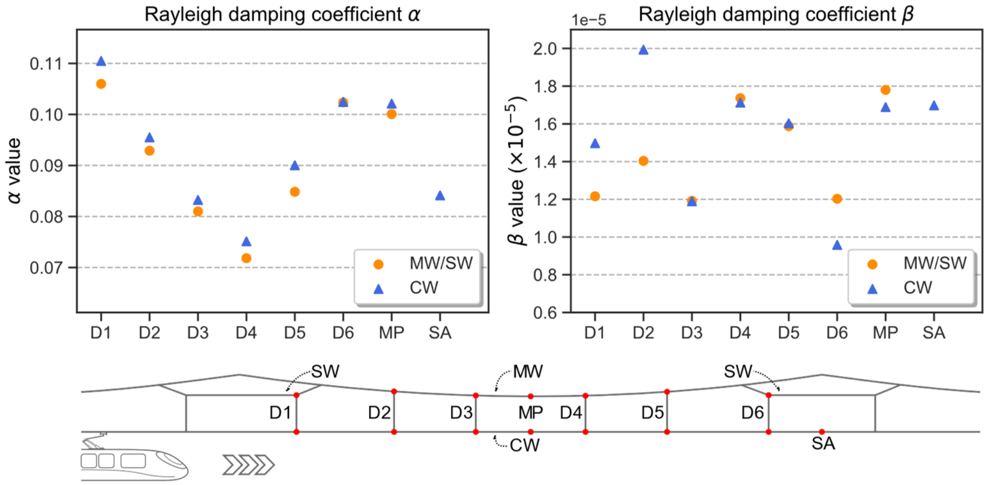

Fig. 3.20. Distribution of the Rayleigh damping coefficients α and β, where CW and MW/SW are the contact wire and messenger wire or stitch wire, respectively; D1 - D6, MP and SA are droppers 1 – 6, midspan point and steady arm, respectively.

Fig. 3.20 shows a comparison of coefficients α and β of the contact, messenger and stitch wires. The upper wires are the stitch wires for droppers 1 and 6, but in regard to the centre droppers 2 – 5, the upper wires are the messenger wires. Table 3.7 and Fig. 3.20 reveal that coefficient α of the contact wire is generally larger than that of the messenger or stitch wire. Coefficient β is roughly equal but randomly distributed across all droppers.

The α change trend, depending on the operation direction of the train, is observed. As shown in Fig. 3.20, α decreases from droppers 1 to 4 but increases from droppers 4 to 6. The middle dropper 4 attains the minimum α value. The train operation direction is from droppers 1 to 6. The coefficient α of droppers 1 - 3 are larger than those of their symmetrical droppers 4 - 6. However, these droppers and their symmetrical droppers have the same design parameters, i.e., the location, size and tension forces. It can be concluded that the mass damping coefficient α is influenced by the operation direction of the train. Compared to the α change trend, the β change trend is more random. Because the β value is small, it is sensitive to noise, i.e., it is easily influenced by noise.

Compared to the displacement amplitude in Fig. 3.14 and the α change trend in Fig. 3.20, it is observed that the displacement amplitude and damping coefficient α are correlated. Dropper 4 exhibits the largest displacement amplitude among the six droppers, but it attains the smallest damping coefficient α or the lowest damping ratio. The standard deviation of the amplitude of dropper 4 is also the largest among the six droppers.

As shown in Fig. 3.20, the midspan point is independent of droppers 3 and 4. The coefficients α of droppers 3 and 4 are the minimum across the whole span, but the α value at the midspan point is close to the maximum value. This phenomenon indicates that the dynamic behaviours of the parts without a dropper are different and amplitude-dependent, as these measuring points all occur in the midspan segment. The above phenomenon is also observed between dropper 6 and the steady arm point.

Based on the results of the Rayleigh damping coefficients α and β, the averages over all locations, as listed in Table 3.7, are recommended when a similar catenary system is simulated.

3.7 Conclusion

The present study aimed to investigate the damping and uplift of an existing railway catenary span under scheduled train operation. A vision-based line-tracking system (VIBLITE) was applied for remote, non-contact and non-marker uplift measurements. A simplified pinhole camera model for camera calibration purposes was described in detail. A detailed study was performed at critical locations along the span, including dropper clamps (on the contact, messenger and stitch wires), midspan point, and steady arm. Sixty-nine single/double-pantograph train passages were acquired during a three-day measurement. The results reveal that the contact, messenger and stitch wires are synchronous in terms of their vibration response over time. The uplift, for railways important, shows a small but clear train direction dependency over the span. Furthermore, all values are well within the maximum allowed uplift as expected.

The system damping was successfully estimated by the Cov-SSI method, and the distribution and change trend of the Rayleigh damping coefficients over one span were presented and analysed. The mass coefficients α are larger towards the poles than those towards the midspan. A small but clear train direction dependency of the damping distribution was also observed over the entire span. Thus, a fixed span damping ratio will include uncertainties from both spatial and directional variations. Therefore, this influence should be considered in future numerical simulations, depending on the problem investigated.

If the Rayleigh damping coefficients of similar catenary systems are unknown, it is recommended to use the averages of the mass and stiffness damping coefficients α and β determined in this study. That is, for the contact wire use, $\alpha = 0.0929$ and $\beta = 1.54$ E-5; for the messenger or stitch wire use, $\alpha = 0.0913$ and $\beta = 1.45$ E-5. For the current system, the damping ratios ζ_k from the recommended Rayleigh damping coefficients become 0.00884 and 0.00869 at the 1st-mode frequency of 0.84 Hz for the contact wire and messenger or stitch wire, respectively.

Chapter 4

Assessment of transition section contact point spatial variation via optical-based field measurements of railway catenaries

Tengjiao Jiang, Gunnstein T. Frøseth, Petter Nåvik and Anders Rønnquist,
Submitted for journal publication, 2021.

Abstract

Catenary section overlaps are designed to provide a transition zone between two consecutive catenary sections. The transition zone is several pole spans long, often three or five spans. Smooth pantograph-catenary contact is essential for regular train operation. However, under normal operation, these overlap spans are locations that are prone to the occurrence of peak contact force, which greatly affects the current collection quality. This work studies pantograph-catenary interaction and transition at overlap spans via measurements. An optical-based measuring method and a post-processing algorithm were developed and implemented under regular train operation to estimate the dynamic spatial vibration in contact wires. Image sequences of eleven single- and two double-pantograph train passages at a train speed of approximately 200 km/h were acquired. By analysing the motion path of the dynamic crossing point of the

two contact wires, this paper details the whole process of dynamic pantograph-catenary interaction and transition at overlap spans. The analyses reveal the reasons for the high contact forces and the contact loss rendering arcing. Finally, the important transition section distance, i.e., the length where the pantograph runs on both contact wires, was obtained and assessed at varying train speeds to study correlations. The transition section varied between 10 and 14 m at train speeds of approximately 200 km/h.

4.1 Introduction

Most high-speed trains in operation are powered by electricity because diesel locomotives are essentially unable to generate enough energy to reach high speeds [10]. Electricity is delivered through the pantograph-catenary system, composed of rigid pantographs and flexible catenary wires [99]. The pantograph mounted atop a train occurs in sliding contact with a contact wire to collect an electrical current [94,135]. The main structural components of the catenary system include contact and messenger wires, droppers and occasionally stitch wires. The messenger wire is suspended by cantilevers from poles at regular intervals. The main task of the messenger wire is to suspend the contact wire to the required design contact wire height from the track, achieved by droppers clamped onto the messenger and contact wires [13]. The contact wire follows a zigzag pattern to ensure that the sliding contact point moves over the panhead from side to side to distribute wear.

High speeds increase the dynamic response of the catenary system due to higher interaction forces. However, a smooth contact between the contact wires and pantograph is essential for regular train operation. A good pantograph-catenary contact improves the current collection quality, minimises contact loss and reduces wear. Contact loss is a major issue in pantograph-catenary interaction since it interrupts the power supply and increases wear. Overlapping sections are considered one of the most critical parts to ensure the current collection quality [1,136,137].

Each catenary section exhibits a limited length of approximately 1-1.5 km due to thermal expansion and tension decrease at each cantilever [16]. Tensioning devices consist of weights and pulleys to guarantee a constant mechanical tension in the catenaries. To ensure pantograph transit between consecutive sections, overlap spans are designed to raise the first section contact wire while lowering that of the second section to the nominal height. A three-span overlap section is shown in Fig. 4.1, where the contact wires exhibit a parabolic shape at the overlap spans. Conventional overlap sections also include four- and five-span sections [136]. The transition between two sections occurs in the middle of the central span for three- and five-span overlap sections. However, for a four-span overlap section, transition occurs at the pole, which is a hard point and thus may yield high contact forces. The simulation results in [138] reveal that a three-span overlap usually suffers higher contact forces than those of a five-span overlap with trains running at speeds between 100 and 160 km/h. Due to the more expensive construction of a five-span overlap, the three-span overlap is often chosen for low-speed lines. However, for high-speed lines, the five-span overlap is the preferred design geometry.

Pantographs transition between adjacent catenary sections within a transition section, i.e., the section between initial and end contact points. The initial contact point is a point where the pantograph starts to contact the second contact wire, and the end contact point is a point where the pantograph leaves the first contact wire. A static crossing point is the intersection of the two static contact wires on the vertical plane. The pantograph remains in contact with both wires for a certain distance until leaving the first contact wire, and this distance is referred to as the transition section distance, as shown in Fig. 4.2.

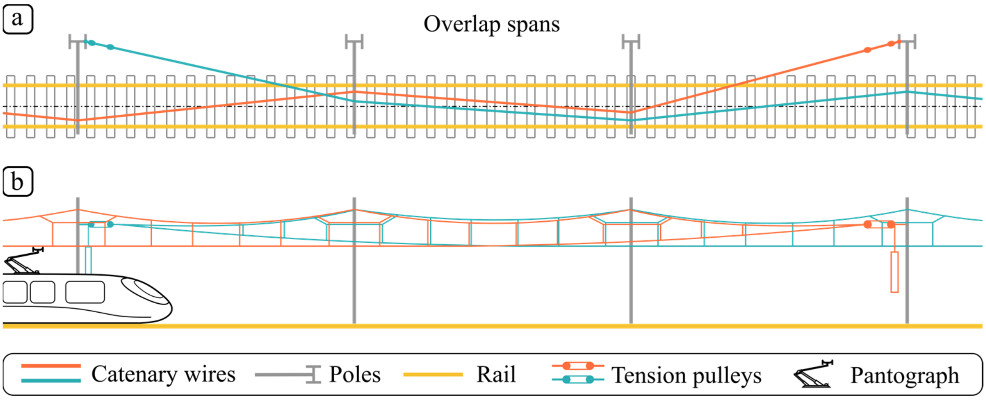

Fig. 4.1. Overlap spans of the catenary system. (a) Top view of the overlap section. (b) Horizontal view.

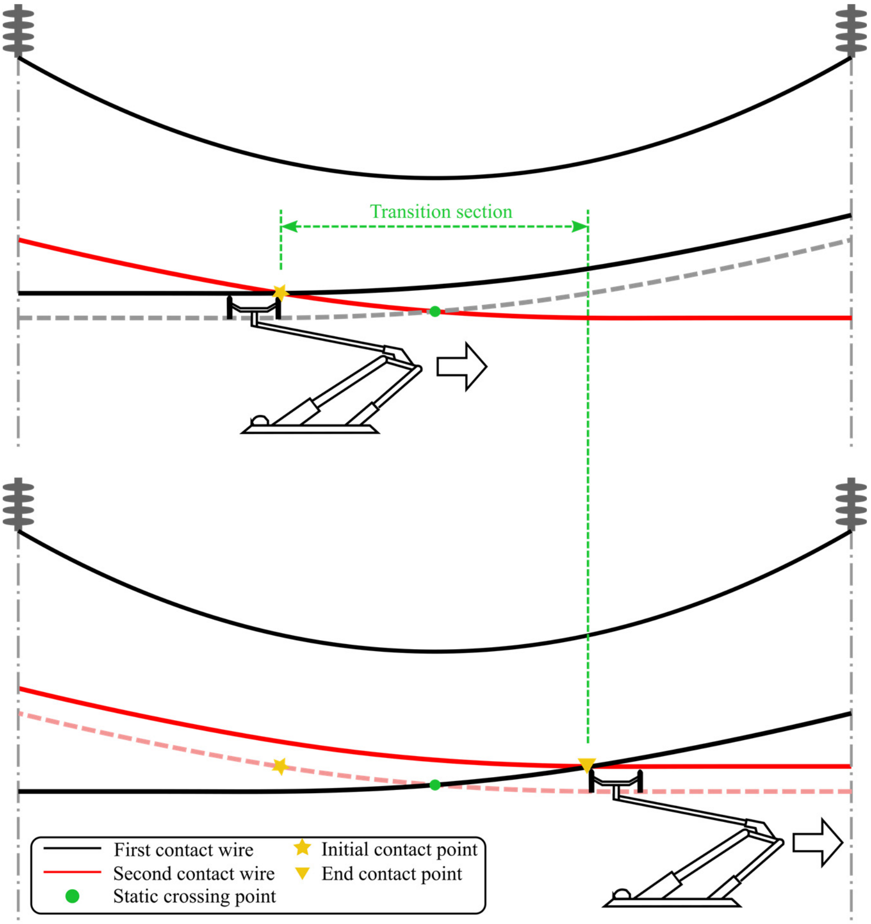

Fig. 4.2. Transition section within the overlap span.

Although a smooth contact is the design goal for the overlap span, the maximum contact force often occurs at the overlap span [136]. In particular, in regular traffic, a smooth transition in overlap spans is only partially achieved.

There are several studies of pantograph-catenary interaction in the literature, such as [10,16,18,139,140], which focus on dynamic behaviour in the conventional spans of the catenary section. However, there are only a few publications regarding the dynamic behaviour of overlap sections. Shimizu et al. [141] measured the contact wire height and wear to optimise the overlap section structure for high-speed Shinkansen lines. Harèll et al. [142] carried out simulations of a five-span overlap section under multiple-pantograph train operation. Their results indicated that the overlap section dynamic performance improved by lowering the lift at the support poles. Kuraoka et al. [143] studied various contact wire configurations in overlap sections with the aim of contact wire wear reduction. By comparing simulation results and inspection vehicle data, an improved contact wire height was found to reduce wear. Vesali et al. [137] designed novel control approaches for catenary systems to prevent pantograph wear and improve the contact quality at conventional spans and overlap sections. Gregori et al. [136] described a detailed simulation analysis of pantograph-catenary dynamic interaction in overlap sections under double-pantograph operation. A catenary section was optimised via the application of Bayesian optimisation techniques to reduce the contact force standard deviation, including the overlap section.

In the current study, no publications are identified on field experiments in regular traffic that successfully measured and mapped the dynamic behaviour of the crossing point of section overlaps. Thus, this work aims to study the dynamic pantograph-catenary interaction of an existing overlap span under scheduled train operations. Computer vision technologies have been implemented in many engineering, e.g., bridge engineering [36,118], mechanical engineering [111,117,144,145], railway engineering [39,146]. A vision-based line-tracking system (VIBLITE) [37] was adopted in this case. A novel overlap measuring method is presented and implemented to estimate the dynamic crossing point spatial motion of the contact wires. Image sequences of eleven single- and two double-pantograph train passages were acquired, including the train speed. The dynamic interaction and transition of the pantograph-catenary at the overlap span are introduced in detail. The dynamic effects rendering high contact forces and a high probability of contact loss and arcing at the overlap spans were investigated. The pantograph typically contacts the second contact wire at a certain distance before reaching the static crossing point. The rear pantograph causes a more severe dynamic interaction than that caused by the front pantograph in double-pantograph train passages. Finally, the transition section distance, i.e., the length where the pantograph runs on both contact wires at the overlap span, was determined and assessed at various train speeds to study correlations, which are basically positive in this investigation.

4.2 Vision-based line-tracking system, configuration and calibration

A vision-based line-tracking system (VIBLITE) [37] was adopted in the field measurements. In contrast to tests conducted on conventional spans [140], the crossing catenary wires at the overlap span yield new challenges in uplift measurement. Therefore, a new method for the measurement of the crossing contact wires was proposed and implemented.

The method first measures the height of the two contact wires, secondly obtains the dynamic uplift of the contact wires under train passage, and finally estimates the dynamic spatial intersection of the contact wires. An optical-based height measuring method is introduced in Section 4.2.2, and the general procedure of dynamic intersection estimation is introduced in detail in Section 4.4.3.

4.2.1 System configuration

The VIBLITE consists of two area scan cameras (Basler ACA2000-165 μm), two optical lenses with a fixed focal length (Edmund Optics 25 mm C-series), a trigger (National Instruments NI USB-6210), a solid-state drive (Samsung T7 Portable SSD 2TB), a laptop (DELL Latitude 7490) and a laser rangefinder (Leica DISTO™ D8), all shown in Fig. 4.5. The camera contains a complementary metal-oxide-semiconductor (CMOS) sensor with a 2048×1088-pixel resolution. The dynamic range of the CMOS sensor is 8 bits, and the intensity value of each pixel is within the interval of [0-255]. The sensor format is 2/3 inches, and the physical sensor size is 11.3×6 mm, and the physical pixel size is 5.5×5.5 μm. The camera is connected to the laptop via a USB 3.0 wire for image data transmission and power supply purposes. The focal length of the lens, i.e., 25 mm, is adopted in this case. The optical distortion of the lens is lower than 0.7%, and the aperture ranges from f/1.4 to f/16. The laser rangefinder measures the catenary-wire distance D_w and pitch angle θ, both essential calibration parameters for the measured height. The laptop controls the camera sampling rate and exposure time and transfers the obtained images from the camera to the external SSD.

4.2.2 Height measuring model

The measurement of wire motion at overlap spans is different from that at normal spans. Thus, a modified measuring method is developed for the section overlap where the contact wires cross. The camera setup location is usually lower than the contact wire height, which makes the estimation of the real crossing point of the contact wires via the tilt shooting more challenging. Thus, a novel method to estimate the spatial position of the crossing point by measuring the height of both contact wires is proposed, as shown in Fig. 4.3 (a).

A pinhole camera model is adopted to measure the height from the rail to the wire, as shown in Fig. 4.3 (b). The image plane is the surface of the digital image sensor. However, the resultant perspective projection of the object is inverted in the image plane. To simplify the subsequent geometric analysis, a virtual image plane is generated, which is located far from the optical centre O at focal length f. The camera pitch angle α, which always occurs after camera setup in field tests, is considered in the pinhole model to enhance the applicability.

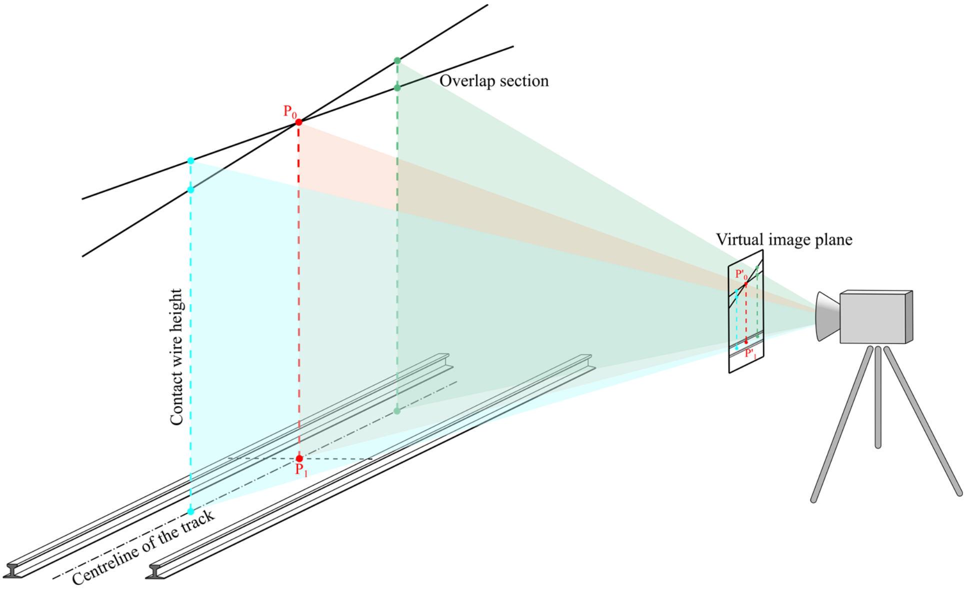

(a) Setup of the VIBLITE.

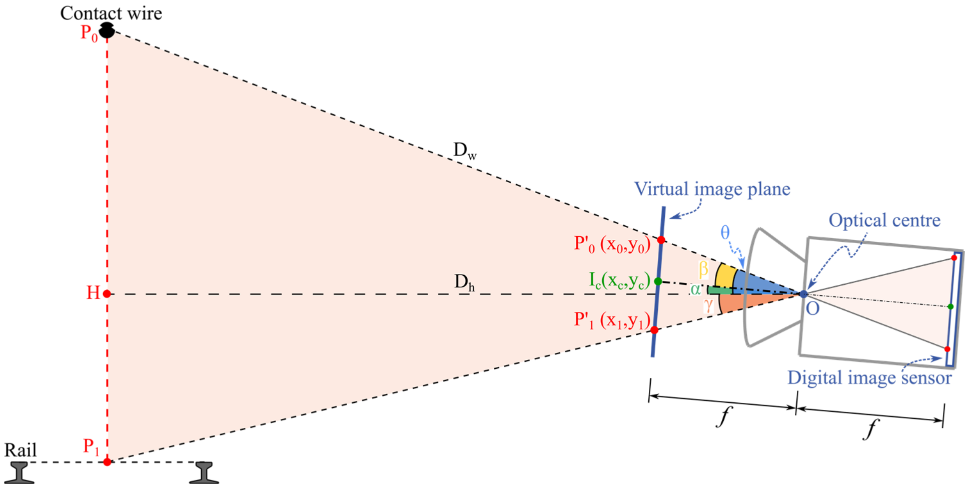

(b) Pinhole camera model for wire height measurement.

Fig. 4.3. Measuring method of the catenary wire height.

The measuring points, i.e., P_0 at the contact wires and P_1 at the rail, are projected as P'_0 and P'_1, respectively, in the image plane. The height P_0P_1 can be estimated as:

$$P_0P_1 = P_0H + P_1H = D_h \cdot \left[\tan\theta + \tan\gamma\right] = D_w \cdot \cos\theta \cdot \left[\tan\theta + \tan\gamma\right] \tag{4.1}$$

where D_w is the distance OP_0 between the contact wire and camera, and D_h is the horizontal projection OH of D_w. $\angle P_0OH$ is the pitch angle θ from the optical centre O to the contact wire P_0, and $\angle P_1OH$ is the pitch angle γ between the optical centre O and the rail. Because D_w and θ are measured in the field with the aid of a laser rangefinder, γ is the only unknown parameter to be estimated in Eq. (4.3) with the pinhole camera model, starting with:

$$\begin{aligned}
&\angle P_0^{'}OI_c = \beta = \arctan(\frac{P_0^{'}I_c}{OI_c}) = \arctan(\frac{\sqrt{[(x_0-x_c)^2+(y_0-y_c)^2]}\cdot S_c}{f}) \\
&\alpha = \theta-\beta = \theta-\arctan(\frac{\sqrt{[(x_0-x_c)^2+(y_0-y_c)^2]}\cdot S_c}{f}) \\
&\angle P_1^{'}OI_c = \alpha+\gamma = \arctan(\frac{P_1^{'}I_c}{OI_c}) = \arctan(\frac{\sqrt{[(x_1-x_c)^2+(y_1-y_c)^2]}\cdot S_c}{f})
\end{aligned} \tag{4.2}$$

where α is the pitch angle of the optical axis, and OI_c is the focal length f of the optical lens, which is 25 mm in this case. $\angle P_0^{'}OI_c$ is represented as β, and $P_0^{'}$ (x_0, y_0) and $P_1^{'}$ (x_1, y_1) are the image coordinates of the catenary wire and rail, respectively. I_c (x_c, y_c) is the centre point of the image plane, and S_c is the physical pixel size of the image sensor, which is 5.5 μm for the adopted camera (Basler ACA2000-165 μm). Hence, the pitch angle γ can be written as:

$$\begin{aligned}
\gamma &= \angle P_1^{'}OI_c-\alpha \\
&= \arctan(\frac{\sqrt{[(x_1-x_c)^2+(y_1-y_c)^2]}\cdot S_c}{f}) + \arctan(\frac{\sqrt{[(x_0-x_c)^2+(y_0-y_c)^2]}\cdot S_c}{f}) - \theta
\end{aligned} \tag{4.3}$$

After obtaining the pitch angle γ, the catenary wire height P_0P_1 can be estimated according to Eq. (4.1). In this case, the scale factor of the height estimation depends on various parameters, including the catenary-wire distance D_w, pitch angle θ, image coordinates (x_0, y_0), (x_1, y_1) and (x_c, y_c), focal length f of the optical lens, and physical pixel size S_c of the image sensor.

Through this height estimation method, two parameters must be measured in the field tests, i.e., the catenary-wire distance D_w and pitch angle θ. The distance D_w can be measured from 0.05 to 200 m with the Leica DISTO™ D8 laser rangefinder, and the measurement accuracy, which varies between 10 and 30 m, can be controlled within 0.1 mm. Moreover, the measurement accuracy of the pitch angle θ is controlled within 0.1°. Hence, the effect of any measurement errors in these two parameters on the measurement accuracy is small enough to be neglected.

4.2.3 Camera configurations

The exposure mode and shutter type are two essential features in camera selection. Before the adoption of multiple cameras, camera synchronisation should be considered to synchronise the camera exposure. In the current setup, a hardware trigger (National Instruments NI USB-6210) was applied to send a logic voltage signal to synchronise the cameras. Logic gate circuits are designed to input and output only two signal types, i.e., high (logic 1) and low (logic 0) signals, as representing a high and low voltage, respectively.

The timed and trigger width modes are two different exposure modes (Fig. 4.4). Under the timed exposure mode, exposure is initiated when a high-voltage signal is detected and is maintained until the exposure time has expired. However, under the trigger width exposure mode, the exposure time is defined by the width of the high-voltage signal. This indicates that exposure is also initiated when a high-voltage signal is detected, which is only maintained until the signal falls [116]. The timed mode was employed in this case due to its advantage of controlling the exposure of each camera individually.

The shutter type is an important feature of a digital image sensor. Global and rolling shutters are two main electronic shutter types. These two shutter types entail different exposure processes and final image results, especially in regard to fast-moving objects [116].

Regarding the global shutter, the exposure of all pixels starts and ends at the same time, but readout occurs row by row. Global shutter provides non-distorted images without wobbles or skewing and is suitable for fast-moving objects, e.g., high-speed trains and vibrating catenary wires. Regarding the rolling shutter, however, exposure occurs row by row at shifted times. Thus, the rolling shutter produces image distortion for fast-moving objects.

The adopted camera (Basler ACA2000-165 µm) contains a global shutter sensor, which is suitable for the measurement of the intense vibration of the catenary wires.

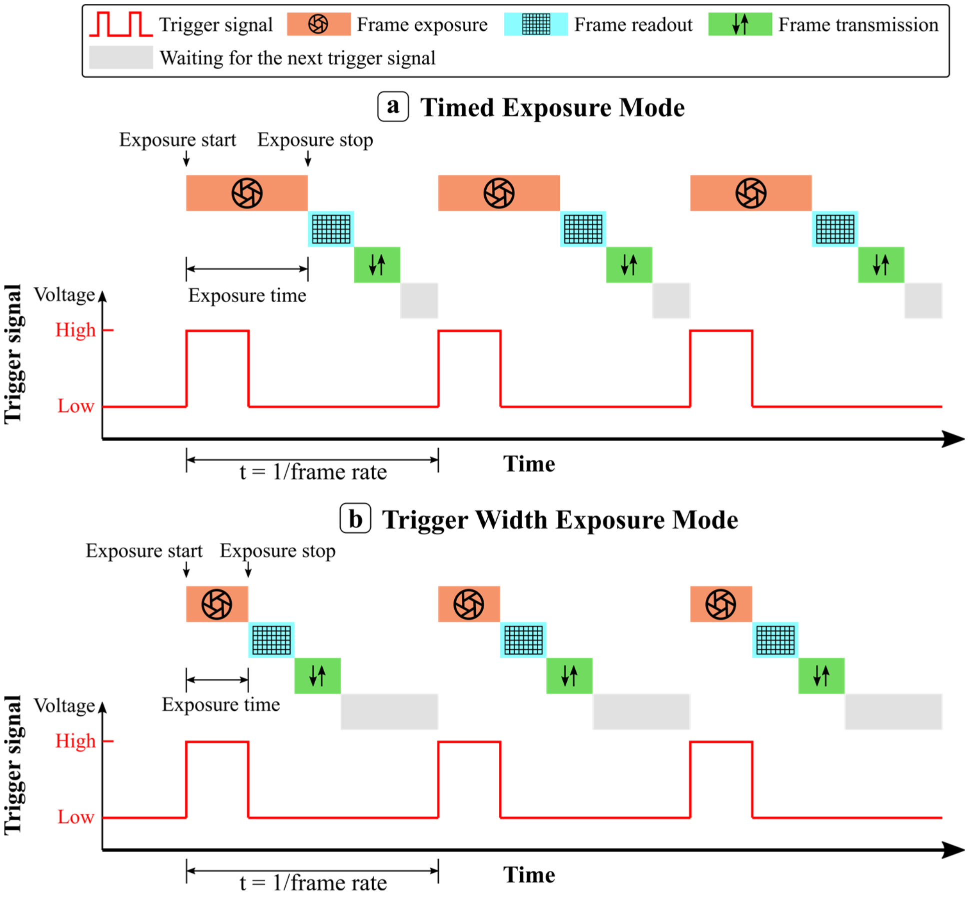

Fig. 4.4. Camera exposure modes.

4.3 Measurement arrangement of the overlap span in traffic

4.3.1 Measurement setup

The railway catenary system is a cable system, which is responsible for the uninterrupted supply of electricity to power trains. In this case, the main objective is to study pantograph-catenary interaction at the overlap span.

Different catenary systems are implemented in Norway, ranging from outdated systems as Tabell 54, to newer systems, from System 35 (130 km/h) to Systems 20 and 25 (200 km/h and 250 km/h, respectively) [15]. The current field measurements were conducted in section overlap spans along the Oslo airport line between Oslo Airport (OSL) and Oslo central station, i.e., System 25. This catenary system is a new system built and designed to accommodate trains operating at a maximum speed of 250 km/h.

Two types of high-speed trains, i.e., Stadler FLIRT Class 74 and GMB Class 71 trains, run along the airport line at train speeds of 200 and 210 km/h, respectively, as shown in Fig. 4.5.

The five-span section overlap is the standard design geometry of the Oslo airport line. The transition occurs at the midspan of the central span of the five-span section, where the pantograph contacts both contact wires. Thus, the uplift measurement was performed at the midspan of the central overlap span, as shown in Fig. 4.6. Both catenary sections contain 21 spans, and the length of the measured overlap span is 49 m.

Fig. 4.5. Oslo airport line. Photography: Tengjiao Jiang/NTNU. Maps courtesy of Kartverket©. Photos of the FLIRT train type courtesy of Norske tog© and the GMB train type courtesy of Flytoget©.

The VIBLITE was positioned outside the railway safety fence without any the scheduled train operation interference. Two cameras were applied in the field measurement to increase the shooting area, indicated by the blue and orange regions in Fig. 4.6. A hardware trigger synchronised these two cameras at a sampling frequency of 200 Hz.

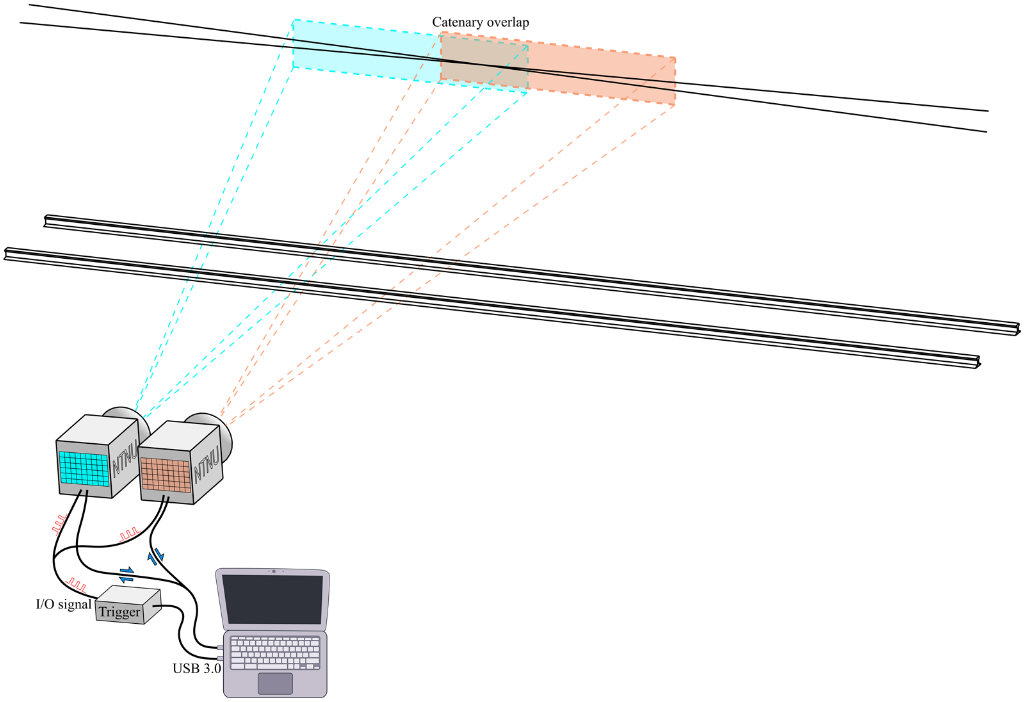

Fig. 4.6. Measurement schematic.

The exposure time of the cameras was limited by the sampling frequency and the time for the transferral of the obtained images to the laptop, e.g., less than 5 ms at the 200-Hz sampling frequency. Due to the limitation of the USB cable transfer speed at 200 Hz, each frame was cropped, and the pixel resolution was reduced to 2048×400 pixels.

Image sequences of the contact wires were measured up to 300 s (60000 frames) for each train passage. The image sequence started before train arrival at the measured span and ended when catenary wire vibration ceased. With the VIBLITE, 11 single- and 2 double-pantograph train passages were recorded in total.

4.3.2 Train-speed measuring method

Fig. 4.7. Measuring method of train speeds. Photography: Tengjiao Jiang/NTNU.

A Stalker LIDAR XLR instrument was applied to measure the train speed, as shown in Fig. 4.7. This instrument is a small and light hand-held gun-type LiDAR and achieves a good measuring range, high accuracy, and short acquisition time. It measures targets up to 1200 m away, and speeds ranging from 2-481 km/h can be measured at an accuracy of ±1 km/h. Thus, the train speeds of both Classes 71 and 74 (210 and 200 km/h) are well within the measuring range, and the train speed was included as a variable in the following data analysis.

4.3.3 Displacement acquisition via post image processing

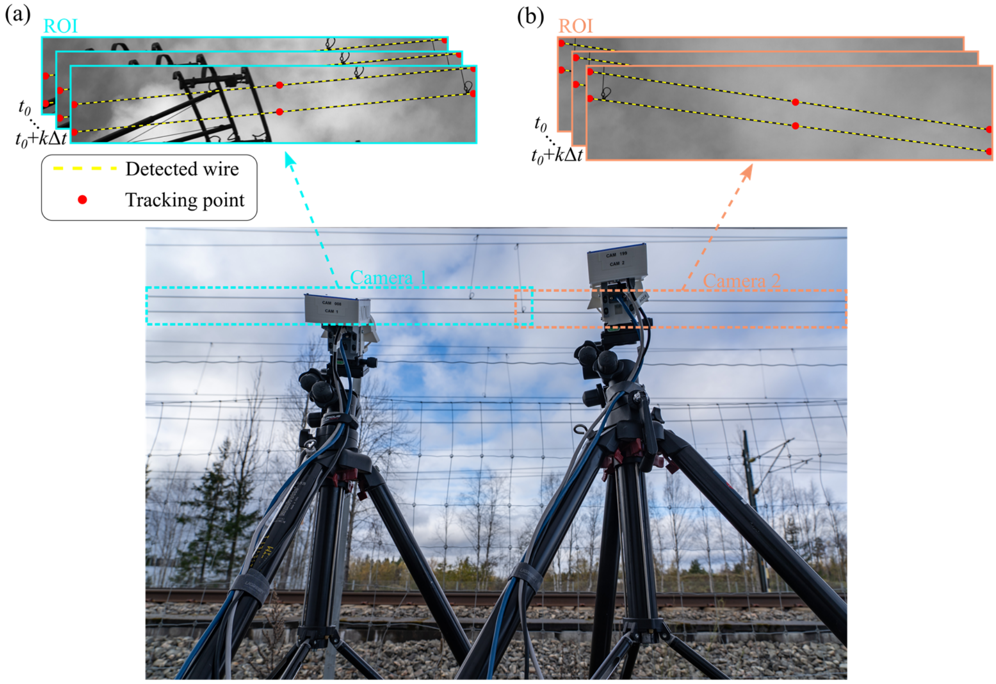

Fig. 4.8. Line-tracking image processing. The detected contact wires and tracking points of camera 1 (a) and camera 2 (b).

This section primarily focuses on the post-processing of the recorded image sequences for each train passage to obtain uplift data of the contact wires. The image sequences were processed with line-tracking technology, and the detection results are shown in Fig. 4.8. The yellow dashed lines indicate the detected catenary wires, and the red points indicate the tracking points.

For completeness, the line-tracking technique is briefly introduced. More detailed descriptions have been provided in a previous study [37], and the open-source code has been made available in [115]. In general, trees often occur along railways, yielding a non-uniform or noisy background of the catenary wire, which makes wire identification and tracking challenging. The line-tracking technique was developed to address the essential challenge of tracking slender wires without markers against noisy backgrounds. The accuracy and robustness of the line-tracking technique has been verified in [37]. The main idea of the line-tracking technique is to employ a sliding subset to search candidate parts of catenary wires along user-selected columns by comparing pixel intensity values. Subpixel centreline detection or subpixel edge detection is then performed to accurately calculate the centreline or edge through bicubic interpolation.

In this case, each image was defined with three searching columns encompassing three tracking points of each contact wire. The shooting areas of the two cameras contained a common area. Thus, after ignoring any repeated tracking points in the common shooting area, there were five independent tracking points for each contact wire. The yellow dashed lines are the detected centrelines between the adjacent tracking points.

At every tracking point, the wire displacement response in pixels before and after train passage was obtained. Then, the pixel displacement was converted into physical units (millimetres) through a pinhole camera calibration model in a previous study [140]. The scale factor for the conversion from pixel units into physical units depends on various parameters. These include the image coordinates of the tracking points and centre point of the image plane, the physical pixel size, the camera pitch angle, the focal length f of the optical lens, and the distance from the optical centre to the object, as described in detail in [140]. Except for the contact-wire distance D_w and pitch angle θ measured in the field, the other parameters are related to the adopted camera and optical lens. The hardware trigger synchronised the two adopted cameras to facilitate camera image sequence correspondence, which ensured the time synchronisation of the displacement data at a time interval of 0.005 s.

4.4 Vibration response and dynamic crossing point assessment

The excitation due to pantograph uplift mainly causes a dynamic response of the contact wires, i.e., the short impulse and the subsequent decaying response are dominated by their fundamental frequencies [25]. Excessive vibration of the catenary system causes contact loss and interrupts the train power supply [60]. Thus, it is essential to capture the spatial motion and study the dynamic response of the contact wires to control the maximum uplift and wear.

4.4.1 Uplift response under single-pantograph train passage

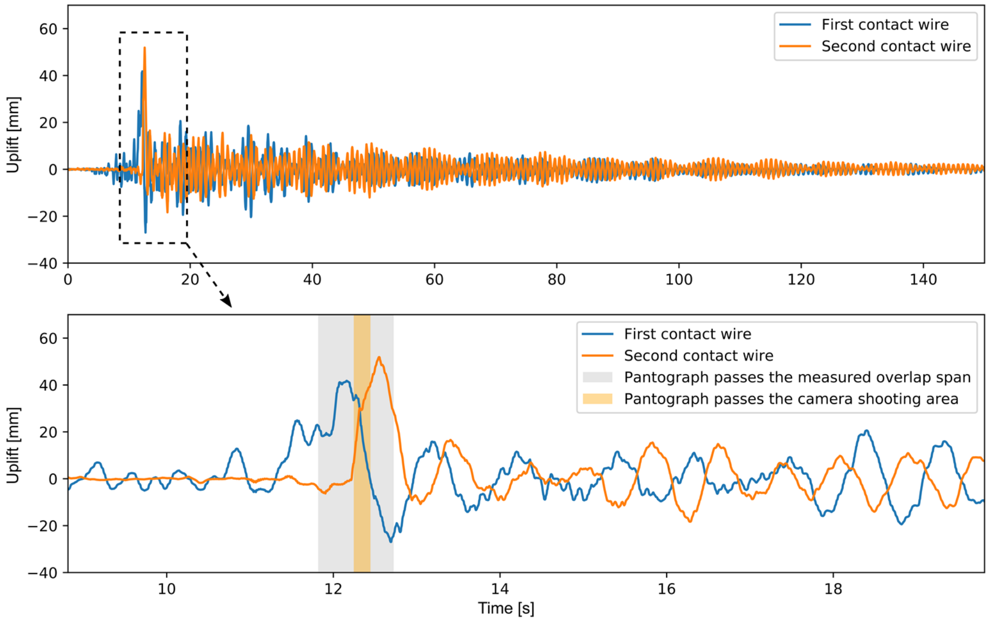

Fig. 4.9. Uplift of the first and second contact wires under single-pantograph train passage.

The uplift time series of the first and second contact wires at the static crossing point is shown in Fig. 4.9 under single-pantograph train passage. The grey and orange regions indicate the times when the pantograph passes the measured overlap span and camera shooting area, respectively.

The first contact wire reaches its maximum uplift value before the pantograph arrives at the static crossing location. However, the second contact wire reaches its maximum uplift value after the pantograph passed the static crossing location. This phenomenon reveals that the first wire starts to descend, and the second wire is uplifted when the pantograph passes the overlap span, as expected from the design of the system.

The maximum uplift of the second contact wire is larger than that of the first contact wire. It should also be noted that the first trough of the first contact wire, after the maximum uplift, is much lower than that of the second wire.

After the pantograph passes the measured overlap span, the first wire exhibits free vibration, and the amplitude decays. It is further analysed below to determine the distance before the static crossing location where a single pantograph interacts with the second wire.

4.4.2 Uplift response under double-pantograph train passage

Fig. 4.10 shows the uplift response under double-pantograph passage, which is compared to that under single-pantograph passage. Naturally, the first uplift peaks of the first and second contact wires are caused by the front pantograph, and the second peaks are caused by the rear pantograph. Similar to single-pantograph passage, the maximum uplift of the second contact wire is larger than that of the first contact wire, for both the front and rear pantographs.

Passage of the front pantograph causes a large vibration in the contact wires, which could affect the contact quality of the rear pantograph. The maximum uplift when the rear pantograph passes is larger than that when the front pantograph passes. The front and rear pantographs both interact with the second wire before reaching the static crossing point, which is further studied below.

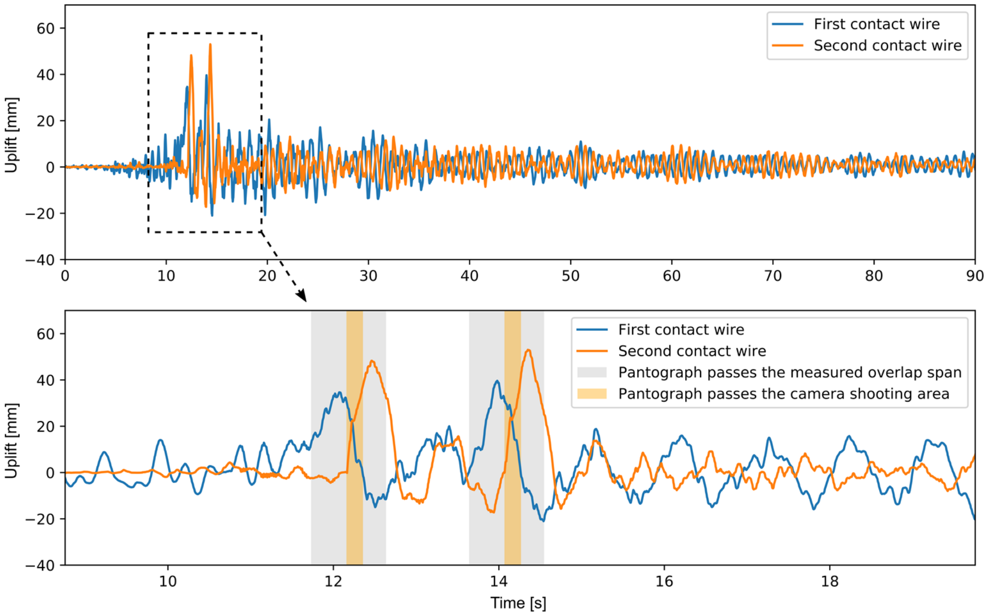

Fig. 4.10. Uplift of the contact wires under double-pantograph train passage.

4.4.3 Contact wire configuration and dynamic crossing point

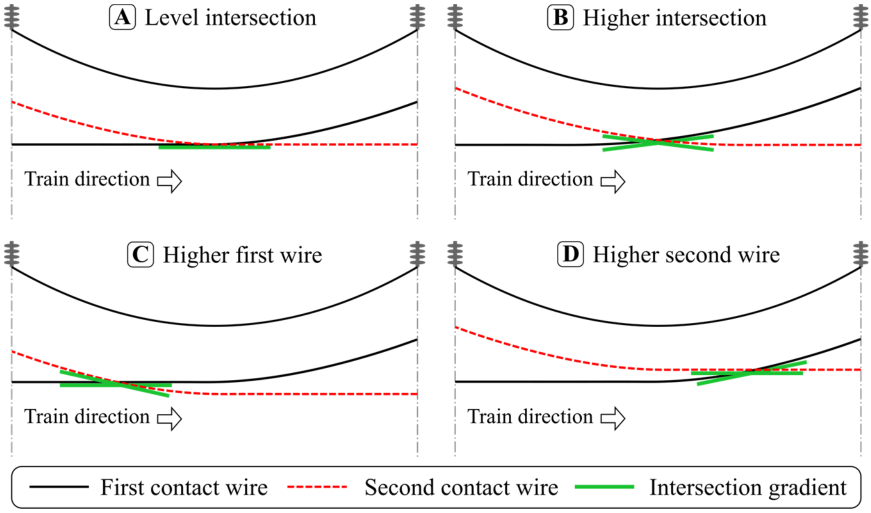

Fig. 4.11. Intersection configuration types of the contact wires in the overlap sections.

The design goal of the overlap section is to ensure that a given pantograph smoothly contacts and transits between adjacent sections. The intersection configuration of the contact wires has been classified into four types in the literature [141,143], as shown in Fig. 4.11. Type A is a level intersection where the intersection gradient is level with the contact wire, and type B is a higher intersection, i.e., the crossing point is higher than the contact wire height. Type C is the higher first wire type, i.e., the height of the first contact wire is higher than that of the second wire, and the opposite applies to type D.

In construction, the static crossing point is either raised or lowered as part of the design geometry. To reduce the transition section distance when the pantograph contacts both contact wires under type A, the crossing point is elevated 40 to 60 mm above the contact wire height, rendering the type B design geometry.

The literature [143] has indicated that wire wear under types B and C exceeds that under types A and D. In Norway, most railways are two-direction tracks, i.e., trains run along with both directions on a single track, and only a few railway tracks in Oslo are one-directional. Catenary type D is only suitable for one-direction tracks and not for two-direction tracks. Moreover, two-directional running results in more wear under type D, similar to type C. Due to the shortcomings of the long transition section distance of type A, type B has become the conventional design geometry for two-direction railway tracks in Norway.

The spatial motion path of the dynamic crossing point was analysed to study the dynamic interaction between the pantograph and contact wires at the section overlap.

The dynamic crossing point is the intersection of the two contact wires during vibration, which was measured with the VIBLITE as follows:

1) Measure the static height of ten contact wire tracking points from the rail, as described in Section 4.2.2.
2) Estimate the uplift response of the tracking points, as mentioned in Section 4.3.3.
3) Calculate the dynamic height of the tracking points during vibration by adding the static height and uplift response.
4) Create lines between each tracking point on the same wire to fit the shape of the real contact wire.
5) Estimate the dynamic crossing point by calculating the line intersection at each moment. The spatial location and corresponding time of the dynamic crossing point can be thusly obtained.
6) Determine the motion path of the crossing point as a time series.

The general procedure is shown in Fig. 4.12.

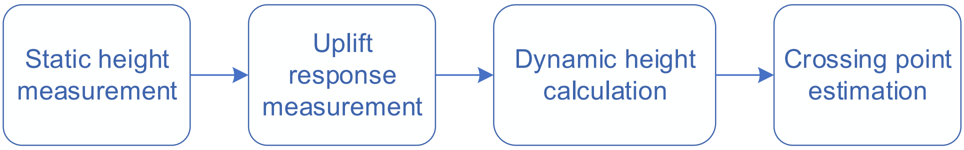

Fig. 4.12. General procedure of dynamic crossing-point estimation.

4.4.4 Dynamic crossing point under single-pantograph train passage

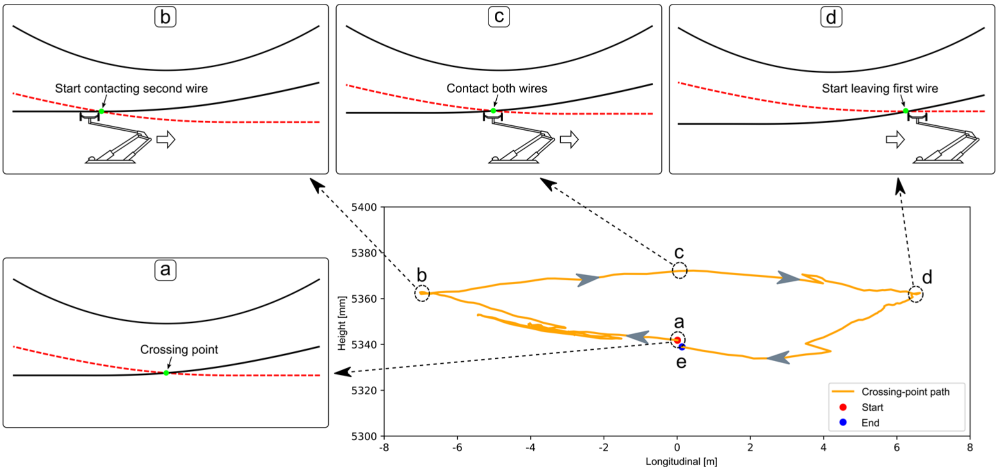

Fig. 4.13. Motion path of the dynamic crossing point and its corresponding sketch under pantograph passage.

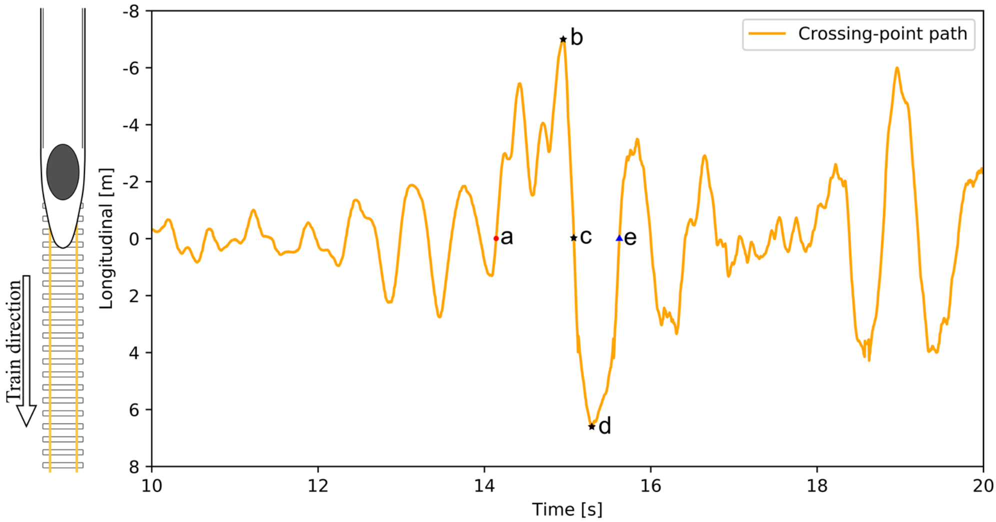

Fig. 4.14. Motion path of the dynamic crossing point as a time series viewed from above.

Under single-pantograph train passage, the spatial path of the crossing point is visualised to reveal the pantograph-catenary interaction at the overlap section in detail. One section of the motion path and the corresponding sketch during pantograph passage are shown in Fig. 4.13. The x-axis is the longitudinal distance from the camera setup location along the rail. The y-axis is the height from the rail along the vertical direction. Fig. 4.14 shows the motion path of the dynamic crossing point as a time series viewed from above. The y-axis is the longitudinal distance, and the train running direction is from top to bottom. The whole motion path can be interpreted as follows:

1) The red point, a, i.e., the starting point, indicates when the pantograph reaches the previous span before the measured span.
2) As the pantograph approaches, the first contact wire starts to vibrate, and the uplift increases. This moves the crossing point towards the train.
3) When the pantograph starts to contact the second wire, the crossing point now occurs at point b (the initial contact point).
4) The pantograph then comes into contact with both wires within the transition section, and the crossing point follows the pantograph motion to point c at the midspan.
5) The pantograph remains in contact with both wires until point d, when the first wire descends and the second wire is lifted. Point d is the moment when the pantograph loses contact with the first wire, i.e., the end contact point.

6) Thereafter, the pantograph successfully transitions to the consecutive catenary section. Without the pantograph contact force, the vibration in the first wire decays, and the crossing point moves to point e.

The pantograph starts to contact the second wire at the initial contact point b, where the intersection gradient is high. This produces a large impulse instead of a smooth contact between the pantograph and second wire. This contact situation is similar to type C in Fig. 4.11, and type C results in high wear of the contact wires. Gregori et al. [136] found through numerical simulations that the peak force occurs when the pantograph starts interacting with the second wire some metres before reaching the static crossing point. Thus, this could be the reason why the maximum contact force appears at the overlap span. The impulse generally increases contact wire wear and may induce contact loss and arcing. Arcing was recorded by the camera at a distance of 6.72 m before the static crossing point during the measurement, as shown in Fig. 4.15, which supports the above statement.

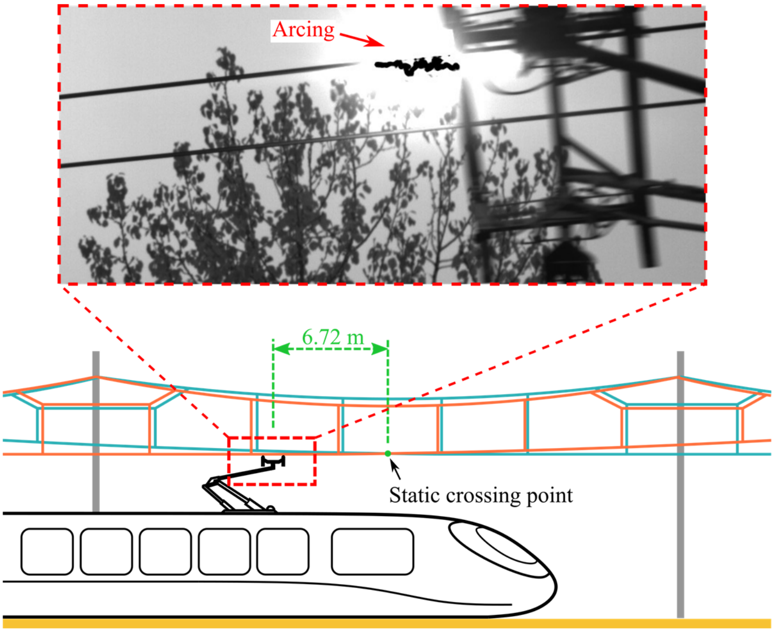

Fig. 4.15. Arcing at the overlap span during the measurement.

4.4.5 Dynamic crossing point under double-pantograph train passage

To determine why the rear pantograph attains a higher probability of contact loss and arcing in overlap spans, the motion path of the dynamic crossing point was studied under the double-pantograph passages.

Two sections of the motion path of the dynamic crossing during the front and rear pantographs passing are shown in Fig. 4.16, represented as a solid orange line and a dashed blue line, respectively. Fig. 4.17 shows the motion path of the dynamic crossing point from the above view as a time series.

The two motion paths start from points a_1 and a_2, which are close to the static crossing point location. These dynamic crossing points move to the initial contact points b_1 and b_2, respectively, while both pantographs start interacting with the second contact wire. However, for the rear pantograph, point b_2 moves more along the longitudinal direction towards the span pole than does point b_1, representing the front pantograph. This may cause a higher intersection gradient of the contact wires for the rear pantograph, as shown in Fig. 4.18.

The front and rear pantographs stay in contact with both wires, similar to the single pantograph. The crossing points b_1 and b_2 follow the pantograph movement to points c_1 and c_2, respectively. The uplift of the rear pantograph is larger than that of the front pantograph. Fig. 4.10 also shows that the maximum uplift of the rear pantograph passage is greater than that of the front pantograph passage.

The front and rear pantographs stay in contact with both wires until they reach the points d_1 and d_2, respectively. Points d_1 and d_2 are close in height and longitudinal location, in contrast to points b_1 and b_2, which greatly differ along the longitudinal direction. Points d_1 and d_2 are the moments when the pantographs lose contact with the first wire, i.e., the end contact points. Finally, the crossing points move to e_1 and e_2, respectively.

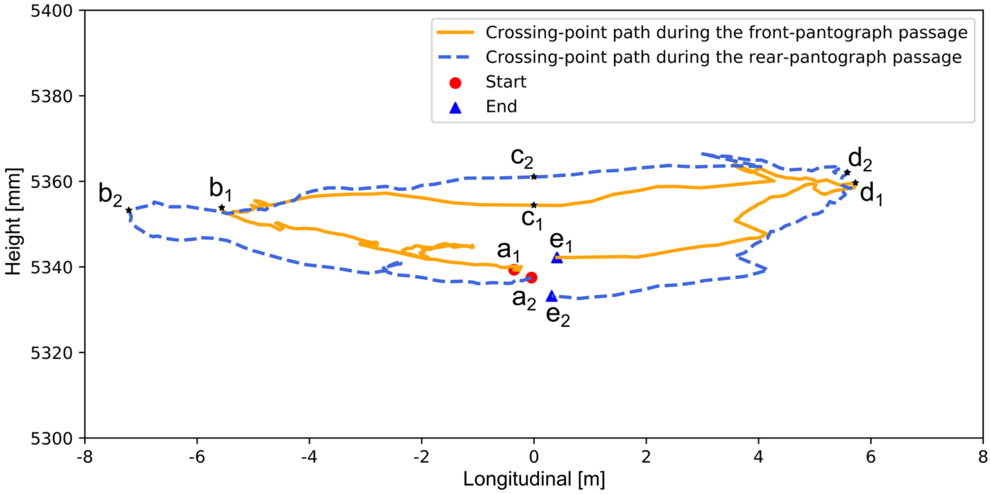

Fig. 4.16. Motion path comparison of the crossing point when the first and second pantographs pass.

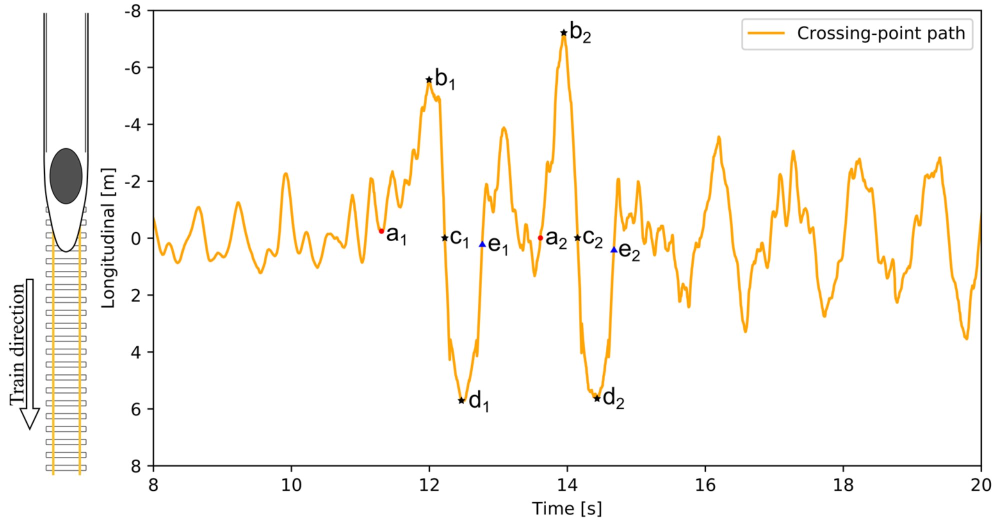

Fig. 4.17. Motion path of the dynamic crossing point as a time series viewed from above.

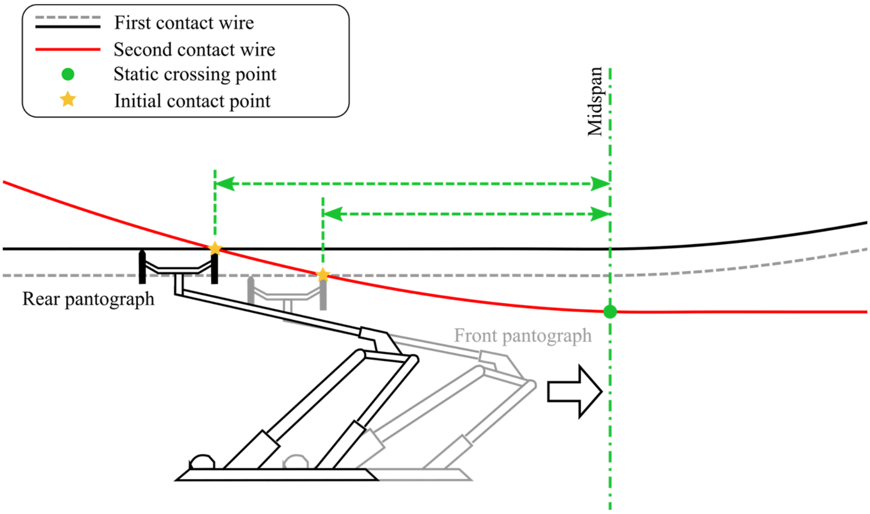

Fig. 4.18. Greater longitudinal distance and intersection gradient for the rear pantograph.

In summary, the rear pantograph achieves a greater longitudinal distance and intersection gradient (point b_2) and a higher uplift (point c_2) than those of the front pantograph. This occurs because the rear pantograph enters the catenary system that is already in motion due to the front pantograph, resulting in a higher dynamic response. Thus, the rear pantograph could experience a more severe impulse and a higher risk of contact loss and arcing within the overlap span than those experienced by the front pantograph. The more severe impulse could induce the rear pantograph to attain a higher peak force. This verifies and demonstrates the similar findings of the higher contact force produced by the rear pantograph in numerical simulations [136,142].

4.4.6 Train speed effect on the transition section distance

This section aims to determine the train speed effect on the transition section distance within the overlap span. A higher train speed imposes a negative effect on the contact quality of pantograph-catenary interaction [147,148].

The transition section distance should be limited due to the power supply switch of catenary sections. The transition section distance was estimated as 13.4 m via a numerical simulation of a single pantograph operating at 300 km/h in the literature [136]. No field measurement has been found in the literature of the transition section distance in existing overlap sections during operation.

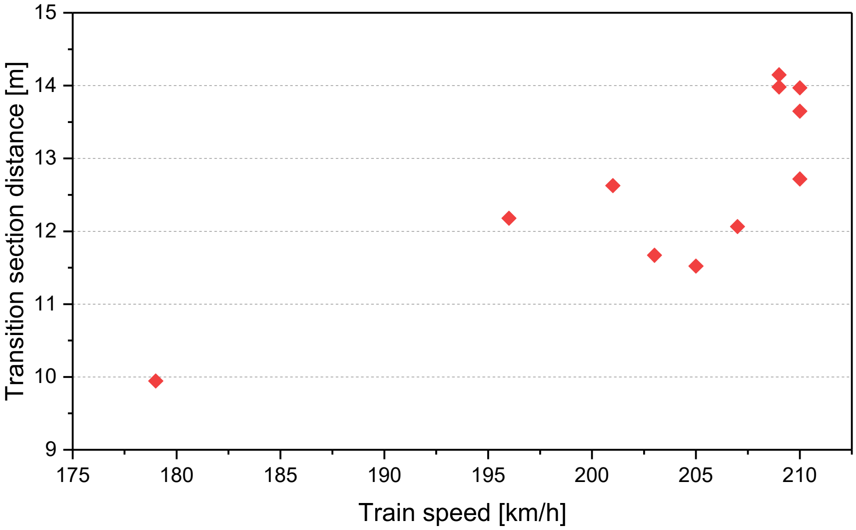

Fig. 4.19. Variation of the transition section distance.

The transition section distance of eleven train passages is estimated based on the dynamic crossing point spatial path, i.e., the distance between the initial and end contact points. The transition section distances and corresponding train speeds are shown in Fig. 4.19. The transition section distance exhibits an increasing tendency with increasing train speed. The measured transition section distances are approximately 14 and 10 m at train speeds of 210 and 179 km/h, respectively. This variation clearly shows a significant train speed dependency. However, there is also a variation of the transition section distance at similar train speeds, e.g., at 210 km/h, there is a registered variation of approximately 1.5m where one out of five measurement stands out. This finding indicates that the transition section distance not only affected by the train speed, but also by other factors, such as individual pantograph settings. To optimise and limit the maximum transition section distance for new catenaries, numerical simulations should be carried out considering the maximum allowable train speed on a given line.

4.5 Conclusion

This experimental study under regular traffic conditions evaluates the dynamic behaviour of pantograph-catenary interaction at an existing overlap span. A novel overlap measuring method was proposed and implemented at the midspan of a five-span overlap. Image sequences of eleven single- and two double-pantograph train passages were acquired with the VIBLITE, and a hand-held gun-type LiDAR was employed to measure the train speed. The dynamic crossing point of the two contact wires was estimated, and their spatial dynamic response was compared in detail under single- and double-pantograph passage conditions. This investigation studied the correlation between the train speed and transition section distance. The main conclusions are summarised as follows:

1) The results reveal that the pantograph contacts the second wire at a certain distance before reaching the static crossing point, which could cause a significant impulse in the contact wire and a high contact force.
2) A clear difference in maximum uplift and transition section distance is observed between single and double pantographs (i.e., the length where the pantograph runs on both wires in the overlap span), which could be related to both the contact forces and wear. The rear pantograph caused more severe dynamic interactions than those caused by the front pantograph under the double-pantograph train passage. The maximum uplifts under single- and double-pantograph train passage conditions are 51.91 mm and 56.69 mm, respectively, at a speed of 196 km/h, and there is a 9.21% increase under double-pantograph train passage.
3) The transition section distance exhibits an increasing tendency with increasing train speed. The measured transition section distances are approximately 14 and 10 m at train speeds of 210 and 179 km/h, respectively. The transition section distances under single- and double-pantograph train passage conditions are 12.18 m and 13.79 m, respectively, at the same train speed of 196 km/h, with a 13.22% increase.

Chapter 5

Conclusions

5.1 Concluding remarks

A set of vision-based hardware equipment for measuring line-like structures

Section 2.2 detailed a first version configuration of a hardware system for the wires' uplift measurement, and the system got updated in Section 4.2.1. The latest version consists of area scan cameras, optical lenses with fixed focal length, tripods, a hardware trigger, a solid-state drive, a laptop, a laser rangefinder and a LiDAR speed gun. This hardware system does not require track access and marker installation on contact wires, and it has good portability and robustness, rapid field deployment, easy operation, and high accuracy.

An image-processing algorithm for addressing the essential challenge of tracking slender wires without markers against noisy backgrounds

The challenge of a non-uniform or noisy background for identifying and tracking contact wire is discussed in Section 2.2. A line-tracking algorithm consists of a coarse search followed by a subpixel detection was proposed in Section 2.3. Section 2.3.1 detailed the workflow and principle of the coarse search, which comprises a subset search and a line search. Section 2.3.2 introduced a subpixel detection, and two different approaches were applied, i.e. a centreline detection algorithm and an edge detection algorithm, for different working conditions. The accuracy, robustness and applicability of the vision-based tracking system are demonstrated through numerical experiments (Section 2.4), the field uplift measurement of the railway catenary system (Section 2.5.1) and the identification of the contact wire in a diverse city environment (Section 2.5.2).

An uplift and damping investigation of an existing railway catenary span under regular train operation

Chapter 3 estimates the spatially distributed damping of an existing catenary span through uplift measurements under regular train operation. Section 3.1 discusses the importance of uplift and damping estimation of an existing catenary span and summarises the damping application in experiments and numerical simulations. The synchronous dynamic uplift response of the contact, messenger and stitch wires is revealed in Section 3.5. The spatially distributed damping of an existing catenary span is successfully estimated in Section 3.6 by using a covariance-driven stochastic subspace identification (Cov-SSI) method to analyse sixty-nine single/double-pantograph train passages. A small but clear train direction dependency of the damping distribution is observed over the entire span. Rayleigh damping coefficients are estimated and recommended for numerical models.

An experimental study of pantograph-catenary interaction and transition at the section overlap span

A measuring method for section overlap investigations is developed in Section 4.2.2 to obtain the height, uplift and crossing point of contact wires. The dynamic spatial moving paths of the crossing point under regular single- and double-pantograph train passages are studied to detail the whole process of the pantograph-catenary interaction and transition at the overlap span in Section 4.4.4 and 4.4.5. The analyses explore reasons for the high contact forces and the contact loss rendering arcing at section overlap spans. The correlation between the train speeds and transition section distance, i.e., the length where the pantograph runs on both contact wires, is studied in Section 4.4.6. The transition section distance was between 10 m and 14 m for train speeds around 200 km/h.

5.2 Suggestions for further work

Perform further data collection of the dynamic behaviour of railway catenary systems

The intention is to explore further a vision-based system and its use in railway measurements. The length of high-speed electric railways is increasing in the global railway network. The catenary dynamic behaviour is critical to ensure a robust and steady current collection quality for electric trains [93]. The vision-based line-tracking system (VIBLITE) has been extensively used to explore many railway catenary system response sides. VIBLITE can obtain verified high-accuracy uplift at any chosen point along the catenary, thus, beneficial for verification of numerical simulation and design specifications on existing and new systems. The latter is essential as new built or modified systems need to be approved according to contracted maximum specifications.

More case studies about the pantograph-catenary interaction will be performed to study the dynamic behaviour further. VIBLITE hardware and software are necessary for further improvement, e.g., increased sampling frequency up towards 800 Hz for high train speeds and high accuracy needed in wear model verification.

Develop a camera vibration reduction system that includes hardware and software

When vision-based systems are performed in the field, environmental conditions such as wind and foundation motions will make the camera devices vibrate. These unwanted vibrations contribute as noise affects the measurement accuracy. Therefore, camera vibration noise has been a concern when further improving field applications. The transitional vibration reduction method tracks the background structures as a static reference to roughly estimate the camera vibration [149]. However, it is difficult to find static reference points in the camera field of view in most field situations. Thus, it is necessary to develop a camera reduction system that can detect, record and calibrate the camera motion.

Trials have been conducted using a tri-axis gyroscope and a tri-axis accelerometer to calibrate the camera's spatial orientation change using a motion-processing unit (MPU). This system shows good response and will be further pursued to increase time-instant accuracy and response sensitivity. The challenge is to synchronise the camera and the sensor system to achieve accurate calibration. Initial theoretical and experimental studies are conducted to demonstrate the possibilities of increased accuracy and robustness of the additional sensor system.

Study machine learning-based inspection systems to monitor railway infrastructure properties and components

Visual inspection using machine learning has been widely applied in many engineering fields, e.g., crack detection [150,151], bolt-loosening detection [152-154]. This technique can identify and analyse components for damage or possibly missing members. Automated identification has been tested at Hell Bridge Test Arena and used on inspection data from Bane NOR bridge inspections. Furthermore, automated identification can also evaluate track and sleepers with fasteners, brackets and other components. Similarly, railway catenary systems can be inspected for issues with isolators, registration arm position, dropper positions, stagger, and wear. The system can also be used to monitor the catenary-pantograph interaction and other pantograph actions, including raising and lowering mechanisms.

References

[1] F. Kiessling, R. Puschmann, A. Schmieder, E. Schneider, Contact lines for electric railways: planning, design, implementation, maintenance, John Wiley & Sons, 2018.

[2] F. Trevithick, Life of Richard Trevithick: with an account of his inventions, E. & FN Spon, London; New York, 1872.

[3] C.H. Ellis, The pictorial encyclopedia of railways, Crown Publishers, 1968.

[4] A.J. Churella, From Steam to Diesel: Managerial Customs and Organizational Capabilities in the Twentieth-Century American Locomotive Industry, Princeton University Press, Princeton, New Jersey, 1998.

[5] M. Hohn, D. Stanfel, H.R. Figlhuber, Mödling–Hinterbrühl. Die erste elektrische Bahn Europas für Dauerbetrieb, Wien: Verlag Slezak, 1983.

[6] D. Zhan, D. Jing, M. Wu, D. Zhang, L. Yu, T. Chen, An Accurate and Efficient Vision Measurement Approach for Railway Catenary Geometry Parameters, IEEE Transactions on Instrumentation and Measurement 67 (2018) 2841-2853. https://doi.org/10.1109/TIM.2018.2830862.

[7] Z. Liu, Detection and Estimation Research of High-speed Railway Catenary, Springer, Singapore, 2017.

[8] S.B. Gao, Z.G. Liu, L. Yu, Detection and monitoring system of the pantograph-catenary in high-speed railway (6C), in: 2017 7th International Conference on Power Electronics Systems and Applications - Smart Mobility, Power Transfer & Security (PESA), 2017, pp. 1-7.

[9] W. Liu, Z. Liu, A. Núñez, Virtual Reality and Convolutional Neural Networks for Railway Catenary Support Components Monitoring, in: 2019 IEEE Intelligent Transportation Systems Conference (ITSC), Auckland, New Zealand, 2019, pp. 2183-2188.

[10] J. Pombo, J. Ambrósio, M. Pereira, F. Rauter, A. Collina, A. Facchinetti, Influence of the aerodynamic forces on the pantograph–catenary system for high-speed trains, Veh. Syst. Dyn. 47 (2009) 1327-1347. https://doi.org/10.1080/00423110802613402.

[11] The railway in numbers, 2019. https://www.banenor.no/Jernbanen/Jernbanen-i-tall/.

[12] J. Ambrósio, J. Pombo, M. Pereira, P. Antunes, A. Mósca, A computational procedure for the dynamic analysis of the catenary-pantograph interaction in high-speed trains, Journal of Theoretical and Applied Mechanics 50 (2012).

[13] M. Tan, N. Zhou, J. Wang, D. Zou, W. Zhang, G. Mei, A real-time impact detection and diagnosis system of catenary using measured strains by fibre Bragg grating sensors, Veh. Syst. Dyn. 57 (2019) 1924-1946. https://doi.org/10.1080/00423114.2018.1556396.

[14] G. Poetsch, J. Evans, R. Meisinger, W. KortÜM, W. Baldauf, A. Veitl, J. Wallaschek, Pantograph/Catenary Dynamics and Control, Veh. Syst. Dyn. 28 (1997) 159-195. https://doi.org/10.1080/00423119708969353.

[15] Jernbaneverket, Mekanisk systembeskrivelse av kontaktledningsanlegg, 2019. https://www.jernbanekompetanse.no/wiki/Mekanisk_systembeskrivelse_av_kontaktledningsanlegg#Ledningsf.C3.B8ring.

[16] P. Antunes, J. Ambrósio, J. Pombo, A. Facchinetti, A new methodology to study the pantograph–catenary dynamics in curved railway tracks, Veh. Syst. Dyn. 58 (2020) 425-452. https://doi.org/10.1080/00423114.2019.1583348.

[17] J. Pombo, J. Ambrósio, Multiple Pantograph Interaction With Catenaries in High-Speed Trains, Journal of Computational and Nonlinear Dynamics 7 (2012) 041008. https://doi.org/10.1115/1.4006734.

[18] Z. Xu, Y. Song, Z. Liu, Effective Measures to Improve Current Collection Quality for Double Pantographs and Catenary Based on Wave Propagation Analysis, IEEE Transactions on Vehicular Technology (2020) 1-1. https://doi.org/10.1109/TVT.2020.2985382.

[19] D. Zhang, S. Gao, L. Yu, G. Kang, D. Zhan, X. Wei, A Robust Pantograph-Catenary Interaction Condition Monitoring Method Based on Deep Convolutional Network, IEEE Transactions on Instrumentation and Measurement (2019) 1-1. https://doi.org/10.1109/TIM.2019.2920721.

[20] Jernbaneverket, Dynamisk systembeskrivelse av kontaktledningsanlegg, 2015. https://www.jernbanekompetanse.no/wiki/Dynamisk_systembeskrivelse_av_kontaktledningsanlegg.

[21] H. Möller, L. Grebner, D. Hofman, Stromabnehmerdiagnose im laufenden Betrieb durch stationäre Anhubmessung (Pantograph diagnosis under operation by stationary uplift management), Elektrische Bahnen 100 (2002) 198-203.

[22] M.T. Stickland, T.J. Scanlon, I.A. Craighead, J. Fernandez, An investigation into the mechanical damping characteristics of catenary contact wires and their effect on aerodynamic galloping instability, Proc. Inst. Mech. Eng. Part F: J.

Rail Rapid Transit 217 (2003) 63-71. https://doi.org/10.1243/095440903765762814.

[23] G. Laffont, N. Roussel, S. Rougeault, J. Boussoir, L. Maurin, P. Ferdinand, Innovative FBG sensing techniques for the railway industry: Application to overhead contact line monitoring, in: Proceedings of SPIE - 20th International Conference on Optical Fibre Sensors, SPIE, Edinburgh, United Kingdom, 2009, pp. 1-4.

[24] P. Nåvik, A. Rønnquist, S. Stichel, Identification of system damping in railway catenary wire systems from full-scale measurements, Eng. Struct. 113 (2016) 71-78. https://doi.org/10.1016/j.engstruct.2016.01.031.

[25] P. Nåvik, A. Rønnquist, S. Stichel, A wireless railway catenary structural monitoring system: Full-scale case study, Case Stud. Struct. Eng. 6 (2016) 22-30. https://doi.org/10.1016/j.csse.2016.05.003.

[26] O. Vo Van, E. Balmes, X. Lorang, Damping characterization of a high speed train catenary, International Symposium on Dynamics of Vehicles on Roads and Tracks, 2015, pp. 1505–1512.

[27] T.E. Thoresen, System for measuring the uplift from all pantographs passing the installed system (Product information), Oslo, Norway, 2008.

[28] G. Frøseth, P. Nåvik, A. Rønnquist, Operational displacement estimations of railway catenary systems by photogrammetry and the integration of acceleration time series, Int. J. Railw. Technol. 6 (2017) 71-92. https://doi.org/10.4203/ijrt.6.3.4.

[29] Y. Park, Y.-H. Cho, K. Lee, H.-J. Kim, I.-C. Kim, Development of an Uplift Measurement System for Overhead Contact Wire using High Speed Camera, J. Korean Inst. Electr. Electron. Mater. Eng. 22 (2009) 864-869. https://doi.org/10.4313/JKEM.2009.22.10.864.

[30] K. Karwowski, M. Mizan, D. Karkosinski, Monitoring of current collectors on the railway line, Transport 33 (2016) 177-185. https://doi.org/10.3846/16484142.2016.1144222.

[31] J. Hietzge, A. Stephan, Non-contact uplift measurement at overhead contact lines, Elektrische Bahnen 105 (2007) 276-279.

[32] C.A.L. Vázquez, M.M. Quintas, M.M. Romera, Non-contact sensor for monitoring catenary-pantograph interaction, in: 2010 IEEE International Symposium on Industrial Electronics, IEEE, Bari, Italy, 2010, pp. 482-487.

[33] D. Zou, W.H. Zhang, R.P. Li, N. Zhou, G.M. Mei, Determining damping characteristics of railway-overhead-wire system for finite-element analysis, Veh. Syst. Dyn. 54 (2016) 902-917. https://doi.org/10.1080/00423114.2016.1172715.

[34] D. Zou, N. Zhou, L. Rui Ping, G.M. Mei, W.H. Zhang, Experimental and simulation study of wave motion upon railway overhead wire systems, Proc. Inst. Mech. Eng. Part F: J. Rail Rapid Transit 231 (2017) 934-944. https://doi.org/10.1177/0954409716648718.

[35] C. Rainieri, G. Fabbrocino, Operational modal analysis of civil engineering structures, Springer, New York, 2014.

[36] C.-Z. Dong, F.N. Catbas, A review of computer vision–based structural health monitoring at local and global levels, Structural Health Monitoring (2020). https://doi.org/10.1177/1475921720935585.

[37] T. Jiang, G.T. Frøseth, A. Rønnquist, E. Fagerholt, A robust line-tracking photogrammetry method for uplift measurements of railway catenary systems in noisy backgrounds, Mech. Syst. Signal Process. 144 (2020) 106888. https://doi.org/10.1016/j.ymssp.2020.106888.

[38] W. Zhou, H. Xiao, Z. Wang, L. Chen, S. Fu, Dynamic target template matching for railway catenary suspension motion detection in wind area, International Journal of Distributed Sensor Networks 14 (2018). https://doi.org/10.1177/1550147718797956.

[39] F. Duan, Z. Liu, Y. Song, S. Derosa, A. Rønnquist, D. Zhai, Vibration Measurement and Wave Reflection Analysis in an Electrified Railway Catenary Based on Analytical Methods, IEEE Transactions on Instrumentation and Measurement 70 (2021) 1-12. https://doi.org/10.1109/TIM.2021.3063178.

[40] Y.-g. Wang, W. Zhou, D. Xie, Y. Zhang, W. Zhang, L. Han, X. Xue, Automatic Visual Inspection for Catenary on High-Speed Railways, ICRT 2017: Railway Development, Operations, and Maintenance, Reston, VA, USA, 2017, pp. 349-359.

[41] P. Tan, X. Li, Z. Wu, J. Ding, J. Ma, Y. Chen, Y. Fang, Y. Ning, Multialgorithm Fusion Image Processing for High Speed Railway Dropper Failure-Defect Detection, IEEE Transactions on Systems, Man, and Cybernetics: Systems (2019) 1-13. https://doi.org/10.1109/TSMC.2019.2938684.

[42] Y. Han, Z. Liu, D. Lee, G. Zhang, M. Deng, High-speed railway rod-insulator detection using segment clustering and deformable part models, in: 2016 IEEE International Conference on Image Processing (ICIP), Phoenix, AZ, USA, 2016, pp. 3852-3856.

[43] G. Zhang, Z. Liu, Y. Han, Automatic recognition for catenary insulators of high-speed railway based on contourlet transform and Chan–Vese model, Optik 127 (2016) 215-221. https://doi.org/10.1016/j.ijleo.2015.10.049.

[44] Y. Park, K. Lee, S.Y. Park, J.Y. Park, W.S. Choi, Implementation of Multi-functional Type Condition Monitoring System for Railway Catenary Systems, The Transactions of The Korean Institute of Electrical Engineers 64 (2015) 1406-1410. https://doi.org/10.5370/KIEE.2015.64.9.1406.

[45] Z. Liu, W. Liu, Z. Han, A high-precision detection approach for catenary geometry parameters of electrical railway, IEEE Trans. Instrum. Meas. 66 (2017) 1798-1808.

[46] C.X. You, A Study on Dynamic Measurement System of Contact Wire Wear in Electrified Railway, Procedia Computer Science 154 (2019) 210-220. https://doi.org/10.1016/j.procs.2019.06.032.

[47] J. Skibicki, M. Bartłomiejczyk, Analysis of measurement uncertainty for contact-less method used to measure the position of catenary contact wire, performed with the use of Monte Carlo method, Measurement 97 (2017) 203-217. https://doi.org/10.1016/j.measurement.2016.11.008.

[48] L. Jarzebowicz, S. Judek, 3D machine vision system for inspection of contact strips in railway vehicle current collectors, in: 2014 International Conference on Applied Electronics, Pilsen, Czech Republic, 2014, pp. 139-144.

[49] E.D. Stefano, C.A. Avizzano, M. Bergamasco, P. Masini, M. Menci, D. Russo, Automatic inspection of railway carbon strips based on multi-modal visual information, in: 2017 IEEE International Conference on Advanced Intelligent Mechatronics (AIM), Munich, Germany, 2017, pp. 178-184.

[50] S. Judek, J. Skibicki, Visual method for detecting critical damage in railway contact strips, Meas. Sci. Technol. 29 (2018) 055102.

[51] G. Karaduman, E. Akin, A New Approach Based on Predictive Maintenance Using the Fuzzy Classifier in Pantograph-Catenary Systems, IEEE Transactions on Intelligent Transportation Systems (2020) 1-11. https://doi.org/10.1109/TITS.2020.3042997.

[52] A. Landi, L. Menconi, L. Sani, Hough transform and thermo-vision for monitoring pantograph-catenary system, Proc. Inst. Mech. Eng. Part F: J. Rail Rapid Transit 220 (2006) 435-447.

[53] I. Aydin, M. Karakose, E. Akin, Anomaly detection using a modified kernel-based tracking in the pantograph–catenary system, Expert Systems with Applications 42 (2015) 938–948. 10.1016/j.eswa.2014.08.026.

[54] M. Karakose, O. Yaman, I. Aydin, E. Karakose, Real-time condition monitoring approach of pantograph-catenary system using FPGA, in: 2016 IEEE 14th International Conference on Industrial Informatics (INDIN), 2016, pp. 481-486.

[55] E. Karakose, M.T. Gencoglu, M. Karakose, I. Aydin, E. Akin, A New Experimental Approach Using Image Processing-Based Tracking for an

Efficient Fault Diagnosis in Pantograph–Catenary Systems, IEEE Transactions on Industrial Informatics 13 (2017) 635-643. https://doi.org/10.1109/TII.2016.2628042.

[56] G. Karaduman, M. Karakose, E. Akin, Deep learning based Arc detection in pantograph-catenary systems, in: 2017 10th International Conference on Electrical and Electronics Engineering (ELECO), Bursa, Turkey, 2017, pp. 904-908.

[57] D. Zheng, X. Lu, W. Quan, Y. Peng, Y. Liu, J.X. Chen, A Two-Stage Detection Method of Rigid Pantograph Catenary Contact Points Using DCNNS, in: 2020 3rd International Symposium on Power Electronics and Control Engineering (ISPECE 2020) IOP Publishing, Chongqing, China, 2021, pp. 012071.

[58] S. Huang, Y. Zhai, M. Zhang, X. Hou, Arc detection and recognition in pantograph–catenary system based on convolutional neural network, Information Sciences 501 (2019) 363-376. https://doi.org/10.1016/j.ins.2019.06.006.

[59] X. Hong, J. Zhou, Y. He, Damage detection of anchored region on the messenger cable based on matching pursuit algorithm, Mech. Syst. Signal Process. 130 (2019) 221-247. https://doi.org/10.1016/j.ymssp.2019.04.053.

[60] J. Ambrósio, J. Pombo, M. Pereira, P. Antunes, A. Mósca, Recent Developments in Pantograph-Catenary Interaction Modelling and Analysis, Int. J. Railw. Technol. 1 (2012) 249-278. https://doi.org/10.4203/ijrt.1.1.12.

[61] M. Bocciolone, G. Bucca, A. Collina, L. Comolli, Pantograph–catenary monitoring by means of fibre Bragg grating sensors: Results from tests in an underground line, Mech. Syst. Signal Process. 41 (2013) 226-238. https://doi.org/10.1016/j.ymssp.2013.06.030.

[62] C. Rainieri, G. Fabbrocino, Operational Modal Analysis of Civil Engineering Structures, Springer, New York, NY, 2014.

[63] H.A. Bruck, S.R. McNeill, M.A. Sutton, W.H. Peters, Digital image correlation using Newton-Raphson method of partial differential correction, Exp. Mech. 29 (1989) 261-267. https://doi.org/10.1007/BF02321405.

[64] B. Pan, K. Li, W. Tong, Fast, robust and accurate digital image correlation calculation without redundant computations, Exp. Mech. 53 (2013) 1277-1289. https://doi.org/10.1007/s11340-013-9717-6.

[65] B. Pan, K. Li, A fast digital image correlation method for deformation measurement, Opt. Lasers Eng. 49 (2011) 841-847. https://doi.org/10.1016/j.optlaseng.2011.02.023.

[66] M. Bornert, F. Brémand, P. Doumalin, J.C. Dupré, M. Fazzini, M. Grédiac, F. Hild, S. Mistou, J. Molimard, J.J. Orteu, L. Robert, Y. Surrel, P. Vacher, B.

Wattrisse, Assessment of Digital Image Correlation Measurement Errors: Methodology and Results, Exp. Mech. 49 (2009) 353-370. https://doi.org/10.1007/s11340-008-9204-7.

[67] B. Pan, K. Qian, H. Xie, A. Asundi, Two-dimensional digital image correlation for in-plane displacement and strain measurement: a review, Meas. Sci. Technol. 20 (2009) 062001. https://doi.org/10.1088/0957-0233/20/6/062001.

[68] L. Yu, B. Pan, Single-camera high-speed stereo-digital image correlation for full-field vibration measurement, Mech. Syst. Signal Process. 94 (2017) 374-383. https://doi.org/10.1016/j.ymssp.2017.03.008.

[69] D.L.B.R. Jurjo, C. Magluta, N. Roitman, P. Batista Gonçalves, Analysis of the structural behavior of a membrane using digital image processing, Mech. Syst. Signal Process. 54-55 (2015) 394-404. https://doi.org/10.1016/j.ymssp.2014.08.010.

[70] J. Soons, P. Lava, D. Debruyne, J. Dirckx, Full-field optical deformation measurement in biomechanics: Digital speckle pattern interferometry and 3D digital image correlation applied to bird beaks, J. Mech. Behav. Biomed. Mater. 14 (2012) 186-191. https://doi.org/10.1016/j.jmbbm.2012.05.004.

[71] B. Pan, L. Tian, X. Song, Real-time, non-contact and targetless measurement of vertical deflection of bridges using off-axis digital image correlation, NDT E Int. 79 (2016) 73-80. https://doi.org/10.1016/j.ndteint.2015.12.006.

[72] S.-W. Kim, N.-S. Kim, Dynamic characteristics of suspension bridge hanger cables using digital image processing, NDT E Int. 59 (2013) 25-33. https://doi.org/10.1016/j.ndteint.2013.05.002.

[73] J.-E. Dufour, B. Beaubier, F. Hild, S. Roux, CAD-based Displacement Measurements with Stereo-DIC, Exp. Mech. 55 (2015) 1657-1668. https://doi.org/10.1007/s11340-015-0065-6.

[74] C. Warren, C. Niezrecki, P. Avitabile, P. Pingle, Comparison of FRF measurements and mode shapes determined using optically image based, laser, and accelerometer measurements, Mech. Syst. Signal Process. 25 (2011) 2191-2202. https://doi.org/10.1016/j.ymssp.2011.01.018.

[75] F. Hild, S. Roux, Digital Image Correlation: from Displacement Measurement to Identification of Elastic Properties – a Review, Strain 42 (2006) 69-80. https://doi.org/10.1111/j.1475-1305.2006.00258.x.

[76] L. Felipe-Sesé, F.A. Díaz, Damage methodology approach on a composite panel based on a combination of fringe projection and 2D digital image correlation, Mech. Syst. Signal Process. 101 (2018) 467-479. https://doi.org/10.1016/j.ymssp.2017.09.002.

[77] P. Poozesh, J. Baqersad, C. Niezrecki, P. Avitabile, E. Harvey, R. Yarala, Large-area photogrammetry based testing of wind turbine blades, Mech. Syst. Signal Process. 86 (2017) 98-115. https://doi.org/10.1016/j.ymssp.2016.07.021.

[78] R. Huňady, M. Hagara, A new procedure of modal parameter estimation for high-speed digital image correlation, Mech. Syst. Signal Process. 93 (2017) 66-79. https://doi.org/10.1016/j.ymssp.2017.02.010.

[79] L. Huynh, J. Rotella, M.D. Sangid, Fatigue behavior of IN718 microtrusses produced via additive manufacturing, Mater. Des. 105 (2016) 278-289. https://doi.org/10.1016/j.matdes.2016.05.032.

[80] A.S. Wu, D.W. Brown, M. Kumar, G.F. Gallegos, W.E. King, An experimental investigation into additive manufacturing-induced residual stresses in 316L stainless steel, Metall. Mater. Trans. A 45 (2014) 6260-6270. https://doi.org/10.1007/s11661-014-2549-x.

[81] P. Chowdhury, H. Sehitoglu, R. Rateick, Damage tolerance of carbon-carbon composites in aerospace application, Carbon 126 (2018) 382-393. https://doi.org/10.1016/j.carbon.2017.10.019.

[82] M. Flores, D. Mollenhauer, V. Runatunga, T. Beberniss, D. Rapking, M. Pankow, High-speed 3D digital image correlation of low-velocity impacts on composite plates, Compos. Part B: Eng. 131 (2017) 153-164. https://doi.org/10.1016/j.compositesb.2017.07.078.

[83] Y. Du, F.A. Diaz, R.L. Burguete, E.A. Patterson, Evaluation using digital image correlation of stress intensity factors in an aerospace panel, Exp. Mech. 51 (2011) 45-57. https://doi.org/10.1007/s11340-010-9335-5.

[84] A. Borkar, M. Hayes, M.T. Smith, Robust lane detection and tracking with ransac and Kalman filter, in: 2009 16th IEEE International Conference on Image Processing (ICIP), IEEE, Cairo, Egypt, 2009, pp. 3261-3264.

[85] H.-C. Kuo, L.-J. Wu, An image tracking system for welded seams using fuzzy logic, J. Mater. Process. Technol. 120 (2002) 169-185. https://doi.org/10.1016/S0924-0136(01)01155-4.

[86] Z. Li, Y. Liu, R. Walker, R. Hayward, J. Zhang, Towards automatic power line detection for a UAV surveillance system using pulse coupled neural filter and an improved Hough transform, Mach. Vis. Appl. 21 (2010) 677-686. https://doi.org/10.1007/s00138-009-0206-y.

[87] I. Golightly, D. Jones, Corner detection and matching for visual tracking during power line inspection, Image Vis. Comput. 21 (2003) 827-840. https://doi.org/10.1016/S0262-8856(03)00097-0.

[88] R.O. Duda, P.E. Hart, Use of the Hough Transform to Detect Lines and Curves in Pictures, Commun. ACM 15 (1972) 11-15. https://doi.org/10.1145/361237.361242.

[89] A. Trujillo-Pino, K. Krissian, M. Alemán-Flores, D. Santana-Cedrés, Accurate subpixel edge location based on partial area effect, Image Vis. Comput. 31 (2013) 72-90. https://doi.org/10.1016/j.imavis.2012.10.005.

[90] J. Javh, J. Slavič, M. Boltežar, The subpixel resolution of optical-flow-based modal analysis, Mech. Syst. Signal Process. 88 (2017) 89-99. https://doi.org/10.1016/j.ymssp.2016.11.009.

[91] P.M. Atkinson, I.M. Sargent, G.M. Foody, J. Williams, Exploring the Geostatistical Method for Estimating the Signal-to-Noise Ratio of Images, Photogramm. Eng. Remote Sensing 73 (2007) 841-850. https://doi.org/10.14358/PERS.73.7.841.

[92] P. Nåvik, S. Derosa, A. Rønnquist, Development of an index for quantification of structural dynamic response in a railway catenary section, Eng. Struct. 222 (2020) 111154. https://doi.org/10.1016/j.engstruct.2020.111154.

[93] Y. Song, Z. Liu, A. Rxnnquist, P. Navik, Z. Liu, Contact Wire Irregularity Stochastics and Effect on High-speed Railway Pantograph-Catenary Interactions, IEEE Transactions on Instrumentation and Measurement (2020) 1-1. https://doi.org/10.1109/TIM.2020.2987457.

[94] Y. Song, P. Antunes, J. Pombo, Z. Liu, A methodology to study high-speed pantograph-catenary interaction with realistic contact wire irregularities, Mechanism and Machine Theory (2020) 103940. https://doi.org/10.1016/j.mechmachtheory.2020.103940.

[95] A. Rønnquist, P. Nåvik, Dynamic assessment of existing soft catenary systems using modal analysis to explore higher train velocities: a case study of a Norwegian contact line system, Veh. Syst. Dyn. 53 (2015) 756-774. https://doi.org/10.1080/00423114.2015.1013040.

[96] S. Bruni, J. Ambrosio, A. Carnicero, Y.H. Cho, L. Finner, M. Ikeda, S.Y. Kwon, J.-P. Massat, S. Stichel, M. Tur, W. Zhang, The results of the pantograph–catenary interaction benchmark, Veh. Syst. Dyn. 53 (2015) 412-435. https://doi.org/10.1080/00423114.2014.953183.

[97] J.-H. Seo, S.-W. Kim, I.-H. Jung, T.-W. Park, J.-Y. Mok, Y.-G. Kim, J.-B. Chai, Dynamic analysis of a pantograph–catenary system using absolute nodal coordinates, Veh. Syst. Dyn. 44 (2006) 615-630. 10.1080/00423110500373721.

[98] S. Gregori, M. Tur, J.E. Tarancón, F.J. Fuenmayor, Stochastic Monte Carlo simulations of the pantograph–catenary dynamic interaction to allow for

uncertainties introduced during catenary installation, Veh. Syst. Dyn. 57 (2019) 471-492. https://doi.org/10.1080/00423114.2018.1473617.

[99] Y. Song, Z. Wang, Z. Liu, R. Wang, A spatial coupling model to study dynamic performance of pantograph-catenary with vehicle-track excitation, Mech. Syst. Signal Process. 151 (2021) 107336. https://doi.org/10.1016/j.ymssp.2020.107336.

[100] S. Pil Jung, Y. Guk Kim, J. Sung Paik, T. Won Park, Estimation of Dynamic Contact Force Between a Pantograph and Catenary Using the Finite Element Method, Journal of Computational and Nonlinear Dynamics 7 (2012). https://doi.org/10.1115/1.4006733.

[101] Z. Liu, P.-A. Jönsson, S. Stichel, A. Rønnquist, Implications of the operation of multiple pantographs on the soft catenary systems in Sweden, Proc. Inst. Mech. Eng. Part F: J. Rail Rapid Transit 230 (2016) 971-983. https://doi.org/10.1177/0954409714559317.

[102] A. Cazzani, M. Cattani, R. Mauro, F. Stochino, A simplified model for railway catenary wire dynamics, European Journal of Environmental and Civil Engineering 21 (2017) 936-959. https://doi.org/10.1080/19648189.2016.1245631.

[103] Y.H. Cho, J.M. Lee, S.Y. Park, E.S. Lee, Robust measurement of damping ratios of a railway contact wire using wavelet transforms, in: Key Engineering Materials, Trans Tech Publ, 2006, pp. 1629-1635.

[104] W. Zhang, Y. Liu, G. Mei, Evaluation of the coupled dynamical response of a pantograph—catenary system: contact force and stresses, Veh. Syst. Dyn. 44 (2006) 645-658. https://doi.org/10.1080/00423110600744656.

[105] Y.H. Cho, Numerical simulation of the dynamic responses of railway overhead contact lines to a moving pantograph, considering a nonlinear dropper, Journal of Sound and Vibration 315 (2008) 433-454. https://doi.org/10.1016/j.jsv.2008.02.024.

[106] J.P. Bianchi, E. Balmès, G. Vermot Des Roches, A. Bobillot, Using modal damping for full model transient analysis. Application to pantograph/catenary vibration, in: ISMA, Leuven, Belgium, 2010, pp. 376.

[107] C.-Z. Dong, O. Celik, F.N. Catbas, Marker-free monitoring of the grandstand structures and modal identification using computer vision methods, Structural Health Monitoring 18 (2018) 1491-1509. https://doi.org/10.1177/1475921718806895.

[108] C.T. do Cabo, N.A. Valente, Z. Mao, Motion magnification for optical-based structural health monitoring, Health Monitoring of Structural and Biological Systems IX, 2020, pp. 1138122.

[109] D. Gorjup, J. Slavič, M. Boltežar, Frequency domain triangulation for full-field 3D operating-deflection-shape identification, Mech. Syst. Signal Process. 133 (2019) 106287. https://doi.org/10.1016/j.ymssp.2019.106287.

[110] J. Javh, J. Slavič, M. Boltežar, Measuring full-field displacement spectral components using photographs taken with a DSLR camera via an analogue Fourier integral, Mech. Syst. Signal Process. 100 (2018) 17-27. https://doi.org/10.1016/j.ymssp.2017.07.024.

[111] D. Gorjup, J. Slavič, A. Babnik, M. Boltežar, Still-camera multiview Spectral Optical Flow Imaging for 3D operating-deflection-shape identification, Mech. Syst. Signal Process. 152 (2021) 107456. https://doi.org/10.1016/j.ymssp.2020.107456.

[112] Y. Xu, Photogrammetry-based structural damage detection by tracking a visible laser line, Structural Health Monitoring 19 (2019) 322-336. https://doi.org/10.1177/1475921719840354.

[113] A. Khadka, B. Fick, A. Afshar, M. Tavakoli, J. Baqersad, Non-contact vibration monitoring of rotating wind turbines using a semi-autonomous UAV, Mech. Syst. Signal Process. 138 (2020) 106446. https://doi.org/10.1016/j.ymssp.2019.106446.

[114] Z. Lai, I. Alzugaray, M. Chli, E. Chatzi, Full-field structural monitoring using event cameras and physics-informed sparse identification, Mech. Syst. Signal Process. 145 (2020) 106905. https://doi.org/10.1016/j.ymssp.2020.106905.

[115] T. Jiang, G.T. Frøseth, A. Rønnquist, E. Fagerholt, A vision-based line-tracking technique, Zenodo, 2020, Version 1.1. https://doi.org/10.5281/zenodo.3685219.

[116] BaslerAG, Basler Product Documentation, 2018. https://docs.baslerweb.com.

[117] Y.F. Xu, A photogrammetry-based experimental modal analysis method by tracking visible laser spots, Measurement 151 (2020) 106963. https://doi.org/10.1016/j.measurement.2019.106963.

[118] C.-Z. Dong, S. Bas, F.N. Catbas, Investigation of vibration serviceability of a footbridge using computer vision-based methods, Eng. Struct. 224 (2020) 111224. https://doi.org/10.1016/j.engstruct.2020.111224.

[119] J.A. Walker, Estimating velocities and accelerations of animal locomotion: a simulation experiment comparing numerical differentiation algorithms, The Journal of Experimental Biology 201 (1998) 981.

[120] P. Welch, The use of fast Fourier transform for the estimation of power spectra: A method based on time averaging over short, modified periodograms, IEEE Transactions on Audio and Electroacoustics 15 (1967) 70-73. https://doi.org/10.1109/TAU.1967.1161901.

[121] H. Henao, S.H. Kia, G. Capolino, Torsional-Vibration Assessment and Gear-Fault Diagnosis in Railway Traction System, IEEE Transactions on Industrial Electronics 58 (2011) 1707-1717. https://doi.org/10.1109/TIE.2011.2106094.

[122] Y. Yang, G. Liu, C. Liu, Fine interrelation between track irregularities and vehicle responses: multi-scale time-dependent correlation analysis, Veh. Syst. Dyn. (2020) 1-19. https://doi.org/10.1080/00423114.2020.1741653.

[123] P. Nåvik, A. Rønnquist, Uplift-Monitoring for Dynamic Assessment of Electrical Railway Contact Lines, in: Dynamics of Civil Structures, Springer International Publishing, Cham, 2015, pp. 237-244.

[124] T.-C.I. Aravanis, J.S. Sakellariou, S.D. Fassois, Spectral analysis of railway vehicle vertical vibration under normal operating conditions, International Journal of Rail Transportation 4 (2016) 193-207. https://doi.org/10.1080/23248378.2016.1221749.

[125] A. Fenerci, O. Øiseth, A. Rønnquist, Long-term monitoring of wind field characteristics and dynamic response of a long-span suspension bridge in complex terrain, Eng. Struct. 147 (2017) 269-284. https://doi.org/10.1016/j.engstruct.2017.05.070.

[126] K.A. Kvåle, O. Øiseth, Characterization of the Wave Field Around an Existing End-Supported Pontoon Bridge from Simulated Data, in: Proceedings of the International Conference on Earthquake Engineering and Structural Dynamics, Springer International Publishing, Cham, 2019, pp. 345-359.

[127] K.A. Kvåle, O. Øiseth, A. Rønnquist, Operational modal analysis of an end-supported pontoon bridge, Eng. Struct. 148 (2017) 410-423. https://doi.org/10.1016/j.engstruct.2017.06.069.

[128] K.A. Kvåle, O. Øiseth, Structural monitoring of an end-supported pontoon bridge, Marine Structures 52 (2017) 188-207. https://doi.org/10.1016/j.marstruc.2016.12.004.

[129] A. Fenerci, O. Øiseth, Site-specific data-driven probabilistic wind field modeling for the wind-induced response prediction of cable-supported bridges, Journal of Wind Engineering and Industrial Aerodynamics 181 (2018) 161-179. https://doi.org/10.1016/j.jweia.2018.09.002.

[130] A. Fenerci, O. Øiseth, Strong wind characteristics and dynamic response of a long-span suspension bridge during a storm, Journal of Wind Engineering and Industrial Aerodynamics 172 (2018) 116-138. https://doi.org/10.1016/j.jweia.2017.10.030.

[131] Ø.W. Petersen, O. Øiseth, E.-M. Lourens, The use of inverse methods for response estimation of long-span suspension bridges with uncertain wind

loading conditions, Journal of Civil Structural Health Monitoring 9 (2019) 21-36. https://doi.org/10.1007/s13349-018-0319-y.

[132] S. Rathi, R.L. Dua, P. Singh, Spectrum sensing in cognitive radio using MIMO technique, International Journal of Soft Computing and Engineering (IJSCE) 1 (2011) 259-265.

[133] D. Anastasio, A. Fasana, L. Garibaldi, S. Marchesiello, Analytical investigation of railway overhead contact wire dynamics and comparison with experimental results, Mech. Syst. Signal Process. 116 (2019) 277-292. https://doi.org/10.1016/j.ymssp.2018.06.021.

[134] K.A. Kvåle, KOMA, Zenodo, 2020, Version 1.0.2. https://doi.org/10.5281/zenodo.3760635.

[135] Y. Song, M. Zhang, H. Wang, A Response Spectrum Analysis of Wind Deflection in Railway Overhead Contact Lines Using Pseudo-Excitation Method, IEEE Transactions on Vehicular Technology 70 (2021) 1169-1178. https://doi.org/10.1109/TVT.2021.3054459.

[136] S. Gregori, J. Gil, M. Tur, J.E. Tarancón, F.J. Fuenmayor, Analysis of the overlap section in a high-speed railway catenary by means of numerical simulations, Eng. Struct. 221 (2020) 110963. https://doi.org/10.1016/j.engstruct.2020.110963.

[137] F. Vesali, H. Molatefi, M.A. Rezvani, B. Moaveni, M. Hecht, New control approaches to improve contact quality in the conventional spans and overlap section in a high-speed catenary system, Proc. Inst. Mech. Eng. Part F: J. Rail Rapid Transit 233 (2019) 988-999. https://doi.org/10.1177/0954409718822861.

[138] H. Elvsaas, A Parametric Study of Dynamic Response in Numerical Pantograph-Catenary Interaction Model, NTNU, Trondheim, 2018.

[139] Y. Song, A. Rønnquist, T. Jiang, P. Nåvik, Identification of short-wavelength contact wire irregularities in electrified railway pantograph–catenary system, Mechanism and Machine Theory 162 (2021) 104338. https://doi.org/10.1016/j.mechmachtheory.2021.104338.

[140] T. Jiang, A. Rønnquist, Y. Song, G.T. Frøseth, P. Nåvik, A detailed investigation of uplift and damping of a railway catenary span in traffic using a vision-based line-tracking system (Preprint), (2021).

[141] M. Shimizu, Y. Fujii, Improvement of Structure of Contact Wire on Overlap Sections of Shinkansen, Quarterly Report of RTRI 41 (2000) 159-162. 10.2219/rtriqr.41.159.

[142] P. Harèll, L. Drugge, M. Reijm, Study of Critical Sections in Catenary Systems During Multiple Pantograph Operation, Proc. Inst. Mech. Eng. Part F: J. Rail Rapid Transit 219 (2005) 203-211. https://doi.org/10.1243/095440905X8934.

[143] T. Kuraoka, I. Ideno, Research on Reduction of Wear of Contact Wires in Overlap Sections, JR East Technical Review (2012).

[144] K. Zaletelj, V. Agrež, J. Slavič, R. Petkovšek, M. Boltežar, Laser-light speckle formation for deflection-shape identification using digital image correlation, Mech. Syst. Signal Process. 161 (2021) 107899. https://doi.org/10.1016/j.ymssp.2021.107899.

[145] M. Southwick, Z. Mao, C. Niezrecki, A Complex Convolution Kernel-Based Optical Displacement Sensor, IEEE Sensors Journal 20 (2020) 9753-9762. https://doi.org/10.1109/JSEN.2020.2986240.

[146] L. Rui, E. Zappa, A. Collina, Vision-based measurement of crack generation and evolution during static testing of concrete sleepers, Engineering Fracture Mechanics 224 (2020) 106715. https://doi.org/10.1016/j.engfracmech.2019.106715.

[147] Y.H. Cho, K. Lee, Y. Park, B. Kang, K.-n. Kim, Influence of contact wire pre-sag on the dynamics of pantograph–railway catenary, International Journal of Mechanical Sciences 52 (2010) 1471-1490. https://doi.org/10.1016/j.ijmecsci.2010.04.002.

[148] A. Collina, S. Bruni, Numerical Simulation of Pantograph-Overhead Equipment Interaction, Veh. Syst. Dyn. 38 (2002) 261-291. https://doi.org/10.1076/vesd.38.4.261.8286.

[149] L. Luo, M.Q. Feng, Z.Y. Wu, Robust vision sensor for multi-point displacement monitoring of bridges in the field, Eng. Struct. 163 (2018) 255-266. https://doi.org/10.1016/j.engstruct.2018.02.014.

[150] M.R. Saleem, J.-W. Park, J.-H. Lee, H.-J. Jung, M.Z. Sarwar, Instant bridge visual inspection using an unmanned aerial vehicle by image capturing and geo-tagging system and deep convolutional neural network, Structural Health Monitoring (2020) 1475921720932384. https://doi.org/10.1177/1475921720932384.

[151] D. Lydon, S.E. Taylor, M. Lydon, J. Early, A review of Vision based Methods for Pothole Detection and Road Profile Analysis, Civil Engineering Research in Ireland 2020, Cork Institute of Technology, Cork, Ireland, 2020.

[152] T.-C. Huynh, J.-H. Park, H.-J. Jung, J.-T. Kim, Quasi-autonomous bolt-loosening detection method using vision-based deep learning and image processing, Automation in Construction 105 (2019) 102844. https://doi.org/10.1016/j.autcon.2019.102844.

[153] H.C. Pham, Q.-B. Ta, J.-T. Kim, D.-D. Ho, X.-L. Tran, T.-C. Huynh, Bolt-Loosening Monitoring Framework Using an Image-Based Deep Learning and Graphical Model, Sensors 20 (2020). https://doi.org/10.3390/s20123382.

[154] D.Q. Tran, J.-W. Kim, K.D. Tola, W. Kim, S. Park, Artificial Intelligence-Based Bolt Loosening Diagnosis Using Deep Learning Algorithms for Laser Ultrasonic Wave Propagation Data, Sensors 20 (2020). https://doi.org/10.3390/s20185329.

DEPARTMENT OF STRUCTURAL ENGINEERING
NORWEGIAN UNIVERSITY OF SCIENCE AND TECHNOLOGY

N–7491 TRONDHEIM, NORWAY
Telephone: +47 73 59 47 00

"Reliability Analysis of Structural Systems using Nonlinear Finite Element Methods",
C. A. Holm, 1990:23, ISBN 82-7119-178-0.

"Uniform Stratified Flow Interaction with a Submerged Horizontal Cylinder",
Ø. Arntsen, 1990:32, ISBN 82-7119-188-8.

"Large Displacement Analysis of Flexible and Rigid Systems Considering
Displacement-Dependent Loads and Nonlinear Constraints",
K. M. Mathisen, 1990:33, ISBN 82-7119-189-6.

"Solid Mechanics and Material Models including Large Deformations",
E. Levold, 1990:56, ISBN 82-7119-214-0, ISSN 0802-3271.

"Inelastic Deformation Capacity of Flexurally-Loaded Aluminium Alloy Structures",
T. Welo, 1990:62, ISBN 82-7119-220-5, ISSN 0802-3271.

"Visualization of Results from Mechanical Engineering Analysis",
K. Aamnes, 1990:63, ISBN 82-7119-221-3, ISSN 0802-3271.

"Object-Oriented Product Modeling for Structural Design",
S. I. Dale, 1991:6, ISBN 82-7119-258-2, ISSN 0802-3271.

"Parallel Techniques for Solving Finite Element Problems on Transputer Networks",
T. H. Hansen, 1991:19, ISBN 82-7119-273-6, ISSN 0802-3271.

"Statistical Description and Estimation of Ocean Drift Ice Environments",
R. Korsnes, 1991:24, ISBN 82-7119-278-7, ISSN 0802-3271.

"Properties of concrete related to fatigue damage: with emphasis on high strength
concrete",
G. Petkovic, 1991:35, ISBN 82-7119-290-6, ISSN 0802-3271.

"Turbidity Current Modelling",
B. Brørs, 1991:38, ISBN 82-7119-293-0, ISSN 0802-3271.

“Zero-Slump Concrete: Rheology, Degree of Compaction and Strength. Effects of Fillers as Part Cement-Replacement”,
C. Sørensen, 1992:8, ISBN 82-7119-357-0, ISSN 0802-3271.

“Nonlinear Analysis of Reinforced Concrete Structures Exposed to Transient Loading”,
K. V. Høiseth, 1992:15, ISBN 82-7119-364-3, ISSN 0802-3271.

“Finite Element Formulations and Solution Algorithms for Buckling and Collapse Analysis of Thin Shells”,
R. O. Bjærum, 1992:30, ISBN 82-7119-380-5, ISSN 0802-3271.

“Response Statistics of Nonlinear Dynamic Systems”,
J. M. Johnsen, 1992:42, ISBN 82-7119-393-7, ISSN 0802-3271.

“Digital Models in Engineering. A Study on why and how engineers build and operate digital models for decisison support”,
J. Høyte, 1992:75, ISBN 82-7119-429-1, ISSN 0802-3271.

“Sparse Solution of Finite Element Equations”,
A. C. Damhaug, 1992:76, ISBN 82-7119-430-5, ISSN 0802-3271.

“Some Aspects of Floating Ice Related to Sea Surface Operations in the Barents Sea”,
S. Løset, 1992:95, ISBN 82-7119-452-6, ISSN 0802-3271.

“Modelling of Cyclic Plasticity with Application to Steel and Aluminium Structures”,
O. S. Hopperstad, 1993:7, ISBN 82-7119-461-5, ISSN 0802-3271.

“The Free Formulation: Linear Theory and Extensions with Applications to Tetrahedral Elements with Rotational Freedoms”,
G. Skeie, 1993:17, ISBN 82-7119-472-0, ISSN 0802-3271.

“Høyfast betongs motstand mot piggdekkslitasje. Analyse av resultater fra prøving i Veisliter'n”,
T. Tveter, 1993:62, ISBN 82-7119-522-0, ISSN 0802-3271.

“A Nonlinear Finite Element Based on Free Formulation Theory for Analysis of Sandwich Structures”,
O. Aamlid, 1993:72, ISBN 82-7119-534-4, ISSN 0802-3271.

“The Effect of Curing Temperature and Silica Fume on Chloride Migration and Pore Structure of High Strength Concrete”,
C. J. Hauck, 1993:90, ISBN 82-7119-553-0, ISSN 0802-3271.

"Failure of Concrete under Compressive Strain Gradients",
G. Markeset, 1993:110, ISBN 82-7119-575-1, ISSN 0802-3271.

"An experimental study of internal tidal amphidromes in Vestfjorden",
J. H. Nilsen, 1994:39, ISBN 82-7119-640-5, ISSN 0802-3271.

"Structural analysis of oil wells with emphasis on conductor design",
H. Larsen, 1994:46, ISBN 82-7119-648-0, ISSN 0802-3271.

"Adaptive methods for non-linear finite element analysis of shell structures",
K. M. Okstad, 1994:66, ISBN 82-7119-670-7, ISSN 0802-3271.

"On constitutive modelling in nonlinear analysis of concrete structures",
O. Fyrileiv, 1994:115, ISBN 82-7119-725-8, ISSN 0802-3271.

"Fluctuating wind load and response of a line-like engineering structure with emphasis on motion-induced wind forces",
J. Bogunovic Jakobsen, 1995:62, ISBN 82-7119-809-2, ISSN 0802-3271.

"An experimental study of beam-columns subjected to combined torsion, bending and axial actions",
A. Aalberg, 1995:66, ISBN 82-7119-813-0, ISSN 0802-3271.

"Scaling and cracking in unsealed freeze/thaw testing of Portland cement and silica fume concretes",
S. Jacobsen, 1995:101, ISBN 82-7119-851-3, ISSN 0802-3271.

"Damping of water waves by submerged vegetation. A case study of laminaria hyperborea",
A. M. Dubi, 1995:108, ISBN 82-7119-859-9, ISSN 0802-3271.

"The dynamics of a slope current in the Barents Sea",
Sheng Li, 1995:109, ISBN 82-7119-860-2, ISSN 0802-3271.

"Modellering av delmaterialenes betydning for betongens konsistens",
Ernst Mørtsell, 1996:12, ISBN 82-7119-894-7, ISSN 0802-3271.

"Bending of thin-walled aluminium extrusions",
Birgit Søvik Opheim, 1996:60, ISBN 82-7119-947-1, ISSN 0802-3271.

"Material modelling of aluminium for crashworthiness analysis",
Torodd Berstad, 1996:89, ISBN 82-7119-980-3, ISSN 0802-3271.

"Estimation of structural parameters from response measurements on submerged floating tunnels",
Rolf Magne Larssen, 1996:119, ISBN 82-471-0014-2, ISSN 0802-3271.

"Numerical modelling of plain and reinforced concrete by damage mechanics",
Mario A. Polanco-Loria, 1997:20, ISBN 82-471-0049-5, ISSN 0802-3271.

"Nonlinear random vibrations - numerical analysis by path integration methods",
Vibeke Moe, 1997:26, ISBN 82-471-0056-8, ISSN 0802-3271.

"Numerical prediction of vortex-induced vibration by the finite element method",
Joar Martin Dalheim, 1997:63, ISBN 82-471-0096-7, ISSN 0802-3271.

"Time domain calculations of buffeting response for wind sensitive structures",
Ketil Aas-Jakobsen, 1997:148, ISBN 82-471-0189-0, ISSN 0802-3271.

"A numerical study of flow about fixed and flexibly mounted circular cylinders",
Trond Stokka Meling, 1998:48, ISBN 82-471-0244-7, ISSN 0802-3271.

"Estimation of chloride penetration into concrete bridges in coastal areas",
Per Egil Steen, 1998:89, ISBN 82-471-0290-0, ISSN 0802-3271.

"Stress-resultant material models for reinforced concrete plates and shells",
Jan Arve Øverli, 1998:95, ISBN 82-471-0297-8, ISSN 0802-3271.

"Chloride binding in concrete. Effect of surrounding environment and concrete composition",
Claus Kenneth Larsen, 1998:101, ISBN 82-471-0337-0, ISSN 0802-3271.

"Rotational capacity of aluminium alloy beams",
Lars A. Moen, 1999:1, ISBN 82-471-0365-6, ISSN 0802-3271.

"Stretch Bending of Aluminium Extrusions",
Arild H. Clausen, 1999:29, ISBN 82-471-0396-6, ISSN 0802-3271.

"Aluminium and Steel Beams under Concentrated Loading",
Tore Tryland, 1999:30, ISBN 82-471-0397-4, ISSN 0802-3271.

"Engineering Models of Elastoplasticity and Fracture for Aluminium Alloys",
Odd-Geir Lademo, 1999:39, ISBN 82-471-0406-7, ISSN 0802-3271.

"Kapasitet og duktilitet av dybelforbindelser i trekonstruksjoner",
Jan Siem, 1999:46, ISBN 82-471-0414-8, ISSN 0802-3271.

“Etablering av distribuert ingeniørarbeid; Teknologiske og organisatoriske erfaringer fra en norsk ingeniørbedrift”,
Lars Line, 1999:52, ISBN 82-471-0420-2, ISSN 0802-3271.

“Estimation of Earthquake-Induced Response”,
Símon Ólafsson, 1999:73, ISBN 82-471-0443-1, ISSN 0802-3271.

“Coastal Concrete Bridges: Moisture State, Chloride Permeability and Aging Effects”,
Ragnhild Holen Relling, 1999:74, ISBN 82-471-0445-8, ISSN 0802-3271.

“Capacity Assessment of Titanium Pipes Subjected to Bending and External Pressure”,
Arve Bjørset, 1999:100, ISBN 82-471-0473-3, ISSN 0802-3271.

“Validation of Numerical Collapse Behaviour of Thin-Walled Corrugated Panels”,
Håvar Ilstad, 1999:101, ISBN 82-471-0474-1, ISSN 0802-3271.

“Strength and Ductility of Welded Structures in Aluminium Alloys”,
Miroslaw Matusiak, 1999:113, ISBN 82-471-0487-3, ISSN 0802-3271.

“Thermal Dilation and Autogenous Deformation as Driving Forces to Self-Induced Stresses in High Performance Concrete”,
Øyvind Bjøntegaard, 1999:121, ISBN 82-7984-002-8, ISSN 0802-3271.

“Some Aspects of Ski Base Sliding Friction and Ski Base Structure”,
Dag Anders Moldestad, 1999:137, ISBN 82-7984-019-2, ISSN 0802-3271.

“Electrode reactions and corrosion resistance for steel in mortar and concrete”,
Roy Antonsen, 2000:10, ISBN 82-7984-030-3, ISSN 0802-3271.

“Hydro-Physical Conditions in Kelp Forests and the Effect on Wave Damping and Dune Erosion. A case study on Laminaria Hyperborea”,
Stig Magnar Løvås, 2000:28, ISBN 82-7984-050-8, ISSN 0802-3271.

“Random Vibration and the Path Integral Method”,
Christian Skaug, 2000:39, ISBN 82-7984-061-3, ISSN 0802-3271.

“Buckling and geometrical nonlinear beam-type analyses of timber structures”,
Trond Even Eggen, 2000:56, ISBN 82-7984-081-8, ISSN 0802-3271.

“Structural Crashworthiness of Aluminium Foam-Based Components”,
Arve Grønsund Hanssen, 2000:76, ISBN 82-7984-102-4, ISSN 0809-103X.

"Measurements and simulations of the consolidation in first-year sea ice ridges, and some aspects of mechanical behaviour",
Knut V. Høyland, 2000:94, ISBN 82-7984-121-0, ISSN 0809-103X.

"Kinematics in Regular and Irregular Waves based on a Lagrangian Formulation",
Svein Helge Gjøsund, 2000-86, ISBN 82-7984-112-1, ISSN 0809-103X.

"Self-Induced Cracking Problems in Hardening Concrete Structures",
Daniela Bosnjak, 2000-121, ISBN 82-7984-151-2, ISSN 0809-103X.

"Ballistic Penetration and Perforation of Steel Plates",
Tore Børvik, 2000:124, ISBN 82-7984-154-7, ISSN 0809-103X.

"Freeze-Thaw resistance of Concrete. Effect of: Curing Conditions, Moisture Exchange and Materials",
Terje Finnerup Rønning, 2001:14, ISBN 82-7984-165-2, ISSN 0809-103X

"Structural behaviour of post tensioned concrete structures. Flat slab. Slabs on ground",
Steinar Trygstad, 2001:52, ISBN 82-471-5314-9, ISSN 0809-103X.

"Slipforming of Vertical Concrete Structures. Friction between concrete and slipform panel",
Kjell Tore Fosså, 2001:61, ISBN 82-471-5325-4, ISSN 0809-103X.

"Some numerical methods for the simulation of laminar and turbulent incompressible flows",
Jens Holmen, 2002:6, ISBN 82-471-5396-3, ISSN 0809-103X.

"Improved Fatigue Performance of Threaded Drillstring Connections by Cold Rolling",
Steinar Kristoffersen, 2002:11, ISBN: 82-421-5402-1, ISSN 0809-103X.

"Deformations in Concrete Cantilever Bridges: Observations and Theoretical Modelling",
Peter F. Takâcs, 2002:23, ISBN 82-471-5415-3, ISSN 0809-103X.

"Stiffened aluminium plates subjected to impact loading",
Hilde Giæver Hildrum, 2002:69, ISBN 82-471-5467-6, ISSN 0809-103X.

"Full- and model scale study of wind effects on a medium-rise building in a built up area",
Jónas Thór Snæbjørnsson, 2002:95, ISBN82-471-5495-1, ISSN 0809-103X.

"Evaluation of Concepts for Loading of Hydrocarbons in Ice-infested water",
Arnor Jensen, 2002:114, ISBN 82-417-5506-0, ISSN 0809-103X.

"Numerical and Physical Modelling of Oil Spreading in Broken Ice",
Janne K. Økland Gjøsteen, 2002:130, ISBN 82-471-5523-0, ISSN 0809-103X.

"Diagnosis and protection of corroding steel in concrete",
Franz Pruckner, 20002:140, ISBN 82-471-5555-4, ISSN 0809-103X.

"Tensile and Compressive Creep of Young Concrete: Testing and Modelling",
Dawood Atrushi, 2003:17, ISBN 82-471-5565-6, ISSN 0809-103X.

"Rheology of Particle Suspensions. Fresh Concrete, Mortar and Cement Paste with Various Types of Lignosulfonates",
Jon Elvar Wallevik, 2003:18, ISBN 82-471-5566-4, ISSN 0809-103X.

"Oblique Loading of Aluminium Crash Components",
Aase Reyes, 2003:15, ISBN 82-471-5562-1, ISSN 0809-103X.

"Utilization of Ethiopian Natural Pozzolans",
Surafel Ketema Desta, 2003:26, ISSN 82-471-5574-5, ISSN:0809-103X.

"Behaviour and strength prediction of reinforced concrete structures with discontinuity regions",
Helge Brå, 2004:11, ISBN 82-471-6222-9, ISSN 1503-8181.

"High-strength steel plates subjected to projectile impact. An experimental and numerical study",
Sumita Dey, 2004:38, ISBN 82-471-6282-2 (printed version), ISBN 82-471-6281-4 (electronic version), ISSN 1503-8181.

"Alkali-reactive and inert fillers in concrete. Rheology of fresh mixtures and expansive reactions",
Bård M. Pedersen, 2004:92, ISBN 82-471-6401-9 (printed version), ISBN 82-471-6400-0 (electronic version), ISSN 1503-8181.

"On the Shear Capacity of Steel Girders with Large Web Openings",
Nils Christian Hagen, 2005:9 ISBN 82-471-6878-2 (printed version), ISBN 82-471-6877-4 (electronic version), ISSN 1503-8181.

"Behaviour of aluminium extrusions subjected to axial loading",
Østen Jensen, 2005:7, ISBN 82-471-6873-1 (printed version), ISBN 82-471-6872-3 (electronic version), ISSN 1503-8181.

"Thermal Aspects of corrosion of Steel in Concrete",
Jan-Magnus Østvik, 2005:5, ISBN 82-471-6869-3 (printed version), ISBN 82-471-6868 (electronic version), ISSN 1503-8181.

“Mechanical and adaptive behaviour of bone in relation to hip replacement. A study of bone remodelling and bone grafting”,
Sébastien Muller, 2005:34, ISBN 82-471-6933-9 (printed version), ISBN 82-471-6932-0 (electronic version), ISSN 1503-8181.

“Analysis of geometrical nonlinearities with applications to timber structures”,
Lars Wollebæk, 2005:74, ISBN 82-471-7050-5 (printed version), ISBN 82-471-7019-1 (electronic version), ISSN 1503-8181.

“Pedestrian induced lateral vibrations of slender footbridges”,
Anders Rönnquist, 2005:102, ISBN 82-471-7082-5 (printed version), ISBN 82-471-7081-7 (electronic version), ISSN 1503-8181.

“Initial Strength Development of Fly Ash and Limestone Blended Cements at Various Temperatures Predicted by Ultrasonic Pulse Velocity”,
Tom Ivar Fredvik, 2005:112, ISBN 82-471-7105-8 (printed version), ISBN 82-471-7103-1 (electronic version), ISSN 1503-8181.

“Behaviour and modelling of thin-walled cast components”,
Cato Dørum, 2005:128, ISBN 82-471-7140-6 (printed version), ISBN 82-471-7139-2 (electronic version), ISSN 1503-8181.

“Behaviour and modelling of selfpiercing riveted connections”,
Raffaele Porcaro, 2005:165, ISBN 82-471-7219-4 (printed version), ISBN 82-471-7218-6 (electronic version), ISSN 1503-8181.

“Behaviour and Modelling og Aluminium Plates subjected to Compressive Load”,
Lars Rønning, 2005:154, ISBN 82-471-7169-1 (printed version), ISBN 82-471-7195-3 (electronic version), ISSN 1503-8181.

“Bumper beam-longitudinal system subjected to offset impact loading”,
Satyanarayana Kokkula, 2005:193, ISBN 82-471-7280-1 (printed version), ISBN 82-471-7279-8 (electronic version), ISSN 1503-8181.

“Control of Chloride Penetration into Concrete Structures at Early Age”,
Guofei Liu, 2006:46, ISBN 82-471-7838-9 (printed version), ISBN 82-471-7837-0 (electronic version), ISSN 1503-8181.

“Modelling of Welded Thin-Walled Aluminium Structures”,
Ting Wang, 2006:78, ISBN 82-471-7907-5 (printed version), ISBN 82-471-7906-7 (electronic version), ISSN 1503-8181.

“Time-variant reliability of dynamic systems by importance sampling and probabilistic analysis of ice loads”,
Anna Ivanova Olsen, 2006:139, ISBN 82-471-8041-3 (printed version), ISBN 82-471-8040-5 (electronic version), ISSN 1503-8181.

“Fatigue life prediction of an aluminium alloy automotive component using finite element analysis of surface topography”,
Sigmund Kyrre Ås, 2006:25, ISBN 82-471-7791-9 (printed version), ISBN 82-471-7791-9 (electronic version), ISSN 1503-8181.

“Constitutive models of elastoplasticity and fracture for aluminium alloys under strain path change”,
Dasharatha Achani, 2006:76, ISBN 82-471-7903-2 (printed version), ISBN 82-471-7902-4 (electronic version), ISSN 1503-8181.

“Simulations of 2D dynamic brittle fracture by the Element-free Galerkin method and linear fracture mechanics”,
Tommy Karlsson, 2006:125, ISBN 82-471-8011-1 (printed version), ISBN 82-471-8010-3 (electronic version), ISSN 1503-8181.

“Penetration and Perforation of Granite Targets by Hard Projectiles”,
Chong Chiang Seah, 2006:188, ISBN 82-471-8150-9 (printed version), ISBN 82-471-8149-5 (electronic version), ISSN 1503-8181.

“Deformations, strain capacity and cracking of concrete in plastic and early hardening phases”,
Tor Arne Hammer, 2007:234, ISBN 978-82-471-5191-4 (printed version), ISBN 978-82-471-5207-2 (electronic version), ISSN 1503-8181.

“Crashworthiness of dual-phase high-strength steel: Material and Component behaviour”,
Venkatapathi Tarigopula, 2007:230, ISBN 82-471-5076-4 (printed version), ISBN 82-471-5093-1 (electronic version), ISSN 1503-8181.

“Fibre reinforcement in load carrying concrete structures”,
Åse Lyslo Døssland, 2008:50, ISBN 978-82-471-6910-0 (printed version), ISBN 978-82-471-6924-7 (electronic version), ISSN 1503-8181.

“Low-velocity penetration of aluminium plates”,
Frode Grytten, 2008:46, ISBN 978-82-471-6826-4 (printed version), ISBN 978-82-471-6843-1 (electronic version), ISSN 1503-8181.

“Robustness studies of structures subjected to large deformations”,
Ørjan Fyllingen, 2008:24, ISBN 978-82-471-6339-9 (printed version), ISBN 978-82-471-6342-9 (electronic version), ISSN 1503-8181.

"Constitutive modelling of morsellised bone",
Knut Birger Lunde, 2008:92, ISBN 978-82-471-7829-4 (printed version), ISBN 978-82-471-7832-4 (electronic version), ISSN 1503-8181.

"Experimental Investigations of Wind Loading on a Suspension Bridge Girder",
Bjørn Isaksen, 2008:131, ISBN 978-82-471-8656-5 (printed version), ISBN 978-82-471-8673-2 (electronic version), ISSN 1503-8181.

"Cracking Risk of Concrete Structures in The Hardening Phase",
Guomin Ji, 2008:198, ISBN 978-82-471-1079-9 (printed version), ISBN 978-82-471-1080-5 (electronic version), ISSN 1503-8181.

"Modelling and numerical analysis of the porcine and human mitral apparatus",
Victorien Emile Prot, 2008:249, ISBN 978-82-471-1192-5 (printed version), ISBN 978-82-471-1193-2 (electronic version), ISSN 1503-8181.

"Strength analysis of net structures",
Heidi Moe, 2009:48, ISBN 978-82-471-1468-1 (printed version), ISBN 978-82-471-1469-8 (electronic version), ISSN1503-8181.

"Numerical analysis of ductile fracture in surface cracked shells",
Espen Berg, 2009:80, ISBN 978-82-471-1537-4 (printed version), ISBN 978-82-471-1538-1 (electronic version), ISSN 1503-8181.

"Subject specific finite element analysis of bone – for evaluation of the healing of a leg lengthening and evaluation of femoral stem design",
Sune Hansborg Pettersen, 2009:99, ISBN 978-82-471-1579-4 (printed version), ISBN 978-82-471-1580-0 (electronic version), ISSN 1503-8181.

"Evaluation of fracture parameters for notched multi-layered structures",
Lingyun Shang, 2009:137, ISBN 978-82-471-1662-3 (printed version), ISBN 978-82-471-1663-0 (electronic version), ISSN 1503-8181.

"Modelling of Dynamic Material Behaviour and Fracture of Aluminium Alloys for Structural Applications",
Yan Chen, 2009:69, ISBN 978-82-471-1515-2 (printed version), ISBN 978-82 471-1516-9 (electronic version), ISSN 1503-8181.

"Nanomechanics of polymer and composite particles",
Jianying He 2009:213, ISBN 978-82-471-1828-3 (printed version), ISBN 978-82-471-1829-0 (electronic version), ISSN 1503-8181.

"Mechanical properties of clear wood from Norway spruce",
Kristian Berbom Dahl 2009:250, ISBN 978-82-471-1911-2 (printed version) ISBN 978-82-471-1912-9 (electronic version), ISSN 1503-8181.

“Modeling of the degradation of TiB_2 mechanical properties by residual stresses and liquid Al penetration along grain boundaries”,
Micol Pezzotta 2009:254, ISBN 978-82-471-1923-5 (printed version) ISBN 978-82-471-1924-2 (electronic version) ISSN 1503-8181.

“Effect of welding residual stress on fracture”,
Xiabo Ren 2010:77, ISBN 978-82-471-2115-3 (printed version) ISBN 978-82-471-2116-0 (electronic version), ISSN 1503-8181.

“Pan-based carbon fiber as anode material in cathodic protection system for concrete structures”,
Mahdi Chini 2010:122, ISBN 978-82-471-2210-5 (printed version) ISBN 978-82-471-2213-6 (electronic version), ISSN 1503-8181.

“Structural Behaviour of deteriorated and retrofitted concrete structures”,
Irina Vasililjeva Sæther 2010:171, ISBN 978-82-471-2315-7 (printed version) ISBN 978-82-471-2316-4 (electronic version) ISSN 1503-8181.

“Prediction of local snow loads on roofs”,
Vivian Meløysund 2010:247, ISBN 978-82-471-2490-1 (printed version) ISBN 978-82-471-2491-8 (electronic version) ISSN 1503-8181.

“Behaviour and modelling of polymers for crash applications”,
Virgile Delhaye 2010:251, ISBN 978-82-471-2501-4 (printed version) ISBN 978-82-471-2502-1 (electronic version) ISSN 1503-8181.

“Blended cement with reducted CO_2 emission – Utilizing the Fly Ash-Limestone Synergy”,
Klaartje De Weerdt 2011:32, ISBN 978-82-471-2584-7 (printed version) ISBN 978-82-471-2584-4 (electronic version) ISSN 1503-8181.

“Chloride induced reinforcement corrosion in concrete” Concept of critical chloride content – methods and mechanisms”,
Ueli Angst 2011:113, ISBN 978-82-471-2769-9 (printed version) ISBN 978-82-471-2763-6 (electronic version) ISSN 1503-8181.

“A thermo-electric-Mechanical study of the carbon anode and contact interface for Energy savings in the production of aluminium”,
Dag Herman Andersen 2011:157, ISBN 978-82-471-2859-6 (printed version) ISBN 978-82-471-2860-2 (electronic version) ISSN 1503-8181.

"Structural Capacity of Anchorage Ties in Masonry Veneer Walls Subjected to Earthquake. The implications of Eurocode 8 and Eurocode 6 on a typical Norwegain veneer wall ",
Ahmed Mohamed Yousry Hamed 2011:181, ISBN 978-82-471-2911-1 (printed version) ISBN 978-82-471-2912-8 (electronic ver.) ISSN 1503-8181.

"Work-hardening behaviour in age-hardenable Al-Zn-Mg(-Cu) alloys",
Ida Westermann , 2011:247, ISBN 978-82-471-3056-8 (printed ver.) ISBN 978-82-471-3057-5 (electronic ver.) ISSN 1503-8181.

"Behaviour and modelling of selfpiercing riveted connections using aluminium rivets",
Nguyen-Hieu Hoang, 2011:266, ISBN 978-82-471-3097-1 (printed ver.) ISBN 978-82-471-3099-5 (electronic ver.) ISSN 1503-8181.

"Fibre reinforced concrete",
Sindre Sandbakk, 2011:297, ISBN 978-82-471-3167-1 (printed ver.) ISBN 978-82-471-3168-8 (electronic ver) ISSN 1503:8181.

"Dynamic behaviour of cablesupported bridges subjected to strong natural wind",
Ole Andre Øiseth, 2011:315, ISBN 978-82-471-3209-8 (printed ver.) ISBN 978-82-471-3210-4 (electronic ver.) ISSN 1503-8181.

"Constitutive modeling of solargrade silicon materials",
Julien Cochard, 2011:307, ISBN 978-82-471-3189-3 (printed ver). ISBN 978-82-471-3190-9 (electronic ver.) ISSN 1503-8181.

"Constitutive behavior and fracture of shape memory alloys",
Jim Stian Olsen, 2012:57, ISBN 978-82-471-3382-8 (printed ver.) ISBN 978-82-471-3383-5 (electronic ver.) ISSN 1503-8181.

"Field measurements in mechanical testing using close-range photogrammetry and digital image analysis",
Egil Fagerholt, 2012:95, ISBN 978-82-471-3466-5 (printed ver.) ISBN 978-82-471-3467-2 (electronic ver.) ISSN 1503-8181.

"Towards a better under standing of the ultimate behaviour of lightweight aggregate concrete in compression and bending",
Håvard Nedrelid, 2012:123, ISBN 978-82-471-3527-3 (printed ver.) ISBN 978-82-471-3528-0 (electronic ver.) ISSN 1503-8181.

"Numerical simulations of blood flow in the left side of the heart",
Sigrid Kaarstad Dahl, 2012:135, ISBN 978-82-471-3553-2 (printed ver.) ISBN 978-82-471-3555-6 (electronic ver.) ISSN 1503-8181.

“Moisture induced stresses in glulam”,
Vanessa Angst-Nicollier, 2012:139, ISBN 978-82-471-3562-4 (printed ver.) ISBN 978-82-471-3563-1 (electronic ver.) ISSN 1503-8181.

“Biomechanical aspects of distraction osteogensis”,
Valentina La Russa, 2012:250, ISBN 978-82-471-3807-6 (printed ver.) ISBN 978-82-471-3808-3 (electronic ver.) ISSN 1503-8181.

“Ductile fracture in dual-phase steel. Theoretical, experimental and numerical study”,
Gaute Gruben, 2012:257, ISBN 978-82-471-3822-9 (printed ver.) ISBN 978-82-471-3823-6 (electronic ver.) ISSN 1503-8181.

“Damping in Timber Structures”,
Nathalie Labonnote, 2012:263, ISBN 978-82-471-3836-6 (printed ver.) ISBN 978-82-471-3837-3 (electronic ver.) ISSN 1503-8181.

“Biomechanical modeling of fetal veins: The umbilical vein and ductus venosus bifurcation”,
Paul Roger Leinan, 2012:299, ISBN 978-82-471-3915-8 (printed ver.) ISBN 978-82-471-3916-5 (electronic ver.) ISSN 1503-8181.

“Large-Deformation behaviour of thermoplastics at various stress states”,
Anne Serine Ognedal, 2012:298, ISBN 978-82-471-3913-4 (printed ver.) ISBN 978-82-471-3914-1 (electronic ver.) ISSN 1503-8181.

“Hardening accelerator for fly ash blended cement”,
Kien Dinh Hoang, 2012:366, ISBN 978-82-471-4063-5 (printed ver.) ISBN 978-82-471-4064-2 (electronic ver.) ISSN 1503-8181.

“From molecular structure to mechanical properties”,
Jianyang Wu, 2013:186, ISBN 978-82-471-4485-5 (printed ver.) ISBN 978-82-471-4486-2 (electronic ver.) ISSN 1503-8181.

“Experimental and numerical study of hybrid concrete structures”,
Linn Grepstad Nes, 2013:259, ISBN 978-82-471-4644-6 (printed ver.) ISBN 978-82-471-4645-3 (electronic ver.) ISSN 1503-8181.

“Mechanics of ultra-thin multi crystalline silicon wafers”,
Saber Saffar, 2013:199, ISBN 978-82-471-4511-1 (printed ver.) ISBN 978-82-471-4513-5 (electronic ver). ISSN 1503-8181.

“Through process modelling of welded aluminium structures”,
Anizahyati Alisibramulisi, 2013:325, ISBN 978-82-471-4788-7 (printed ver.) ISBN 978-82-471-4789-4 (electronic ver.) ISSN 1503-8181.

“Combined blast and fragment loading on steel plates”,
Knut Gaarder Rakvåg, 2013:361, ISBN978-82-471-4872-3 (printed ver.) ISBN 978-82-4873-0 (electronic ver.). ISSN 1503-8181.

“Characterization and modelling of the anisotropic behaviour of high-strength aluminium alloy”,
Marion Fourmeau, 2014:37, ISBN 978-82-326-0008-3 (printed ver.) ISBN 978-82-326-0009-0 (electronic ver.) ISSN 1503-8181.

“Behaviour of threated steel fasteners at elevated deformation rates”,
Henning Fransplass, 2014:65, ISBN 978-82-326-0054-0 (printed ver.) ISBN 978-82-326-0055-7 (electronic ver.) ISSN 1503-8181.

“Sedimentation and Bleeding”,
Ya Peng, 2014:89, ISBN 978-82-326-0102-8 (printed ver.) ISBN 978-82-326-0103-5 (electric ver.) ISSN 1503-8181.

“Impact against X65 offshore pipelines”,
Martin Kristoffersen, 2014:362, ISBN 978-82-326-0636-8 (printed ver.) ISBN 978-82-326-0637-5 (electronic ver.) ISSN 1503-8181.

“Formability of aluminium alloy subjected to prestrain by rolling”,
Dmitry Vysochinskiy, 2014:363,, ISBN 978-82-326-0638-2 (printed ver.) ISBN 978-82-326-0639-9 (electronic ver.) ISSN 1503-8181.

“Experimental and numerical study of Yielding, Work-Hardening and anisotropy in textured AA6xxx alloys using crystal plasticity models”,
Mikhail Khadyko, 2015:28, ISBN 978-82-326-0724-2 (printed ver.) ISBN 978-82-326-0725-9 (electronic ver.) ISSN 1503-8181.

“Behaviour and Modelling of AA6xxx Aluminium Alloys Under a Wide Range of Temperatures and Strain Rates”,
Vincent Vilamosa, 2015:63, ISBN 978-82-326-0786-0 (printed ver.) ISBN 978-82-326-0787-7 (electronic ver.) ISSN 1503-8181.

“A Probabilistic Approach in Failure Modelling of Aluminium High Pressure Die-Castings”,
Octavian Knoll, 2015:137, ISBN 978-82-326-0930-7 (printed ver.) ISBN 978-82-326-0931-4 (electronic ver.) ISSN 1503-8181.

“Ice Abrasion on Marine Concrete Structures”,
Egil Møen, 2015:189, ISBN 978-82-326-1034-1 (printed ver.) ISBN 978-82-326-1035-8 (electronic ver.) ISSN 1503-8181.

“Fibre Orientation in Steel-Fibre-Reinforced Concrete”,
Giedrius Zirgulis, 2015:229, ISBN 978-82-326-1114-0 (printed ver.) ISBN 978-82-326-1115-7 (electronic ver.) ISSN 1503-8181.

“Effect of spatial variation and possible interference of localised corrosion on the residual capacity of a reinforced concrete beam”,
Mohammad Mahdi Kioumarsi, 2015:282, ISBN 978-82-326-1220-8 (printed ver.) ISBN 978-82-1221-5 (electronic ver.) ISSN 1503-8181.

“The role of concrete resistivity in chloride-induced macro-cell corrosion”,
Karla Horbostel, 2015:324, ISBN 978-82-326-1304-5 (printed ver.) ISBN 978-82-326-1305-2 (electonic ver.) ISSN 1503-8181.

“Flowable fibre-reinforced concrete for structural applications”,
Elena Vidal Sarmiento, 2015-335, ISBN 978-82-326-1324-3 (printed ver.) ISBN 978-82-326-1325-0 (electronic ver.) ISSN 1503-8181.

“Development of chushed sand for concrete production with microproportioning”,
Rolands Cepuritis, 2016:19, ISBN 978-82-326-1382-3 (printed ver.) ISBN 978-82-326-1383-0 (electronic ver.) ISSN 1503-8181.

“Withdrawal properties of threaded rods embedded in glued-laminated timer elements”,
Haris Stamatopoulos, 2016:48, ISBN 978-82-326-1436-3 (printed ver.) ISBN 978-82-326-1437-0 (electronic ver.) ISSN 1503-8181.

“An Experimental and numerical study of thermoplastics at large deformation”,
Marius Andersen, 2016:191, ISBN 978-82-326-1720-3 (printed ver.) ISBN 978-82-326-1721-0 (electronic ver.) ISSN 1503-8181.

“Modeling and Simulation of Ballistic Impact”,
Jens Kristian Holmen, 2016:240, ISBN 978-82-326-1818-7 (printed ver). ISBN 978-82-326-1819-4 (electronic ver.) ISSN 1503-8181.

“Early age crack assessment of concrete structures”,
Anja B. Estensen Klausen, 2016:256, ISBN 978-82-326-1850-7 (printed ver). ISBN 978-82-326-1851-4 (electronic ver.) ISSN 1503-8181.

“Uncertainty quantification and sensitivity analysis for cardiovascular models”,
Vinzenz Gregor Eck, 2016:234, ISBN 978-82-326-1806-4 (printed ver.) ISBN 978-82-326-1807-1 (electronic ver.) ISSN 1503-8181.

"Dynamic behaviour of existing and new railway catenary systems under Norwegain conditions",
Petter Røe Nåvik, 2016:298, ISBN 978-82-326-1935-1 (printed ver.) ISBN 978-82-326-1934-4 (electronic ver.) ISSN 1503-8181.

"Mechanical behaviour of particle-filled elastomers at various temperatures",
Arne Ilseng, 2016-295, ISBN978-82-326-1928-3 (printed ver.) ISBN 978-82-326-1929-0 (electronic ver.) ISSN 1503-8181.

"Nanotechnology for Anti-Icing Application",
Zhiwei He, 2016:348, ISBN 978-82-326-2038-8 (printed ver.) ISBN 978-82-326-2019-5 (electronic ver.) ISSN 1503-8181.

"Conduction Mechanisms in Conductive Adhesives with Metal-Coated Polyer Spheres",
Sigurd Rolland Pettersen, 2016:349, ISBN 978-326-2040-1 (printed ver,) ISBN 978-82-326-2041-8 (electronic ver.) ISSN 1503-8181.

"The interaction between calcium lignosulfonate and cement",
Alessia Colombo, 2017:20, ISBN 978-82-326-2122-4 (printed ver.) ISBN 978-82-326-2123-1 (electronic ver.) ISSN 1503-8181.

"Behaviour and Modelling of Flexible Structures Subjected to Blast Loading",
Vegard Aune, 2017:101, ISBN 978-82-326-2274-0 (printed ver.) ISBN 978-82-326-2275-7 (electronic ver.) ISSN 1503-8181.

"Behaviour of steel connections under quasi-static and impact loading",
Erik Løhre Grimsmo, 2017:159, ISBN 978-82-326-2390-7 (printed ver.) ISBN 978-82-326-2391-4 (electronic ver.) ISSN 1503-8181.

"An experimental and numerical study of cortical bone at he macro and Nano-scale",
Masoud Ramenzanzadehkoldeh, 2017:208, ISBN 978-82-326-2488-1 (printed ver.) ISBN 978-82-326-2489-8 (electronic ver.) ISSN 1503-8181.

"Optoelectrical Properties of a Novel Organic Semiconductor: 6,13-Dichloropentacene",
Mao Wang, 2017:130, ISBN 978-82-326-2332-7 (printed ver.) ISBN 978-82-326-2333-4) (electronic ver.) ISSN 1503-8181.

"Core-shell structured microgels and their behavior at oil and water interface",
Yi Gong, 2017:182, ISBN 978-82-326-2436-2 (printed. ver.) ISBN 978-82-326-2437-9 (electronic ver.) ISSN 1503-8181.

"Aspects of design of reinforced concrete structures using nonliear finite element analyses",
Morten Engen, 2017:149, ISBN 978-82-326-2370-9 (printed ver.) ISBN 978-82-326-2371-6 (electronic ver.) ISSN 1503-8181.

"Numerical studies on ductile failure of aluminium alloys",
Lars Edvard Dæhli, 2017:284, ISBN 978-82-326-2636-6 (printed ver.) ISBN 978-82-326-2637-3 (electronic ver.) ISSN 1503-8181.

"Modelling and Assessment of Hydrogen Embrittlement in Steels and Nickel Alloys",
Haiyang Yu, 2017:278, ISBN 978-82-326-2624-3 (printed. ver.) ISBN 978-82-326-2625-0 (electronic ver.) ISSN 1503-8181.

"Network arch timber bridges with light timber deck on transverse crossbeams",
Anna Weronika Ostrycharczyk, 2017:318, ISBN 978-82-326-2704-2 (printed ver.) ISBN 978-82-326-2705-9 (electronic ver.) ISSN 1503-8181.

"Splicing of Large Glued Laminated Timber Elements by Use of Long Threated Rods",
Martin Cepelka, 2017:320, ISBN 978-82-326-2708-0 (printed ver.) ISBN 978-82-326-2709-7 (electronic ver.) ISSN 1503-8181.

"Thermomechanical behaviour of semi-crystalline polymers: experiments, modelling and simulation",
Joakim Johnsen, 2017:317, ISBN 978-82-326-2702-8 (printed ver.) ISBN 978-82-326-2703-5 (electronic ver.) ISSN 1503-8181.

"Small-Scale Plasiticity under Hydrogen Environment",
Kai Zhao, 2017:356, ISBN 978-82-326-2782-0 (printed ver.) ISBN 978-82-326-2783-7 (electronic er.) ISSN 1503-8181.

"Risk and Reliability Based Calibration of Structural Design Codes",
Michele Baravalle, 2017:342, ISBN 978-82-326-2752-3 (printed ver,) ISBN 978-82-326-2753-0 (electronic ver.) ISSN 1503-8181.

"Dynamic behaviour of floating bridges exposed to wave excitation",
Knut Andreas Kvåle, 2017:365, ISBN 978-82-326-2800-1 (printed ver.) ISBN 978-82-326-2801-8 (electronic ver.) ISSN 1503-8181.

"Dolomite calcined clay composite cement – hydration and durability",
Alisa Lydia Machner, 2018:39, ISBN 978-82-326-2872-8 (printed ver.). ISBN 978-82-326-2873-5 (electronic ver.) ISSN 1503-8181.

“Modelling of the self-excited forces for bridge decks subjected to random motions: an experimental study”,
Bartosz Siedziako, 2018:52, ISBN 978-82-326-2896-4 (printed ver.). ISBN 978-82-326-2897-1 (electronic ver.) ISSN 1503-8181.

“A probabilistic-based methodology for evaluation of timber facade constructions”,
Klodian Gradeci, 2018:69, ISBN 978-82-326-2928-2 (printed ver.) ISBN 978-82-326-2929-9 (electronic ver.) ISSN 1503-8181.

“Behaviour and modelling of flow-drill screw connections”,
Johan Kolstø Sønstabø, 2018:73, ISBN 978-82-326-2936-7 (printed ver.) ISBN 978-82-326-2937-4 (electronic ver.) ISSN 1503-8181.

“Full-scale investigation of the effects of wind turbulence characteristics on dynamic behavior of long-span cable-supported bridges in complex terrain”,
Aksel Fenerci, 2018 100, ISBN 9978-82-326-2990-9 (printed ver.) ISBN 978-82-326-2991-6 (electronic ver.) ISSN 1503-8181.

“Modeling and simulation of the soft palate for improved understanding of the obstructive sleep apnea syndrome”,
Hongliang Liu, 2018:101, ISBN 978-82-326-2992-3 (printed ver.) ISBN 978-82-326-2993-0 (electronic ver.) ISSN 1503-8181.

“Long-term extreme response analysis of cable-supported bridges with floating pylons subjected to wind and wave loads”,
Yuwang Xu, 2018:229, ISBN 978-82-326-3248-0 (printed ver.) ISBN 978-82-326-3249-7 (electronic ver.) ISSN 1503-8181.

“Reinforcement corrosion in carbonated fly ash concrete”,
Andres Belda Revert, 2018:230, ISBN 978-82-326-3250-3 (printed ver.) ISBN 978-82-326-3251-0 (electronic ver.) ISSN 1503-8181.

“Direct finite element method for nonliear earthquake analysis of concrete dams including dam-water-foundation rock interaction”,
Arnkjell Løkke, 2018:252, ISBN 978-82-326-3294-7 (printed ver.) ISBN 978-82-326-3295-4 (electronic ver.) ISSN 1503-8181.

“Electromechanical characterization of metal-coated polymer spheres for conductive adhesives”,
Molly Strimbeck Bazilchuk, 2018:295, ISBN 978-82-326-3380-7 (printed. ver.) ISBN 978-82-326-3381-4 (electrical ver.) ISSN 1503-8181.

“Determining the tensile properties of Artic materials and modelling their effects on fracture”,
Shengwen Tu, 2018:269, ISBN 978-82-326-3328-9 (printed ver.) ISBN 978-82-326-3329-6 (electronic ver.) ISSN 1503-8181.

“Atomistic Insigth into Tranportation of Nanofluid in Ultra-confined Channel”,
Xiao Wang, 2018:334, ISBN978-82-326-3456-9 (printed ver.) ISBN 978-82-326-3457-6 (electronic ver.) ISSN 1503-8181.

“An experimental and numerical study of the mechanical behaviour of short glass-fibre reinforced thermoplastics”,
Jens Petter Henrik Holmstrøm, 2019:79, ISBN 978-82-326-3760-7 (printed ver.) ISBN 978-82-326-3761-4 (electronic ver.) ISSN 1503-8181.

“Uncertainty quantification and sensitivity analysis informed modeling of physical systems”,
Jacob Sturdy, 2019:115, ISBN 978-82-326-3828-4 (printed ver.) ISBN 978-82-326-3829-1 (electric ver.) ISSN 1503-8181.

“Load model of historic traffic for fatigue life estimation of Norwegian railway bridges”,
Gunnstein T. Frøseth, 2019:73, ISBN 978-82-326-3748-5 (printed ver.) ISBN 978-82-326-3749-2 (electronic ver.) ISSN 1503-8181.

“Force identification and response estimation in floating and suspension bridges using measured dynamic response”,
Øyvind Wiig Petersen, 2019:88, ISBN 978-82-326-3778-2 (printed ver.) ISBN 978-82-326-377-9 (electronic ver.) ISSN 1503-8181.

“Consistent crack width calculation methods for reinforced concrete elements subjected to 1D and 2D stress states”,
Reignard Tan, 2019:147, ISBN 978-82-326-3892-5 (printed ver.) ISBN 978-82-326-3893-2 (electronic ver.) ISSN 1503-8181.

“Nonlinear static and dynamic isogeometric analysis of slender spatial and beam type structures”,
Siv Bente Raknes, 2019:181, ISBN 978-82-326-3958-8 (printed ver.) ISBN 978-82-326-3959-5 (electronic ver.) ISSN 1503-8181.

“Experimental study of concrete-ice abrasion and concrete surface topography modification”,
Guzel Shamsutdinova, 2019:182, ISBN978-82-326-3960-1 (printed ver.) ISBN 978-82-326-3961-8 (electronic ver.) ISSN 1503-8181.

“Wind forces on bridge decks using state-of-the art FSI methods”,
Tore Andreas Helgedagsrud, 2019:180, ISBN 978-82-326-3956-4 (printed ver.) ISBN 978-82-326-3957-1 (electronic ver.) ISSN 1503-8181.

“Numerical Study on Ductile-to-Brittle Transition of Steel and its Behavior under Residual Stresses”,
Yang Li, 2019:227, ISBN 978-82-326-4050-8 (printed ver.) ISBN 978-82-326-4015-5 (electronic ver.) ISSN 1503-8181.

“Micromechanical modelling of ductile fracture in aluminium alloys”,
Bjørn Håkon Frodal, 2019:253, ISBN 978-82-326-4102-4 (printed ver.) ISBN 978-82-326-4103-1 (electronic ver.) ISSN 1503-8181.

“Monolithic and laminated glass under extreme loading: Experiments, modelling and simulations”,
Karoline Osnes, 2019:304, ISBN 978-82-326-4204-5 (printed ver.) ISBN 978-82-326-4205-2 (electronic ver.) ISSN 1503-8181.

“Plastic flow and fracture of isotropic and anisotropic 6000-series aluminium alloys: Experiments and numerical simulations”,
Susanne Thomesen, 2019:312, ISBN 978-82-326-4220-5 (printed ver.), ISBN 978-82-326-4221-2 (electriniv ver.) ISSN 1503-8181

“Stress-laminated timber decks in bridges”,
Francesco Mirko Massaro, 2019:346, ISBN 978-82-326-4288-5 (printed ver.), ISBN 978-82-326-4289-2 (electronic ver.) ISSN 1503-8181

“Connections between steel and aluminium using adhesive bonding combined with self-piercing riveting: Testing, modelling and analysis”,
Matthias Reil, 2019:319, ISBN 978-82-326-4234-2 (printed ver.), ISBN 978-82-326-4235-9 (electronic ver.) ISSN 1503-8181

“Designing Polymeric Icephobic Materials”,
Yizhi Zhuo, 2019:345, ISBN 978-82-326-4286-1 (printed ver.), ISBN 978-82-326-4287-8 (electronic ver.) ISSN 1503-8181

“Fundamental Mechanisms of Ice Adhesion”,
Rønneberg, Sigrid 2020:87, ISBN 978-82-326-4527-8 (printed version) ISBN 978-82-326-4524-5 (electronic version) ISSN 1503-8181

“Mechanical modeling of the polymeric coating on a subsea pipeline”,
Vestrum, Ole 2020:105, ISBN 978-82-326-4562-6 (printed version) ISBN 978-82-4563-3 (electronic version) ISSN 1503-8181

“Conceptual form-finding in structural engineering”,
Marcin Luczkowski 2020:232, ISBN 978-82-326-4812-2 (printed version) ISBN 978-82-326-4813-9 (electronic version) ISSN 1503-8181

“Self-assembled superstructures of magnetic nanoparticles: advanced nanofabrication and enhanced mechanical properties”,
Verner Håkonsen 2020:271, ISBN 978-82-326-4890-0 (printed version) ISBN 978-82-326-4891-7 (electronic version) ISSN 1503-8181

“Micromechanical modelling of fracture in ductile alloys with applications to high-strength steel”,
Sondre Bergo 2020:313, ISBN 978-82-326-4974-7 (printed version) ISBN 978-82-326- 4975-4 (electronic version) ISSN 1503-8181

“Fracture in wood of Norway spruce - Experimental and numerical study”,
Katarzyna Ostapska 2020:314, ISBN 978-82-326-4976-1 (printed version) ISBN 978-82-326-4977-8 (electronic version) ISSN 1503-8181

“Dynamic anti-icing surfaces (DAIS)”,
Feng Wang 2020:330 ISBN 978-82-326-5006-4 (printed version) ISBN 978-82-326-5007-1 (electronic version) ISSN 1503-8181

“Multiaxial Fatigue analysis of offshore mooring chains, considering the effects of residual stresses and corrosion pits”,
Ershad P. Zarandi 2020:337 ISBN 978-82-326-5020-0 (printed version) ISBN 978-82-326-5021-7 (electronic version) ISSN 1503-8181

“Production and documentation of frost durable high-volume fly ash concrete: air entrainment, cracking and scaling in performance testing”,
Andrei Shpak 2020:366 ISBN 978-82-326-5078-1 (printed version) ISBN 978-82-326-5079-8 (electronic version) ISSN 1503-8181

“Physics-based and data-driven reduced-order blood flow models: Applications to coronary artery disease diagnostics”,
Fredrik Eikeland Fossan 2020:362 ISBN 978-82-326-5070-5 (printed version) ISBN 978-82-326-5071-2 (electronic version) ISSN 1503-8181

“Multi-scale modelling and simulation of ductile failure in aluminium structures”,
Henrik Granum 2020:374 ISBN 978-82-326-5094-1 (printed version) ISBN 978-82-326-5095-8 (electronic version) ISSN 1503-8181

“Testing and modelling of multi-material joints”,
Jon Fredrick Berntsen 2020:368 ISBN 978-82-326-5082-8 (printed version) ISBN 978-82-326-5083-5 ISSN 1503-8181

“Heuristic models for wear prediction and dynamic-based condition monitoring techniques in pantograph-catenary interaction”,
Stefano Derosa 2020:381 ISBN 978-82-326-5108-5 (printed version) ISBN 978-82-326-5109-2 (electronic version) ISSN 1503-8181

“Experimental and numerical study of dilation in mineral filled PVC”,
Sindre Nordmark Olufsen 2020:388 ISBN 978-82-326-5122-1 (printed version) ISBN 978-82-326-5123-8 (electronic version) ISSN 1503-8181

“Residual stresses and dimensional deviation in metal additive manufacturing: prediction and mitigation methods”,
Li Sun 2020:411 ISBN 978-82-471-9600-7 (printed version) ISBN 978-82-471-9581-9 (electronic version) ISSN 1503-8181 (printed version) ISSN 2703-8084 (online version)

“Moment-resisting timber frames with semi-rigid connections”,
Aivars Vilguts 2021:88 ISBN 978-82-326-6987 (printed version) ISBN 978-82-326-5737-7 (electronic version) ISSN 2703-8084 (online version)

“Thermal transport in metal-polymer systems”,
Susanne Sandell 2021:63 ISBN 978-82-326-5304-1 (printed version) ISBN 978-82-326-6278-4 (electronic version) ISSN 2703-8084 (online version)

“Competitive timber floors”,
Sveinung Ørjan Nesheim 2021:134 ISBN 978-82-326-6481-8 (printed version) ISBN 978-82-326-5399-7 (electronic version) ISSN 2703-8084

“Thermodynamics of Nanoscale Films and Fluid Volumes”,
Bjørn Andre Strøm 2021:166 ISBN 978-82-326-6778-9 (printed version) ISBN 978-82-326-5900-5 (electronic version) ISSN 2703-8084 (online version)

“Characterization and modeling of the mechanical behavior of polymer foam”,
Daniel Thor Morton 2021:173 ISBN 978-82-326-6245-6 (printed version) ISBN 978-82-326-5699-8 (electronic version) ISSN 2703-8084 (online version)

“Atomistic Insights to Interfacial Dynamics”,
Yuequn Fu 2021:233 ISBN 978-82-326-5530-4 (printed version) ISBN 978-82-326-6894-6 (electronic version) ISSN 2703-8084 (online version)

“Mechanisms and enhancement of CO2 condensation heat transfer”,
Ingrid Snustad 2021:236 ISBN 978-82-326-5606-6 (printed version) ISBN 978-82-236-6715-4 (electronic version) ISSN 2703-8084

“Experimental study of reinforced concrete slabs subjected to fire exposure and blast loading”,
Assis Arano Barenys 2021:239 ISBN978-82-326-5289-1 (printed version) ISBN 978-82-326-5876-3 (electronic version) ISSN 2703-8084 (online version)

“Long-term extreme buffeting response investigations for long-span bridges considering uncertain turbulence parameters based on field measurements”,
Tor Martin Lystad 2021:216 ISBN 978-82-326-5797-1 (printed version) ISBN 978-82-326-6154-1 (electronic version) ISSN 2703-8084 (online version)